VILNIUS UNIVERSITY

and

CENTER FOR PHYSICAL SCIENCES AND TECHNOLOGY

VALDEMAR STANKEVIČ

FORMATION AND CHARACTERIZATION OF MICRO –OPTO - MECHANICAL 3D DEVICES FOR SENSOR APPLICATION IN TRANSPARENT MATERIALS

Doctoral dissertation

Technology Science, Material Engineering (08T)

Vilnius 2017

The research described in this thesis was performed in 2012-2016 in the Department of Laser Technologies of the Center for Physical Sciences and Technology (Savanoriu Ave. 231, Vilnius, Lithuania).

Scientific supervisor

Dr. **Gediminas Račiukaitis** (Center for Physical Sciences and Technology, Technology Science, Material Engineering – 08T, Laser Technology - T165).

VILNIAUS UNIVERSITETAS

ir

FIZINIŲ IR TECHNOLOGIJOS MOKSLŲ CENTRAS

Valdemar Stankevič

TRIMAČIŲ MIKROOPTOMECHANINIŲ DARINIŲ JUTIKLIAMS FORMAVIMAS LAZERIAIS SKAIDRIOSE TERPĖSE IR JŲ CHARAKTERIZAVIMAS

Daktaro disertacija

Technologijos mokslai, medžiagų inžinerija (08T)

Vilnius 2017

Disertacija rengta 2012-2016 m. Valstybinio mokslinių tyrimo instituto Fizinių ir technologijos mokslų centro Lazerinių technologijų skyriuje (Savanorių pr. 231, Vilnius, Lietuva).

Mokslinis vadovas

Dr. Gediminas Račiukaitis (Fizinių ir technologijos mokslų centras, technologijos mokslai, medžiagų inžinerija - 08T, lazerinė technologija - T165)

Table of Contents

Abstract

During the past two decades, the femtosecond laser material processing (FLMP) has been developing at an exponential rate. Various materials were processed starting from a simple metal ablation and ending with internal 3D modification inside transparent materials for the Lab-on-chip and MEMS (Micro-electro-mechanical systems) applications. The femtosecond laser fabrication is a complex technique that opens future perspectives for micro and nano-level technology development. Currently, the direct laser writing (DLW) technique in combination with a femtosecond laser is a key feature for applications in two-photon polymerization and modification of transparent materials. For processing of transparent materials where the fused silica and Foturan glass plays a major role, objectives with a numerical aperture NA≤0.7 are used to be sufficient to initiate internal modifications for the waveguides writing and selectively induced etching of modified areas. In such focusing conditions, extremely high intensities are achieved at the focal spot, and, therefore, it is possible to initiate nonlinear absorption and more predictable modification of materials.

In this thesis, the combination of a few topics is presented. In the beginning, the femtosecond laser-induced chemical etching technique (FLICE) was used for microchannels inscription in bulk fused silica. The various ranges of the highly focused femtosecond pulses parameters were investigated for optimising the microchannels etching rate. The etching selectivity was induced due to the volume nanostructures that are oriented perpendicularly to the laser beam polarisation. The nature of the nanogratings is not completely understood thus this phenomenon is under debate. By investigating the quality of such nanogratings with the SEM microscope, it has been observed that the orientation of the nanogratings was slightly tilted with respect to the scan direction. This remark followed the discovery of the new phenomenon that demonstrated the nanogratings tilt dependence on the

different scanning directions when laser polarisation was kept constant. The phenomenon was investigated under the different laser radiation parameters, and a theoretical model was proposed. Finally, the practical applications of the FLICE technique were demonstrated by fabricating three different 3D microfluidic devices for fluid pumping, microchannels for ellipsometric application and challenging double-side aspheric microfluidic lens for light focusing from the Y-shaped waveguide.

Acknowledgements

Numerous individuals had participated in realising my ideas and my professional growth. I would like to express my sincerely thanks to all of them.

First of all, I am thankful to my supervisor Gediminas Račiukaitis that proposed me to start this new topic with almost no background from the local scientists and inspired me never to get down.

Thanks to FTMC where I am preparing my thesis, for support in my scientific practice at Milano Politecnico where I meet a lot of friendly people and have had a major input for my thesis realisation.

Many thanks for personnel from ELAS company where I am working as an application engineer. Thanks to that co-workers: Arvydas, Viktoras, Artūras I spent many hours discussing the laser micromachining topics and for their help to me by preparing mechanical drawings for beam delivery setups.

I want to say many thanks to Professor Saulius Juodkazis that believed me and helped to introduce to the world of nanogratings in transparent materials.

Especially I want to thank my wife Agneška and daughter Adela, that supported me independent on whether conditions and for the motivation during the thesis writing.

Thanks to individuals from the chemical laboratory of FTMC that helped me to manage the experiments on chemical etching in the HF environmental. Especially,

I want to say thank for Rasa Gvozdaitė who had a personal obligation to support me at any time when I had a need to etch some samples.

Introduction

Since the first laser invention by T. Maiman in 1961 [1], the growth of applications of lasers in different field accelerated and will reach its apogee in the near future. After the development of new powerful laser systems with sub-picosecond pulse duration [2] and high-quality beam parameters, it became possible to reach the diffraction limited focusing where the extremely high intensities allowed to open new frontiers in the light-mater interaction. The currently available industrial femtosecond lasers are very stable laser sources that provide pulse intensities of ~ 10^{13}W/cm^2. Such high intensities ensure the ionisation of all transparent materials and fast cooling rates comparing to the longer pulse duration lasers. In 1994, the femtosecond lasers were firstly used for ablation experiments on the surface of fused silica [3] and silver [4]. The intriguing advantages such as induced nonlinear processes and reduced heat affected zone allowed the fabrication with a sub-micrometer resolution that consequently evoked a strong interest and brought the fabrication to a new level for three-dimensional bulk modifications.

The first example of the bulk processing was demonstrated by K. Hirao team in 1996, when they have shown a permanent refractive index modification (up to 10^{-2}) inside the bulk of transparent materials [5, 6] induced by the tightly focused femtosecond laser pulses below the damage threshold. This phenomenon enabled the formation of optical devices in a variety of dielectric transparent materials with the direct laser writing (DLW) technique simply by translating a sample under the tightly focused femtosecond laser beam. Hence the modification remains embedded inside the transparent material, and focusing depth can be arbitrarily changed, this enables the three-dimensional fabrication. This fabrication technique was acknowledged by many scientific groups as the optical waveguides can be created

inside of transparent materials. Fabrication of waveguides and three-dimensional couplers were reported [7–9]. There are a few ways how to produce internal modifications depending on the sample translation: longitudinal or perpendicular to the beam propagation direction. In the longitudinal way, the waveguides are fabricated symmetrically. However, their length is limited by the focusing optics. In the perpendicular writing configuration, there is more flexibility to record the waveguides of the required length, but their cross-section is asymmetrical and suffers, therefore, larger losses. To defeat this drawback, a few methods were proposed. By using astigmatic beam shaping [10] during the focusing of the femtosecond pulses, the asymmetry in transverse geometry was eliminated. However, this allowed recording the waveguides only in one direction with a compensated asymmetry. Thus in 2005, the spatial-temporal focusing for microscopy application was proposed by Zhu et al. [11] and it was adapted to the laser microfabrication [12]. This method allowed to avoid any asymmetry in various scanning directions and write waveguides with almost circular cross-section.

Besides the waveguide writing, the femtosecond pulses with the intensity slightly higher than required for the refractive index modification can induce uniaxial birefringence in fused silica. In 2002, it was suggested that this kind of birefringence might by caused by sub-surface nanogratings oriented perpendicular to the electrical vector direction of the laser beam (polarisation) [13]. The first qualitative prove of the evidence of the periodic nanostructures was reported in 2003 by Shimotsuma et al. [14]. The discovered nanostructures had a period approximately equal to a half of the wavelength. In subsequent years, it was demonstrated the long-range order of the periodical structures that was explained by the self-replication phenomenon [15]. The multi-pulse irradiation which created nanogratings opened the way for a few more applications in photonics [16] as well as in the three-dimensional microfluidic channels formation where the laser-modified material in combination with the chemical etching allows fabrication of microstructures in fused silica by the technique known as Femtosecond Laser

Irradiation followed by Chemical Etching (FLICE) [17]. The same technique was applied to photo-structurable glasses with an additional step involving a heat treatment [18]. Controlling of the etching rate of the modified materials up to two orders of magnitude enabled achieving long, high-aspect-ratio channels. The FLICE consists of two steps: 1) The permanent sample modification under high-intensity femtosecond pulses and 2) exposure of the modified zone to the hydrofluoric acid (HF) solution. The advantages of the FLICE technique comparing to the conventional fabrication of the microfluidic channels are evident: 1) there is no need to use photolithography and clean rooms; 2) there is no reason to seal with a cover glass the buried channels; 3) the circular cross section channels are produced in a natural way; 4) the straightforward 3D geometry of the channels is allowed.

After the FLICE technique invention, many ideas emerged how to combine the waveguides writing and microchannels in a single platform. It allowed fabricating the microfluidic devices with an integrated optical sensing. For this new field definition, the new term “optofluidics” has been recently introduced [19, 20] where the synergy of optics and fluidics was exploited to realise entirely new functionalities.

In this thesis, the microchannels etching selectivity was investigated over a broad range of the processing parameters. The pulse duration influence to the etching selectivity at the various wavelength is overviewed. The new phenomena of the induced tilt of the nanogratings are overviewed. The approaches of the new microfluidic and optofluidic devices are presented.

Main thesis objectives

The aim of this thesis was to introduce and develop the new technology -FLICE at the Department of the Laser Technologies of FTMC, and use it for fabrication of complex 3D microfluidic devices.

The practical tasks were:

1. Investigate the etching selectivity of fused silica, modified with the femtosecond laser pulses depending on broad range of the laser process and etching parameters;
2. Perform detailed investigations of the nanograting formation inside the modified region, how their orientation is influenced by the writing direction and laser pulse energy at the constant polarisation direction;
3. To develop and fabricate using the FLICE technology the microfluidic devices with a complex 3D geometry, which can be utilised for sensing and detection applications.

Novelty

The FLICE technique is the new field in Lithuania, and we wanted to show benefits in utilising ultrashort pulse lasers produced in Lithuania. The main goal was to optimise the process and increase its throughput. Therefore, a broad range of processing parameters was checked for the etching selectivity. It was demonstrated that the shortest pulse duration could not be treated as the best solution whereas the optimal pulse duration was ~ 700 fs with evident improvement of the nanograting quality under the detailed SEM inspection.

Considerable attention was paid to improve the etching conditions. In this case, the various HF acid temperatures and concentrations were tested. The etching in ultrasonic bath showed a huge improvement in the etching time.

By investigating the nanogratings in bulk fused silica the new phenomenon: the nanograting till dependence on the scan direction was discovered. It was demonstrated that the nanogratings are not strongly perpendicular to the electric field polarisation. A vectorial light-matter interaction model was developed to explain all the observed features.

The complex microstructures inside the bulk fused silica were fabricated by stacking the single line modifications and etched in diluted HF acid. The etching

improvement of the internal microstructures was demonstrated by introducing new contour scanning algorithm allowing the easier acid diffusion to the laser-modified region.

Three different devices for the microfluidic applications are presented. The unique passive micropump device based on the Venturi tube was fabricated, and pumping ability was demonstrated. The micropump design was optimised by numerical simulation, and additionally, its fluid mixing ability was discovered.

The new design of the internal-to-external microfluidic channels was proposed for ellipsometric applications to measure the absorption kinetics of proteins. The microfluidic channels in fused silica allowed the measurement parallelization that saved the tested material and minimised the measurement time.

The most advanced microfluidic device was designed to make the ability for focus the light coming from a Y-shaped waveguide. Here, the key component was the complex double side hollow aspherical lens filled with the refractive index matching fluid. The designed lens was able to collimate the light coming from separate waveguides and focus it to the single spot. The complexity of the device was to integrate waveguides and the microfluidic lens to a single device and couple the light from the single mode fibre to the waveguide.

The statements to defend

1. The fused silica etching selectivity in the 15% HF acid solution of >1:140 can be achieved by the FLICE technology utilising Yb-based femtosecond laser radiation of fundamental harmonics with the optimal pulse duration exceeding 700 fs.
2. The tilt between the nanograting orientation and the polarisation for different scan directions as high as ~ 2^{o} (maximal when directions of the scan and the polarisation have an angle of $\pi/4$ @1030 nm) can appear due to coupling between the temperature gradient and electric field vector causing anisotropy in heat diffusion process.

3. In the FLICE technology with the optimized pulse energy, utilising the contour scanning method and linear or circular polarization, the enhanced HF acid penetration to the modified 3D structures in the bulk of fused silica and the maximal etching selectivity are achieved leading to the minimal surface roughness of ~ 75 nm.

Approbation

The results of the research described in this thesis are published in 4 publications in scientific journals included in the ISI Journal list. These results were presented at 12 conferences (listed below), 10 of which were personally presented by the author.

Publications directly related to the topic of the dissertation (ISI)

[P1] V. Stankevič, G. Račiukaitis, **Laser-induced chemical etching of micro-channels in fused silica**, Lithuanian Journal of Physics, **54** (3) 136-141 (2014).

[P2] V. Stankevič, G. Račiukaitis, **Free-shape 3D Structure Formation in Bulk Fused Silica by Irradiation with Femtosecond Laser Pulses,** Journal of Laser Micro/Nanoengineering, **9** (3), 271-275 (2014).

[P3] V. Stankevič, T. Rakickas, G. Račiukaitis, **Internal-to-external microfluidic device for ellipsometric biosensor application**, Journal of Laser Micro/Nanoengineering, **11**(1), 53-58 (2016).

[P4] V. Stankevič, G. Račiukaitis, F. Bragheri, X. Wang, E. G. Gamaly, R. Osellame, and S. Juodkazis, **Laser printed nano-gratings: orientation and period peculiarities**, *Sci. Rep.* **7,** 39989 (2017).

Conference presentations directly related to the topic of the dissertation

[C1] V. Stankevič, G. Račiukaitis, ***Kanalų formavimas lydyto kvarco tūryje ultratrumpaisiais impulsais***, 40 – oji Lietuvos nacionalinė fizikos konferencija, Vilnius, Lithuania, June 10-12, 2013. (poster).

[C2] V. Stankevič, G. Račiukaitis, **Laser-induced chemical etching of microchannels in fused silica**, 20-th Lithuania – Belarus seminar, Vilnius, Lithuania, November 21-22, 2013. (poster).

[C3] V. Stankevič, G. Račiukaitis, **Free-shape 3D structure formation in bulk fused silica by irradiation with femtosecond laser pulses**, 15-th International Symposium on Laser Precision Microfabrication (LPM 2014), Vilnius, Lithuania, June 17-20, 2014 (poster).

[C4] V. Stankevič, G. Račiukaitis, **Laisvos formos 3D struktūrų formavimas lydytame kvarce femtosekundinio lazerio impulsais**, Doktorantų mokslinė konferencija, Vilnius, Lithuania, 2014 (oral).

[C5] V. Stankevič, G.Račiukaitis, **Mikrosiurblio gamyba lydytame kvarce lazeriu inicijuoto cheminio ėsdinimo būdu**, 41 – oji Lietuvos nacionalinė fizikos konferencija, Vilnius, Lithuania, 17-19 June, 2015. (poster);

[C6] V. Stankevič, T. Rakickas, G. Račiukaitis**, Internal-to-external microfluidic device for ellipsometric biosensor application**, 7-th International Congress on Laser Advanced Materials Processing (LAMP 2015), Kitakyushu, Japonija, May 26-29, 2015 (poster);

[C7] L. Rimgaila, V. Stankevič, G.Račiukaitis, **Aukšto efektyvumo tūrinių Brego gardelių kūrimas naudojantis femtosekundinę spinduliuotę lydytame kvarce**, 41 – oji Lietuvos nacionalinė fizikos konferencija, Vilnius, Lithuania, 17-19 June, 2015. (poster);

[C8] V.Stankevič, G. Račiukaitis, **Fabrication of micropump device with mixing functionality in fused silica with ultrashort laser pulses**, Lasers in Manufacturing (LiM 2015), Munich, Germany, June 25-29, 2015 (oral).

[C9] V. Stankevič, G. Račiukaitis, **Orientation Instabilities of Nanogratings in Fused Silica**, 17-th International Symposium on Laser Precision Microfabrication (LPM 2016), Xi'an, China, May 23-27, 2016 (oral).

[C10] V. Stankevič, G. Račiukaitis, **Influence of focusing depth for the nanograting formation and etching selectivity in fused silica**. 10-th International Conference on photo-excited process and applications (ICPEPA-10), Brasov, Romania, August 29 – September 2, 2016 (poster).

[C11] V. Stankevič, G. Račiukaitis, **Tilt of nanogratings recorded by femtosecond laser pulses. 10-th International Conference on photoexcited process and applications** (ICPEPA-10), Brasov, Romania, August 29 – September 2, 2016 (oral).

[C12] V. Stankevič, G. Račiukaitis, F. Bragheri, X. Wang, E. G. Gamaly, R. Osellame and S. Juodkazis, **Orientation instabilities of nanogratings recorded by femtosecond laser pulses in silica**, Bragg gratings, photosensitivity and poling in glass waveguides (BGPP), Sydney, Australia, September 5-8, 2016 (oral).

Patents

1. G. Račiukaitis, M. Gedvilas, V. Stankevič, applicants: FTMC and UAB ELAS, **Method and apparatus for laser cutting of transparent media**, patent EP 2944412, issued 2016 11 02.

Contributions

Author's Contribution

The author designed and prepared the experimental setups, generated the experimental ideas and methods. He also designed the characterization setup and analysed all the experimental data. The SEM and microscopes pictures were made personally by the author. The main text of the publications P1-P3 was prepared by the author and the editing was performed together with the co-authors.

Francesca Bragheri partly participated in the sample fabrication and data analysis made for the publication P4.

Saulius Juodkazis and Roberto Osellame provided the initial ideas on the nanograting tilt phenomena explanation.

Xuewen Wang performed the initial numerical simulations for the nanograting tilt phenomena understanding.

Tomas Rakickas performed the iSPR measurement experiments and edited the manuscript [P3].

List of Acronyms

1D – one dimensional

3D – three dimensional

BSA – bovine serum albumin

CAD – computer-aided design

CCD – charged coupled device

cw – clockwise

CW – continuous-wave operation

DLW – direct laser writing

FFT – Fast Fourier Transformation

FLICE – femtosecond laser-induced chemical etching

FLMP – femtosecond laser material processing

FROG – frequency optical gating

HEPES - 4-(2-hydroxyethyl)-1-piperazineethanesulfonic acid

HF – hydrofluoric acid

IR – infrared

iSPR – imaging Surface Plasmon Resonance

KOH – potassium hydroxide

LIPPS – laser-induced periodic surface structures

LOC – lab-on-chip

MEMS – micro-electro-mechanical systems

NA – numerical aperture

PDMS – polydimethylsiloxane

PFT – pulse front tilt

SEM – scanning electron microscope

SHG – second harmonic generation

SPIM – selective plane illumination microscopy

SPP – surface plasmons polaritons

UV – ultraviolet

WAFLD – direct ablation of glass in water

Yb:KGW – ytterbium doped potassium gadolinium tungstate

Yb:KYW – ytterbium doped potassium yttrium tungstate

1 Theoretical background

1.1 Interaction of femtosecond laser pulses with dielectric materials

For dielectric materials at absolute zero temperature, the valence band is highest occupied energy level with electrons as the lowest available energy states are always nearly completely filled with electrons. The lowest unoccupied energy level in the material – the conduction band is separated by the energy gap, E_g, from the valence band. When the material is irradiated by a strong intensity of electromagnetic field that exceeds the bandgap energy, the valence electrons gain enough energy, and they can leave the valence band, reach the conduction band and become free electrons. Usually, the energy of a single photon in the visible light is not high enough to overpass the bandgap of typical optical materials. In this case, the nonlinear multiphoton absorption processes are required to initiate the ionisation.

1.1.1 *Nonlinear Excitation Mechanisms*

When a low-intensity laser beam irradiates a transparent material, only linear optical effects such as reflection, diffraction, transmission and absorption may be observed. However, when the laser intensity is intense enough, nonlinear optical effects occur, and reversible and non-reversible material modifications become possible. The nature of these laser-induced phenomena is usually characterised by the combination of the laser parameters (pulse duration, fluence, wavelength, and repetition rate) and the optical, mechanical, and thermal properties of the target materials. During the laser-induced breakdown or laser ablation, the first stage is the transfer of the laser energy to electrons through multiphoton absorption followed by inverse bremsstrahlung heating, and the transfer of energy into the lattice through the electron-phonon interaction. Eventually, the electrons and lattice

reach thermal equilibrium on a time scale of a few picoseconds [21, 22]. This time scale (electron-phonon interaction time) sets the boundary for thermal and/or non-thermal interactions, i.e., material modification with pulses longer or shorter than this timescale which is also termed as “long-pulse” or “short-pulse” [23] resulting in the significantly different interaction mechanisms.

Due to the ultrashort pulse duration, the peak intensities at the focal plane are as big as $I > \sim 10^{13}$ W/cm^2. When such pulses are focused inside transparent materials (e.g. fused silica), the nonlinear absorption is a leading phenomenon in the light-mater interaction process. The band gap of dielectric materials, as a rule, is much larger than the single photon energy of the second harmonics (515-532 nm) laser source. For example, the photon energy of the 515 nm pulses is ~ 2.4 eV, while the bandgap of fused silica is ~ 9 eV. In the linear absorption case, the band gap of the material E_g should be lower than the single photon energy $\hbar\omega$ to ionise the irradiated material. In the other hand, when the laser beam intensity is sufficiently strong, absorption in the pure transparent material can occur only through the nonlinear absorption mechanism. The main two classes of the non-linear absorption processes responsible for such interaction are the nonlinear ionisation and avalanche ionisation [24, 25]. Photoionization refers to excitation of the electron into the conduction band by the laser radiation field. The ionisation may occur in two forms: tunnelling or multiphoton absorption [24].

1.1.1.1 Photoionization

Multiphoton ionisation is the dominant mechanism for lower laser intensities (still sufficient for multiphoton absorption) and higher frequencies. During this process, several photons are absorbed by an electron simultaneously (Figure 1, right). At high laser intensity and low frequency [24], the Coulomb well binds a valence electron to its parent atom and can be suppressed enough that there is a significant probability that the bound electron can tunnel through the barrier, and then the nonlinear ionisation is accelerated via tunnelling ionisation (Figure 1, left).

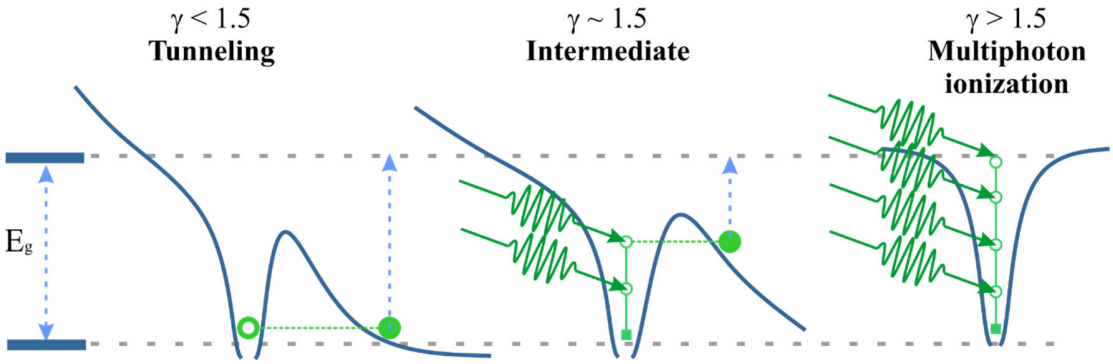

Figure 1 Nonlinear photoionization processes underlying femtosecond laser machining (left); tunnelling (central); combined nonlinear processes (right) multiphoton ionisation. Source [24].

In 1965, Keldysh proposed the adiabaticity parameter now known as the Keldysh parameter to indicate the regime in which the processes might occur [26]:

$$\gamma = \frac{\omega}{e}\sqrt{\frac{m_e c n \varepsilon_0 E_g}{I}}, \tag{1.1}$$

where ω is the laser radiation frequency, e is the electron charge , m_e is the mass of the electron, c is the velocity of light, n is the refractive index of the material, ε_0 is the permittivity of the free space, E_g is the band gap of the material, and I is the intensity of the laser beam. When the Keldysh parameter exceeds the 1.5 value, the multiphoton ionisation plays a major role; if it is smaller than 1.5, the tunnelling process is dominating. For intermediate situation, the behaviour of the ionisation is a combination of two mechanisms.

For multiphoton ionisation, the laser intensity I has a strong influence on photoionization rate:

$$P_{PI}(I) = \sigma_n I^n \tag{1.2}$$

where σ_n is the multiphoton absorption coefficient for n photons. The number of photons required to excite the electron to the conduction band is described by the following condition:

$$\hbar\omega \geq E_g \tag{1.3}$$

where ω is the photon frequency and $\hbar$ is the Planck constant. For short laser pulses, the multiphoton ionisation is dominating mechanism of free electron generation that makes it less dependent on defects in the material than long-pulse breakdown and therefore is a more deterministic process. For longer laser pulses, the seed electrons cannot be excited directly from valence band to the conduction band due to the insufficient peak intensity, and the process becomes strongly dependent on random impurities and defects. Consequently, the process is less deterministic.

1.1.1.2 Avalanche Ionization

When electrons are already in the conduction band, they can sequentially absorb several photons and gain the energy over the bottom of the conduction band (see Figure 2). The electron in the conduction band which energy exceeds the band-gap energy can then collisionally ionise another electron from the valence band by the impact ionisation. As a result, the two electrons are in the lowest available energy state in the conduction band. [24, 27]. Each of them can absorb the energy through the free carrier absorption and repeat the energy transfer cycle again. This process will repeat as long as the laser field is present as well increasing the density of electrons in the conduction band exponentially. The avalanche ionisation process generates the following electron density:

$$\eta_{av}(t) = \eta_0 2^{w_{imp}t} = \eta_0 e^{w_{imp}t \ln 2} \tag{1.4}$$

where η_0 is the initial (seed) electron concentration, and w_{imp} is the probability of the impact ionisation.

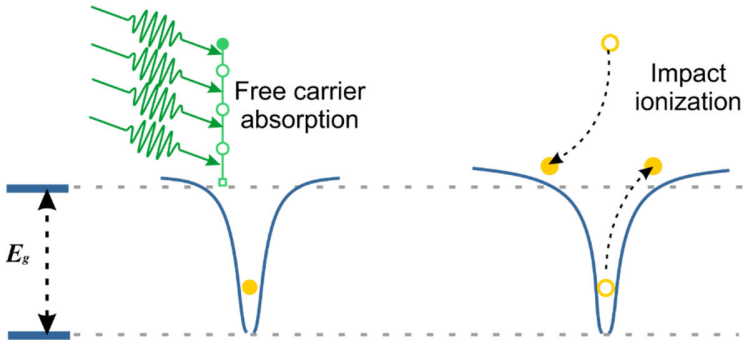

Figure 2 Schematic diagram of avalanche (impact) ionization [24].

To trigger the avalanche ionisation process, the presence of the seed electrons is required. It was shown that larger probability for the avalanche ionisation development is for the pulse durations starting from the 200 fs and greater [28]. For materials with defects, the seed electrons come from low-lying levels via linear absorption or thermal excitation [24]. However, for pure, perfect dielectrics, the photoionization is the main process for supplying of seed electrons.

1.1.1.3 Damage threshold and energy transfer for different pulse durations

The permanent material damage occurs when the sufficient energy is absorbed. The damage threshold describes the irradiation intensity when permanent damage occurs, however, there is no widely accepted measuring technique. Usually, the damage threshold measurements are performed by the evaluation of the damages by the optical techniques [24, 29]. The damage threshold values on the material surface and in bulk are entirely different processes, but frequently there are considered as the same quantity. The surface damage is strongly influenced by the surface preparation [30] (polishing quality, impurities) while in the volume, the self-focusing and the spherical aberrations have an additional impact [31].

The laser pulse duration plays a key role in the material modification mechanisms. The electrons are excited during the laser pulse irradiation and distribute the energy among themselves via carrier-carrier scattering (10-100 fs) and carrier-phonon scattering (>10 ps). The first process is fast enough and

redistributes the energy among the excited electrons. However, the second process is slower. It transfers the energy to the lattice and reaches the equilibrium between electrons and lattice.

For the pulse durations longer than 10 ps, the major energy is transferred to the lattice during the pulse propagation [24]. In the vicinity of the focal region, the energy is transferred via the excited lattice phonons by the thermal diffusion, and consequently, when the temperature of the material reaches the melting point, the damage is inevitable.

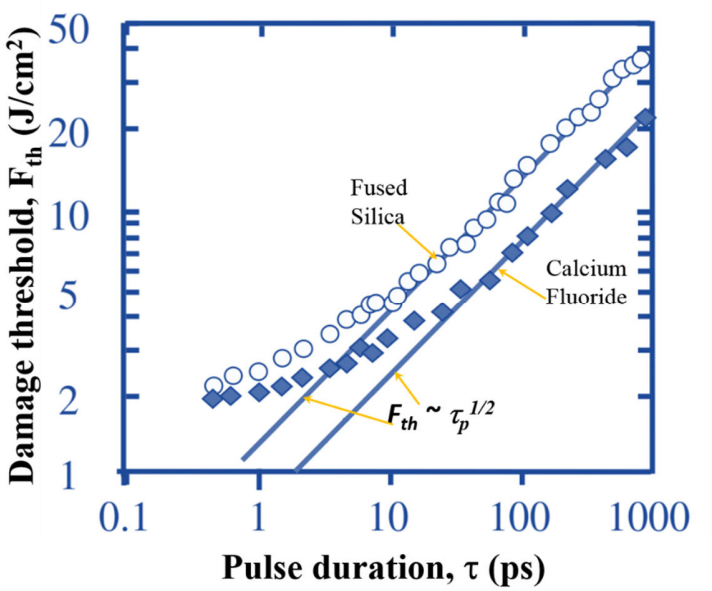

Figure 3 Dependence of the damage threshold on the pulse duration observed for the fused silica and calcium fluoride at 825 and 1053 nm wavelengths. The solid lines indicate the fits for $\tau^{1/2}$ [29].

The relative rate of the energy deposition and diffusion determine the damage threshold, and, as it is well known, the fluence necessary to induce optical breakdown scales with the square root of the pulse duration τ [32] (Figure 3). For pulses > 10 ps the peak laser intensity required to initiate the damage is not sufficiently high to directly initiate the photoionisation. Therefore, the seed electrons necessary for the avalanche ionisation are provided by the thermal excitation or impurity and defects.

The contrary situation is when the ultrashort pulses are used. The time needed to heat up the material up to the equilibrium temperature is much longer than the pulse duration. Therefore, the absorption and material heating processes are decoupled. Hence only after the pulse is passed, the energy is transferred to the material, and if a certain material-dependent energy threshold is exceeded, the permanent structural changes are initiated. For this case, the damage threshold is not influenced by seed electrons from impurity or defects required for avalanche ionisation. They are provided by the photoionization and makes the damage a deterministic process.

1.2 Types of transparent materials modification

In the bulk of transparent materials, usually three different types of material modification can be induced by using the femtosecond laser pulses: 1) the smooth, isotropic refractive index change; 2) the birefringent refractive index change and 3) the voids. In Figure 4, there are illustrated the energy dependent modification types in fused silica induced by the femtosecond laser pulses. In particular, the Type I modification (Figure 4b) is the one typically used for waveguide fabrication, while the Type II modification (Figure 4c) is the one employed in the first step of the FLICE technique for microchannel production. The Type III modification (Figure 4d) can be used for direct laser ablation and data storage.

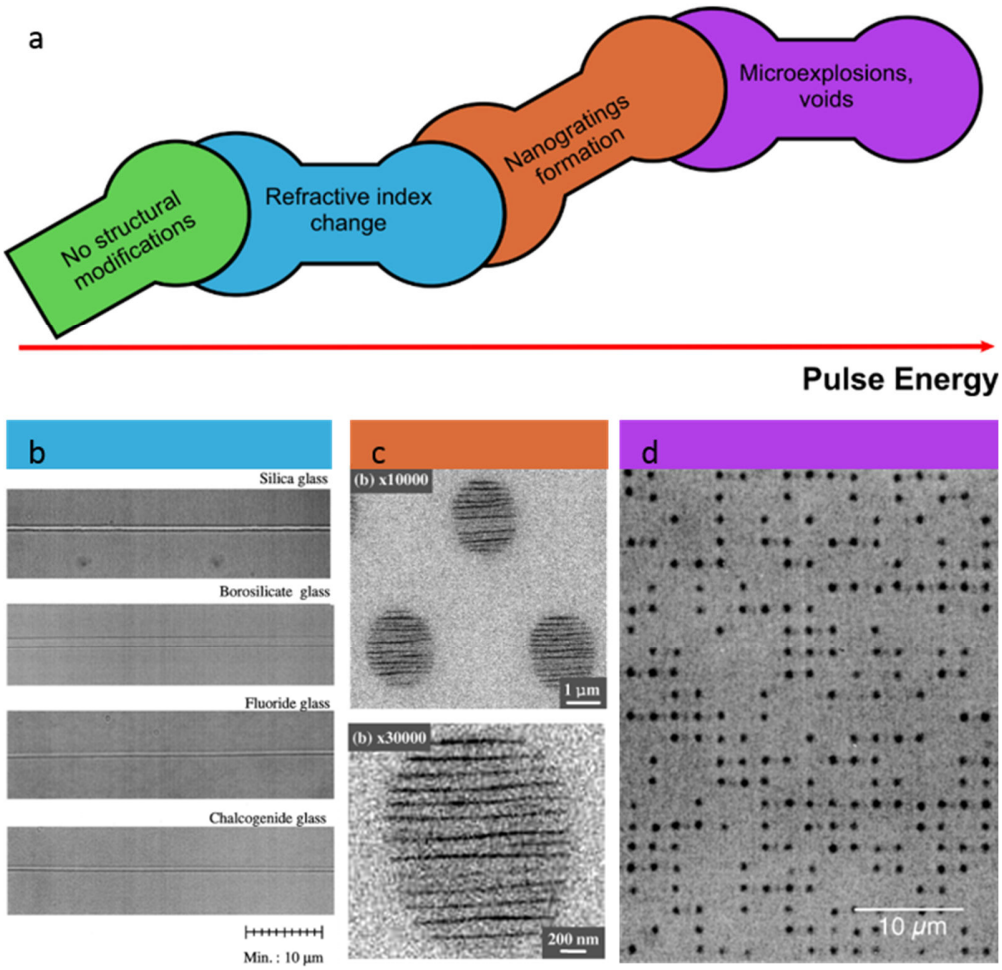

Figure 4 Material modification types evolution of (most) transparent glasses induced by the femtosecond laser direct-write technique (a). The three modification types are shown: (b) Type 1 – refractive index increase [33]; (c) Type 2 – nanogratings [14]; Type 3 – voids [6].

1.2.1 *Overview of surface ripples and subsurface nanogratings*

Five decades ago, the first observation of laser-induced periodic surface structures (LIPPS) on the surface of a semiconductor was reported by Birnbaum [34]. This followed the further observation of ripples in many materials starting from metals and ending on dielectrics. The surface ripples can be formed with all visible spectrum wavelengths up to the blue end of the visible spectrum and using laser working from CW to femtosecond. It was demonstrated that for the LIPPS structures the laser energy distribution on the surface is influenced by the angle

between the beam direction and the electric field direction [35]. The period of the surface ripples when the beam is directed by some angle to the surface for the p-polarized light (electric field in the plane of incidence) is close to the laser beam wavelength and has two possible periods with a strong dependence on the angle of incidence [36]:

$$\Lambda_{gr} = \frac{\lambda}{1 \pm \sin\theta'} \tag{1.5}$$

where θ is the angle of incidence and λ is the wavelength of incident laser light. For the s-polarized light, Λ_{gr} is comparable with the wavelength λ for small incidence angles.

A few different models have been proposed for the periodic nanostructures formation on the material surface. One is based on the interference that is created by the incident light and the light scattered by dust and impurities [37], and the other one suggests that surface plasmons or surface polaritons could produce ripples [38, 39]. The most widely accepted explanation is the interference between the incident and surface scattered waves formed by random variation of surface height, electron density, defects density or any other optically significant physical property [36, 37, 40, 41]. The sinusoidal light intensity variation is produced during interference that interacts with the material surface. Due to this modulation, the light is diffracted, and surface irregularities grow that further forms the periodic structure [42].

In 2003, the self-organized nanostructures were observed inside the silica glass after irradiation with a focused ultrashort pulse laser beam [14]. The structures initiated [43] the anisotropy and the anisotropic light scattering [44, 45]. In contrary to the surface ripples, the nanostructures inside of the material were found only for a few materials: fused silica, sapphire and some sorts of glass [46, 47]. A few years ago, the nanogratings were also observed in the bulk borosilicate glasses and ultra-low expansion glass (ULE) [48]. Nanogratings were also discovered in porous silica glass [49]. The volume nanogratings can be continuously transformed to the surface

ripples when the laser focus is translated in the vicinity of the sample surface [50]. As a consequence, some theories on the nanostructures formation try to reconcile the surface ripples and volume nanograting formation [51].

After detailed observation cross-sections of the internal modifications, the two periodicities were noted: perpendicular to the polarisation and along the light propagation direction (Figure 5) [52]. The first periodicity is in the plane perpendicular to the light propagation with the period ~ λ/2n depending on the experimental conditions. The second periodicity is observed basically on the initial part of the modified region with the period close to the light wavelength in the material.

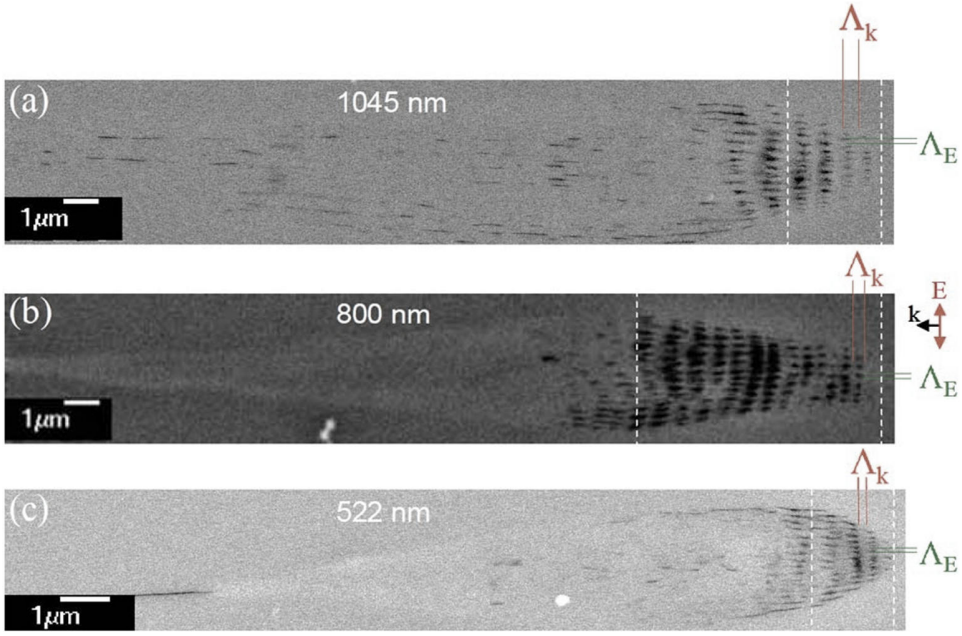

Figure 5 SEM images of nanogratings formed by three different central wavelengths of the irradiated laser pulses. E is the electric field of the writing laser; k is the wave vector of the writing laser beam. (a) τ_p = 520 fs, E_p=0.9 μJ, writing speed 200 μm⁄s, repetition rate 500 kHz. (b) τ_p=150 fs, E_p = 0,5 μJ writing speed 100 μm⁄s, repetition rate 250 kHz. (c) τ_p = 490 fs, E_p= 0.15 μJ, writing speed 200 μm⁄s, repetition rate 200 kHz. Reprinted from Yang et al. [52].

1.2.2 *Theory of nanograting formation*

The existing theories of the nanograting formation mainly concentrate to the explanation of the subwavelength periodicity on the plane perpendicular to the light propagation direction. There are a few models to explain the subsurface

nanogratings. The first model came from the traditional surface ripple theory [14] and is based on the interference of the longitudinal waves in an electron plasma with the incident light. The second theory relies on the nanoplasma formation [15]. There is also an alternative theory where the interaction and self-trapping of exciton-polaritons was suggested to explain the nanograting formation [53].

The highlights of a few approaches are presented in the next section, together with a discussion on their strengths, weakness, and future challenges.

1.2.3 *Interference-based theory*

The initial coupling is produced by inhomogeneities induced by electrons moving in the plane of light polarisation [14]. The periodic structures created by the interference pattern reinforce this coupling and, consequently, induce the periodic modulation of the electron plasma concentration and the structural changes in the glass. The periodic structures further grow exponentially and are embedded within the material. The period of the gratings is defined by the longitudinal component of the momentum conservation condition:

$$\vec{k}_{gr} + \vec{k}_{ph} = \vec{k}_{pl}, \tag{1.6}$$

where $k_{ph} = \omega n/c$ is the photon wavevector, $k_{pl} = \omega_{pl}/v_{pl}$ is the plasma wavevector and, consequently, the grating wavevector can be described as:

$$k_{gr} = \frac{2\pi}{\Lambda_{gr}} = \sqrt{k_{pl}^2 - k_{ph}^2}, \tag{1.7}$$

Finally, taking into account the momentum conservation relation and the dispersion relation, the explicit equation for the grating period Λ_{gr} can be obtained:

$$\Lambda_{gr} = \frac{2\pi}{\sqrt{\frac{1}{T_e}\left(\frac{m_e\omega^2}{3k_B} - \frac{e^2\eta_e}{3\varepsilon_0 k_B}\right) - k_{ph}^2}}, \tag{1.8}$$

According to (1.8), the grating period increases with the increase of the electron concentration and electron temperature (Figure 6). The rapid growth of the period occurs when the electron concentration η_e approaches the critical plasma density $\eta_{cr} \sim \eta_{cr} - 3\varepsilon_0 k_B k_{ph} T_e e^{-2}$.

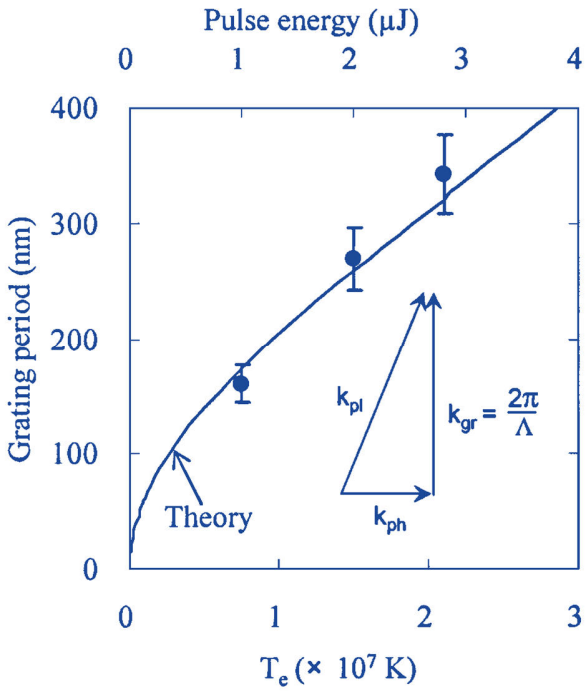

Figure 6 Evolution of the nanograting period predicted by the plasmon interference theory. The inset shows the wave vector matching diagram [14].

The one more prediction that comes from the model is the energy-dependent nanograting period that increases with the pulse energy. For a period of 150 nm recorded with the 800 nm wavelength ultrashort laser pulses, the realistic electron temperature $T_e = 5x10^7$ *K* and density $\eta_e = 1.75x10^{21}$ cm^{-3} were found. The micro-explosions induced by ultrashort laser pulses demonstrate the comparable conditions [54]. However, the nanogratings were observed even for the 100 nJ laser pulses meaning that the nanogratings can be assembled at the subcritical plasma concentration. The electron temperature is also limited by the band gap of the

materials (for silica glass it does not exceed 1.1×10^5 K) as the hot electrons dissipate their energy by the impact ionisation.

1.2.4 *Transient nanoplasmonic theory*

The further physical mechanism explaining the nanograting formation is based on the transient nanoplasmonic model studied in detail in [15]. The explanation comes through a few steps. Due to the presence of the defects or colour centres, the hot spots for multiphoton ionisation occur in the focal volume (Figure 7a).

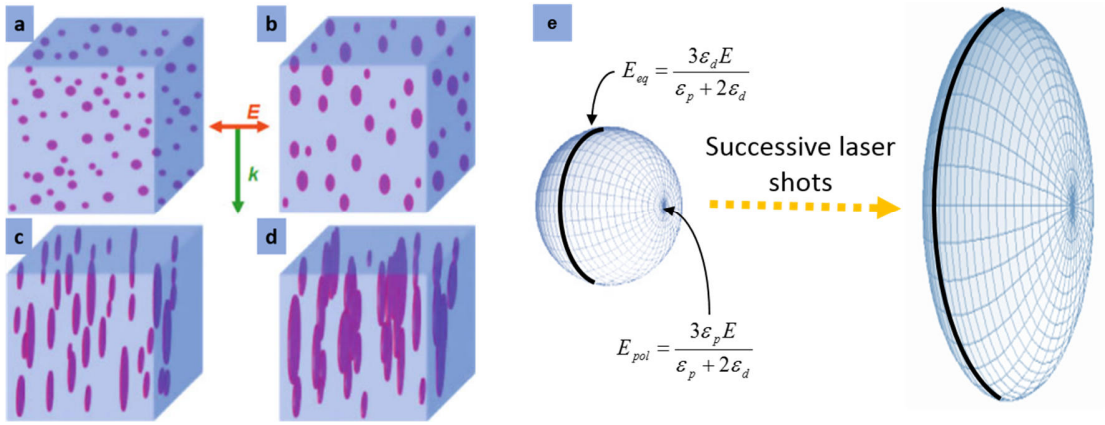

Figure 7 Illustration of the nanoplasmonic model explaining the evolution of the nanoplanes: (a) Randomly distributed underdense nanoplasma droplets; (b) Asymmetrically grow in the presence of the laser field over hundreds of laser pulses (c) to become ellipsoidal and (d) finally flatten and merge to become micrometer-sized nanoplanes; (e) Pictorial representation of the nanoplasma growth: field enhancements near the nanoplasma along the propagation direction force the expansion into a plane by ionization under the action of many shots [55].

The memory effect occurred due the successive laser pulses evolves the hot spots into spherically shaped nanoplasmas (Figure 7b) [56]. The local field enhancement at the boundary of the nanoplasma droplets results in an asymmetric growth of the initially spherical droplets in the direction perpendicular to the laser polarisation (Figure 7c) where the electric field at the poles E_{pol} and equator E_{eq} of the nanoplasma sphere will be the following (Figure 7e):

$$E_{pol} = \frac{3\varepsilon_p E}{\varepsilon_p + 2\varepsilon_d}, \tag{1.9}$$

$$E_{eq} = \frac{3\varepsilon_d E}{\varepsilon_p + 2\varepsilon_d}. \quad (1.10)$$

where ε_d and ε_p are the real parts of the electric permittivity for dielectric medium and plasma. The nanoplanes are initially randomly spaced when the electron concentration is below critical $E_{pol} < E_{eq}$. The electric field is enhanced at the equator leading to the nanoplane formation. Further, the nanoplanes become metallic and start influencing light propagation in such a way that they assemble in parallel nanoplanes which lead to a prediction of nanograting period equal to $\lambda/2n$. This theory has a difficulty when $\varepsilon_p > \varepsilon_d$ and electron density becomes higher than critical as a result of $E_{pol} > E_{eq,}$ and nanoplanes could not be formed [57].

1.2.5 *Alternative theories for nanograting formation*

The alternative nanogratings formation theory is based on the self-trapping of exciton-polaritons [53]. As it is known, the absorption spectra of SiO_2 are characterised by a strong exciton peak at $\hbar\omega_0$ = 10.4 eV [58, 59]. Two dispersion branches of the excitons–polaritons can be simultaneously excited by the multiphoton absorption [53] in the fused silica. Then, due to the interference of the exciton modes, the polarisation grating is formed. The recombination of the self-trapped excitons induces the generation of molecular oxygen due to the photosynthesis-like reaction [60]:

$$SiO_2 + X \rightarrow Si + O_2, \quad (1.11)$$

where X denotes an exciton. Nanopores of silica filled by oxygen are formed in the locations of high concentration of the self-trapped excitons. Agglomerations of these nanopores are responsible for refractive index change and induced birefringence in nanogratings observed in the experiments. Due the extremely short coherence time (<300 ps) of polaritons in glasses, the free excitons-polaritons are

transformed into indirect self-trapped excitons that freeze the polarisation grating pattern in glass [61].

It should be noted, that all of the reviewed theories are predicted only after the laser irradiation. However, it is not entirely clear how the nanogratings are formed in the matter during the irradiation. All of the theories predict that nanogratings are formed after a single pulse irradiation, but it is well known that the sequential pulses are required to initiate the nanograting formation. That aspect suggests the existence of some accumulation effects. The direct observations are desirable to have progress in the phenomena explanation.

1.3 Properties of fused silica

Most studies into the fundamental physical processes that occur at the laser focus have been conducted in fused silica. In comparison with other optical materials, fused silica was treated with a broad range of laser pulse frequencies, durations, energies, wavelengths and sample translation speeds. Furthermore, fused silica is easy to obtain in high purity forms as it is a popular UV optical material. The properties of fused silica are almost ideal for integrated micro-optical and micro fluidic circuits due to its wide transmission range (0.2 - 2.5 μm) in the visible and near infrared spectral range, resistance to high temperature and compatibility with biological materials. The band gap of fused silica is 9.1 eV.

The continuous random network of cross-linked SiO_4 describes the atomic-scale structure of the vitreous silica [62]. The network structure of fused silica is shown in Figure 8a. The closed paths of repeated Si-O segments create the n-membered ring structures, where n describes the number of Si-O segments. The computer simulation confirmed the existence of these rings structures [63]. It was determined that in fused silica, there is from three to nine-membered rings distribution with the most predominant five and six-fold structures. In the Raman experiments, it was found two peaks at 495 and 605 cm^{-1} [64–67] that correspond to the Raman active symmetric breathing modes of the oxygen atoms in the four- and three- membered

ring structures, respectively. The symmetric motion of the oxygen atoms is involved by the modes (Figure. 8b), and their decoupling from the rest of the network vibrational modes gives rise to the sharp profile of the 495 cm^{-1} and 605 cm^{-1} peaks. They are referred as D1 and D2 defect peaks. The assignment these peaks to the four- and three- membered ring structures was confirmed by Pasquarello et al. [63].

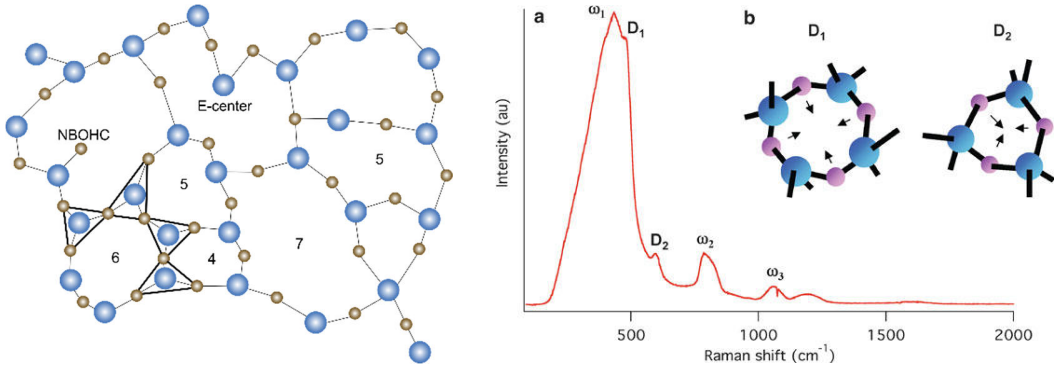

Figure 8 (a) Schematic presentation of the irregular network structure of fused silica. The coordination number of silicon atoms in fused silica is written in the network ring; (b) The Raman spectrum of the fused silica. ω1, ω2, ω3, are the vibrational modes of the silica network. D1 and D2 are the Raman active symmetric breathing modes of four- and three- membered ring structures.

The observed broad peaks at 440, 790, 1060, and 1200 cm^{-1} are assigned to the vibrations of the cross-linked glass network. The wide distribution of Si-O-Si angles in the network is explained by the broadness of the peaks.

The few types of defects can be found in fused silica. One of the most known defects are the dangling bond type defects (shown in Figure 8a). The E'-centre is assigned as a dangling Si bonds ≡Si● (≡ are three covalent bonds attached to three oxygen atoms, ● is alone unpaired electron) and the NBOHC (non-bridging oxygen hole centre) [62, 68, 69] is assigned as an oxygen dangling bond ≡Si-O●. These and other known defects in fused silica have characteristic optical absorption/excitation and fluorescence/photoluminescence (PL) bands. The most of the bands of the defects in vitreous silica are provided by Skuja et al. [70].

1.4 Microchannels formation and optimisation

In this section, the femtosecond laser based technology responsible for the microchannels formation in fused silica is reviewed. The main governing physical and chemical processes driving the selective etching are discussed.

1.4.1 *FLICE technology*

The polarisation dependent subsurface nanogratings imprinted into fused silica with femtosecond laser pulses are attracting due to their ability to induce selective chemical etching. The higher etching rate of the laser modified regions than the unexposed material is achieved by using dilute HF [71–74] or KOH [75]. A decade ago, the 70-fold increase in the HF etching for laser exposure with a linear polarisation perpendicular to the scan direction compared with parallel polarisation was demonstrated by Hnatovsky et al. [73]. They suggested that this selective etching is related to the formation of the subsurface nanogratings with the nano-planes aligned orthogonal to the polarisation direction. The experiments repeated with the circular polarisation showed the similar high contrast in the etching rate, however lower than for the perpendicular polarisation due to the disordered nature of the nanostructures. The main advantage of the circular polarisation is that the etching rate along the curved laser modification track is the same. The etching selectivity as high as 280:1 was reported between laser modified and unmodified glass [76] for the exposure with 40 fs pulses and energy of 200 nJ in the 2.5 % HF solution.

The embedded microchannel length is usually limited to < 4 mm because of the undesirable tapering and low control of the cross-sectional shape limit applications of FLICE for fabrication of LOC (Lab-on-chip) systems [73, 77]. The solution of tapering control was proposed by Osellame et al. They introduced the geometry compensation by the conical wobbling to create long straight and uniform cylindrical microchannels. However, this technique is not flexible for creating

complex cross-sectional shapes [78]. The almost uniform cross-section in the length of 9.2 mm was demonstrated in fused silica etched in a high concentration (10M) of aqueous KOH and a high temperature of 80 °C to gain the modest etching rate of ~ 1.7 μm/min [75].

The increased HF etching rate of fused silica following the femtosecond laser irradiation is due to the combination of several mechanisms [79]. A first one is related to densification of silica that decreases the Si–O–Si bond angle induced by the hydrostatic pressure or compressive stress created in the irradiated region [72]. Thus, the reactivity of the oxygen atoms is increased due to the deformed configuration of their valence band [80], and that increases the etching rate of laser-modified zones. This explanation is particularly suited for the low-intensity modification regime (Type I), where the formation of waveguides is observed. The second mechanism is suitable for Type II modifications and results in a much higher selectivity in the etching rate of the irradiated regions, when the self-ordered nanograting structures, perpendicular to the laser direction are formed [81].

The chemical process responsible for the dissolution of silica glass by aqueous HF is described by the following chemical equation:

$$\equiv Si-O-Si\equiv + HF \rightarrow Si-OH + \equiv SiF \qquad (1.12)$$

The F^- ions attack the silicon atoms, while the H^+ ions attack the oxygen atoms. For aqueous KOH, the hydroxide ion, OH-, attack the ≡Si-O-Si≡ groups, and the bounds are separated into ≡Si-OH and ≡Si-O^-. The exact mechanism at the molecular level is still under the debate.

The features of the FLICE process are following:

1) The process requires multiple femtosecond pulses impinging to the same spot to induce a cumulative action. Therefore, the processing window requires the right combination of the intensity and translation speed during the writing process.

2) To be properly triggered, the process requires the precise alignment of the writing laser polarisation with respect to the translation direction [81]. For the linear polarisation aligned perpendicularly to the translation direction, the nanogratings are directed along the channel axis, allowing easy diffusion of the etchant. For linear polarisation parallel to the translation direction, the etchant diffusion is blocked (nanogratings are perpendicular to the translation direction).

Based on the above explanations, the FLICE technique can be understood as follows: the nanogratings act as channels for the acid diffusion into the fused silica. The microchannels produced by the Type II modification yield much higher aspect ratios than those fabricated by the Type I modification due to the fast acid diffusion in the modified region instead of acid carving by progressively removing the irradiated material which takes place for the Type I modification.

The photo-structurable Foturan glass was also treated by the FLICE technique [82–84]. However, due to the entirely different laser-mater interaction where the Ce^{3+} ions donate an electron to Ag^{+} ions upon laser irradiation, and after the post-annealing process settles the colloidal Ag phase, the resolution is limited to a few microns. The etching contrast in 10% HF solution can be as high as 43:1 compared with unmodified glass.

1.5 Introduction to microfluidics

The microfluidics is the science and technology of manipulation fluids (gases, liquids) at the micron-scale in embedded channels [85]. It has a broad application in different fields, such as biology, chemistry, medicine and physical sciences. However, the main application of microfluidic is in the bio-chemical field where the main problem to solve is: how to make machines and devices that manipulate cells, proteins and other biological materials. The main goals of the microfluidics are the miniaturisation (smaller things tends to be faster, cheaper and use less power

and materials), parallelization and integration (combination of functions previously done on a separate device). Thanks to the evolution of the microfluidics field, the compact devices called lab-on-chip (LOC) were created, and many of the modern DNA sequencing schemes [86] and high-throughput screening assays [87] are available. The LOC microsystems are capable of integrating the whole biological or chemical laboratories in a single chip, where microfluidic channels and active and/or passive components, such as filters, valves or mixers can be integrated.

The flow in microsystems behaves completely different than flow on the macro-scale. The main difference is that in microfluidics the turbulence is absent. Here, the flow is smooth and laminar. Other important difference is that inertia forces are insignificant on the microscale and the viscosity becomes crucial. The mixing starts due to the diffusion that in microscale is an only minor influence. The interaction between the forces in microfluidics is completely different due to the reduced system size where the surface to volume ratio (S/V) increases dramatically as the system is downscaled. For example, the evaporation can become critical as the surface area increases leading to rapid changes in osmolarity. The fluid flow phenomena in microfluidics are described through dimensionless parameters such as Reynolds, Peclet or capillary numbers, which respectively relate inertial forces to viscous forces, convection to diffusion and viscous forces to surface tension.

1.5.1 *Review of microfluidics techniques*

The microfluidic devices can be fabricated by various technologies that are divided to conventional methods such as wet etching, conventional machining, photolithography [88], soft lithography [89], hot embossing [90, 91], injection moulding [92, 93], and direct laser writing techniques such as the FLICE technique [17, 94] and direct ablation [95] of glass in water (WAFLD) [96]. The methods are selected taking into account a few factors: preferred material, cost, speed and the fabrication capabilities (feature size and aspect ratio).

Many polymers were used to fabricate microfluidic devices. Very popular is optically transparent, soft elastomer polydimethylsiloxane (PDMS). However, it is permeable to many small and hydrophobic molecules [97]. Microchannels in PDMS are typically made using the soft lithography [98]. This technique can be cheap and very flexible, but the fabrication of the 3D microfluidic structures in the transparent substrate requires additional stacking and bonding processes that increase the total fabrication time [99]. A promising alternative FLICE technique to fabricate the fully integrated 3D structures of transparent glass materials that was reported first by Marcinkevičius et al. [17] and received strong development in the past few decades [84, 100–102]. Fused silica is the main transparent media in this technique due to its easy processing and high etching selectivity caused by the type II modification [55, 73]. The optical quality, chemical resistivity and flexibility of the FLICE technique are the key factors that stimulated the use of fused silica. The FLICE technique involves inscribing of 3D microchannels in a few steps that do not require any complex fabrication processes.

1.5.2 *Microfluidic flow dynamics*

The fluid flow is classified into two main groups: viscous flow and inviscid flow. An inviscid flow is assumed to have no viscosity, therefore in fluid dynamics, this approach is used to easily solved problems where the viscous effects can be neglected. In the viscous flow, the viscosity is the friction between the adjacent layers of fluid that moves parallel to each other. The fluid viscosity is primarily responsible for the turbulent flow due to the energy losses associated with a transport of the fluid in a channel. The majority of known liquids are viscous, e.g., air and water [103].

The fluid flow in microscale dimensions is very smooth and is characterised with almost no mixing between neighbouring fluid particles except through molecular diffusion. This flow is called laminar flow. In a turbulent flow, the random variation

in time of the fluid velocity and pressure is characteristic due to the irregular variation of the fluid motion.

The fluid flow is characterised by the main three parameters: the length scale of the flow field (the channel width/diameter), the spatial average of the flow velocity, and the kinematic viscosity, which is the ratio of the viscosity and the density of the fluid. In the case, when length scale or velocity is large enough, the flow may be turbulent. The same statement is also valid when the kinematic velocity of the fluid is very small. All that simple fluid parameters are necessary to get information about the flow in microsystems. If we take the ratio of the inertial forces to the viscous forces the dimensionless, a single number called Reynolds number [104] can be introduced and allows to identify the type of flow in the system. The Reynolds number is expressed as

$$\mathrm{Re} = \frac{VL}{\nu} = \frac{\rho VL}{\eta}, \tag{1.12}$$

where L is the characteristic length, V is the average velocity of the moving liquid, ν is the kinematic velocity, ρ is the density and η is the viscosity. The critical Reynolds number Re_{crit} can be introduced that shows the boundary between the laminar flow if $\mathrm{Re} < \mathrm{Re}_{crit}$ and turbulent flow if $\mathrm{Re} > \mathrm{Re}_{crit.}$ The flow regime is typically divided in three cases based on Reynolds number values: for Re < 2000 the flow is laminar, for Re > 4000 the flow is turbulent and for flow between 2300 and 4000 the so-called transitional flow appears, where the flow type is determined by the surface defects [105]. Figure 9 shows the example of the laminar and turbulent flows.

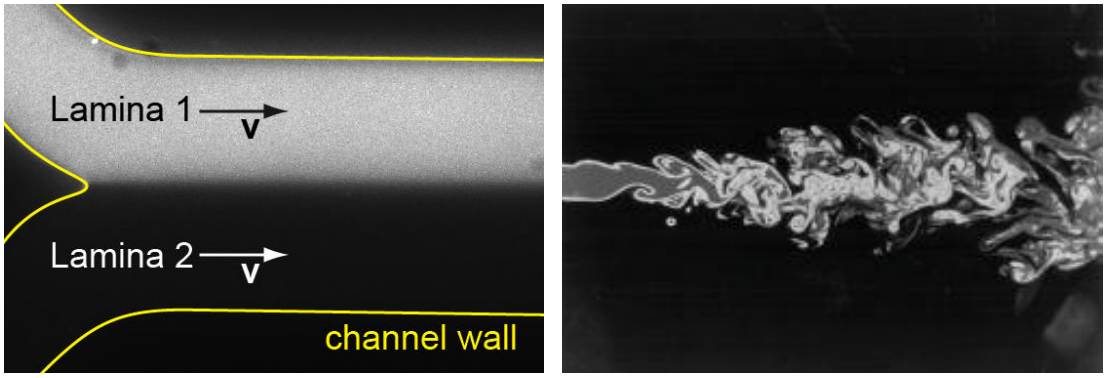

a) b)

Figure 9 The laminar (a) and turbulent (b) flow demonstration in the fluids [106, 107].

For the non-compressible Newtonian fluids, such as water, the relation of the fluid velocity ant the fluid pressure is described by the Bernoulli equation:

$$\frac{V^2}{2} + \frac{p}{\rho} + gh = const\ , \tag{1.13}$$

where V is the average velocity of the fluid, p is the pressure, ρ is the density, g is the gravitational acceleration, and h is the height. The Bernoulli equation can be derived by applying the Newton's second law of motion to a fluid particle.

In order to analyse the fluid flow dynamics in microsystems, the Navier-Stokes approach should be introduced. An infinite-small element of fluid is affected by a stress field σ (force per unit area), which is due to the fluid itself, and by an external forces acting on the same fluid element. The velocity field exerted by these forces for a Newtonian fluid can be determined by the Navier-Stokes differential equation, which is built on the fundamental laws of conservation and is the rewritten version of the 2nd Newton's law **F** = m**a**:

$$\rho\left(\frac{\partial v}{\partial t} + v \cdot \nabla v\right) = \nabla\sigma + f = -\nabla p + \eta\nabla^2 v + f\ , \tag{1.14}$$

where p is the pressure and η is the viscosity, which depends on the system characteristics. To finalise the equations describing the simple incompressible fluid,

the continuity equation should be taken into account. This equation expresses the conservation of mass that is still valid even in the continuous case:

$$\frac{\partial \rho}{\partial t} + \nabla \cdot (\rho v) = 0 , \tag{1.15}$$

For incompressible fluids (like water) the continuity equation is simplified and is:

$$\nabla \cdot v = 0 , \tag{1.16}$$

which means that the fluid cannot arise from anywhere and cannot vanish into anywhere. For the microfluidic case, the inertial forces are small compared to the viscous forces. Thus the nonlinear term in the Navier-Stokes equation can be neglected and is transformed to the simpler Stokes equation:

$$\rho \frac{\partial v}{\partial t} = \nabla \sigma + f = -\nabla p + \eta \nabla^2 v + f , \tag{1.17}$$

As the fluids are made of molecules, the diffusion take place both with the fluid molecules and with particles and tracers dispersed in it.

1.5.3 ***Diffusion in microfluidics***

The mixing at the macroscale is explained by the turbulence that initiates the vortices during the fluid flow, however, when the dimensions fall down to the microscale, only laminar flow occurs. Thus the turbulence is neglected, and the main mechanism responsible for the mixing is the diffusion. Diffusion phenomenon is the stochastic process in which molecules drift from one region to another. Each molecule moves in one direction until it hit by another molecule and changes its motion direction. The diffusion in one dimension can be considered as the following equation:

$$d = \sqrt{2Dt} , \tag{1.18}$$

where *d* is the average distance moved by particle during the time *t* and *D* is the molecular diffusion coefficient of the material in units of (m^2/s). D expresses how fast a concentration diffuses a certain distance. The fluid movement due the diffusion is described by the Fick's law which postulates that the solute moves from a region of the high concentration to a region with the lower concentration across a concentration gradient:

$$\frac{\partial c}{\partial t} = D\nabla^2 c\,, \tag{1.19}$$

where c is the concentration and $\nabla^2 c$ is the spatial gradient of the concentration.

The nature and the strength of the diffusive mixing can be characterised by the dimensionless number called the Peclet number defined as the ratio between the advective and diffusive transport, and it is given by:

$$Pe = \frac{VL}{D}\,, \tag{1.20}$$

For a larger Peclet number in a given system, the diffusion is going to be less and less important. It can be noted that for the Peclet numbers higher than 1000 diffusion can be neglected, however, when the Peclet number is less than 10 then the diffusion is the dominating mechanism and the advection can be neglected.

1.5.4 *Surface effects*

An important consequence of the scaling of the dimensions is the increase in surface-to-volume ratio, which makes of primary importance the surface effects influencing the flow motion, such as surface tension or capillary forces. In fact, at the micro-scale, surface forces are so prominent in comparison to other forces that a liquid flow can be confined, controlled and even manipulated. This effect has been studied for example in the generation of controlled monodisperse microdroplet between two immiscible fluids [108].

2 Used methods

The femtosecond laser micromachining system used for most of the experiments with fused silica glass is described in this chapter. After laser fabrication, the fused silica sample should be post- processed to reveal the microchannels or nanograting structure depending on the investigation aims. The procedures such as chemical etching and precise sample polishing are described in Section 2.2 to make clear the entire procedure.

The etched microchannels have different dimensions and lengths. Thus the methods how to qualitatively and quantitatively estimate the microchannel characteristics such as length and etching selectivity is described in Section 2.3.

The revealed subsurface nanogratings were measured with SEM microscope, and the tilt angle measurement is introduced. As the pulse duration is one of the most important parameters during the nanograting tilt angle investigation, therefore, its measurement techniques are described more detailed in Section 2.4.

Finally, in the last thesis section, the various microfluidic devices are studied. For different devices, various output characteristics should be estimated. For that purpose, the characterization setup used for waveguides characterization and estimation of the focusing characteristics of the microfluidic lenses was designed.

2.1 Laser micromachining system

The laser micromachining system is the main tool involved to realise the aims of the current thesis. The used system is custom developed by the ELAS company and assembled by the author. The experiments performed with the current laser micromachining system are presented in Chapters 3, 4, and 5.

For fabrication of microchannels and subsurface nanogratings, radiation of first (1030 nm) and second (515 nm) harmonics from the ultra-short pulse, diode-pumped, mode–locked Yb:KGW laser (Pharos, Light Conversion) was utilised. It

was attenuated with a motorised Brewster angle attenuator and delivered to the 50x or 10x microscope objective (Olympus LMPlan, NA 0.55; Olympus, NA 0.25) which focused the laser beam inside the bulk fused silica sample. Linear or circular polarisation of the laser beam was controlled during the experiments with a setup formed of the zero-order λ/2 or λ/4 phase plates mounted in mechanical rotation holders. The linear polarisation orientation before the laser processing was calibrated with the Glan prism polarizer and the half-wave plate. In this way, the half-wave plate was oriented to get perpendicular or parallel polarisation to the writing direction. The nanometer resolution positioning stages ANT130 (Aerotech) were used to translate the fused silica substrate in X and Y directions under the laser beam. Laser writing was performed at the scanning speed varying from 0.025 to 10 mm/s in the directions (x or y) perpendicular to the laser beam propagation (z). In order to control the accurate sample positioning, the off-axis machine vision system with a coaxial lighting and charged coupled device (CCD) camera were installed.

Figure 10 Optical design of the laser micromachining system (left) and laser micromachining system picture (right).

Part of experiments was performed with the optical setup similar as shown in Figure 10 at Politecnico di Milano. The femtoREGEN HighQ laser (two harmonics at the 1040 nm and 520 nm wavelengths) was used. This is an ultra-compact laser

system based on an Yb:KYW chirped-pulse regenerative amplifier using the intra-cavity stretching to allow an ultra-compact design, flexible repetition rates up to 2 MHz with pulses as short as 350 fs. The used laser can set repetition rate up to 1 MHz that allowed to look on to etching selectivity when the heat accumulation effects started to be more visible [109]. The experiments performed with that laser are presented in Sections 3.4 and 4.1.

2.2 Sample preparation and etching procedures

For all experimental work presented in this thesis, the commercially available fused silica samples (JGS1, Eksma Optics) were used. Dimensions of the samples were 15x4x2 mm^3, 20x15x2 mm^3, and 20x15x1 mm^3 depending on the structure needed to fabricate. The sample was mounted on the positioning stages with the double side tape and tilted to get the precisely horizontally orientated sample. Before the laser processing, the sample was cleaned with pure acetone to remove all residues and dust from the sample surface.

The etching was performed by immersing the sample in the diluted HF acid. Various concentrations of the acid from 1 to 20 % were used depending on the application. The 1 to 5 % HF concentration was used to reveal the nanograting structure and etching time was from 1 to 5 min. The 5 to 20 % HF concentration was used for microchannels and 3D structures etching. The initial etching experiments were performed without ultrasonic bath at the room temperature. The required etching time was 1- 14 hours. Further, the ultrasonic bath was used in the etching experiments. The HF acid was heated to 35-70 °C and etching took place up to 5 hours depending on the sample complexity.

2.3 Estimation of the etching length and selectivity

The length of the etched microchannels was measured by an optical microscope and analysed with a freeware software “Gwyddion”, and etching selectivity was calculated according to the following formula:

$$S = \frac{\frac{L}{t} \cdot 60 + r_0}{r_0}. \qquad (2.1)$$

where L is the etched line length, t is the etching time in hours, r_0 is the etching rate [µm/h] of unmodified fused silica. The etching length of unmodified fused silica was calculated by two ways: 1) measuring the width of etched microchannels and subtracting the modified line width before the etching and 2) measuring the cone angle of the etched channels and calculating the etched length of the unmodified fused silica according to the trigonometrical rules of the right triangle.

2.4 Pulse duration techniques description

There are various laser pulse duration measuring techniques, however, to measure the duration of ultrashort laser pulses (< 10 ps), the nonlinear optical autocorrelation techniques should be used. Two different methods for the pulse duration measuring were used in the experimental works: a single-shot autocorrelation for the pulse duration and pulse front tilt measurement and the second harmonics frequency optical-gated (SH-FROG) technique for the pulse duration and temporal chirp measurement. More detailed description of that techniques is provided in the next section.

2.4.1 *FROG technique*

Frequency-resolved optical gating (FROG) can successfully and efficiently record pulse characteristics by the overlapping split and partially delayed duplicate laser pulses in a nonlinear optical medium such as second-harmonics (SHG) crystal

[110]. When the pulses are overlapped in the crystal, a frequency-doubled pulse of light is produced that is encoded with the necessary characteristics of the initial laser pulse [111].

In the FROG technique, the laser pulse is separated into two pulses, and they intersect in a nonlinear optical medium (Figure 11). The nonlinear signal is spectrally resolved for various time delays between two beams. For the SHG FROG case, the envelope of the nonlinear signal field has the shape:

$$E_{sig}(t,\tau) = E(t)E(t-\tau), \tag{2.2}$$

where *E(t)* is the complex envelope of the pulse to be measured and τ is the delay between the two beams. This signal is used as the input to a spectrometer, and the intensity is detected by a photodiode or CCD array

$$I_{FROG}(\omega,\tau) = \left| \int_{-\infty}^{\infty} dt E_{sig}(t\ \tau) \exp(i\omega t) \right|^2 = \left| E_{sig}(\omega,\tau) \right|^2. \tag{2.3}$$

The FROG signal is a positive real-valued function of two variables: the frequency and the time delay between two pulses. This experimentally determined FROG signal is used as an input to a numerical algorithm, which determines the full complex electric field, i.e. both the intensity and the phase, of the pulse that created the FROG signal.

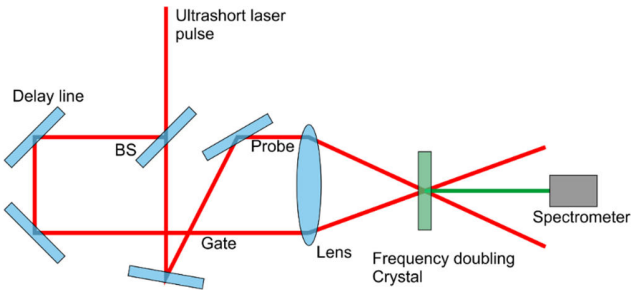

Figure 11 SHG FROG experimental setup.

The signal field of (2.3) is invariant with respect to a change of the sign of the delay time τ so that the SHG FROG signal is always symmetric relative

τ: $I_{FROG}(\omega, \tau) = I_{FROG}(\omega, -\tau)$. This temporal ambiguity is the main shortcoming of SHG FROG compared with the $\chi^{(3)}$ FROG method. The SHG FROG cannot distinguish between a pulse and its time-reversed replica.

2.4.2 *Single shot autocorrelation*

For high repetition rate ultrashort pulse lasers, there is not much variation from a pulse to pulse. As a result, the pulse spectrum can be obtained by scanning a monochromator in time or by leaving the shutter open on a camera or diode array at a spectrometer output and averaging over many pulses. Similarly, the delay in an autocorrelator may be scanned in time with confidence that pulses are not changed during the scan.

Some amplified laser systems have considerably lower pulse repetition rates, however, and the non-negligible pulse-to-pulse variations are expected. In this latter case, we should use a single-shot method. It is easy to obtain a single-shot spectrum, simply by opening the spectrometer camera shutter for only a single laser pulse. The single-shot autocorrelation, however, is more complex because the delay must somehow be scanned during a single pulse.

A single-shot autocorrelation signal is obtained by mapping the delay onto the position and spatially resolving the autocorrelation signal using a camera or array detector. This involves crossing two laser beams in the nonlinear-optical crystal at a large angle, so that, on the left, one pulse precedes the other, and, on the right, the other precedes the one [112–114]. In this manner, the delay ranges from a negative value on one side of the crystal to a positive value on the other. Usually, we focus with a cylindrical lens, so the beams are line-shaped in the crystal, and the range of delays is larger.

2.5 Fabrication of sub-surface nanogratings

Two different femtosecond lasers were used to record the sub-surface nanogratings:

(1) Pharos (Light Conversion) with the wavelength of 1030 nm or 515 nm, and the 260 fs laser pulses at the 500 kHz repetition rate and the scanning speed of 0.25 mm/s and 1 mm/s;

(2) FemtoRegen (HighQ Laser) 1040 nm, 317 fs at the 500 kHz repetition rate and the scanning speeds from 0.25 to 5 mm/s.

Focusing was carried out in the case (1) with a 50× objective lens of numerical aperture NA = 0.55 (Olympus LMPlan). For the case (2), the employed objectives had NA = 0.6 at 50× magnification (Leitz Wetzlar) or NA = 0.4, at 20× (Olympus LMPlan).

For the nanograting tilt investigation, the radially oriented lines starting from a common centre were inscribed. The scan direction of each line was from the center to outside, and in this way, the *star* pattern was formed (Figure 34c). The angle between subsequent ray orientations was $\Delta\varphi = 15°$, and the *star* pattern was formed from 24 lines in total.

To investigate the influence of the pulse duration and the pulse front tilt on the etching selectivity and nanograting orientation, six different pulse durations with negatively and positively chirp were used: 743 fs, 436 fs, 338 fs (negative chirp), 264 fs (bandwidth limited), and 357 fs, 630 fs (positive chirp).

The pulse energy was measured after the objective lens at the sample position to exclude any absorption and reflection/scattering losses caused by optical components. Nanogratings were recorded in a multi-shot exposure regime, e.g., for a typical spot diameter at the focus of 2.5 μm (1030 nm), 500 kHz laser repetition rate and a typical scan speed of v = 1 mm/s. There were $N \cong 1.3\times10^3$ pulses per

spot. For the 515 nm irradiation, the typical number of pulses per spot with the scan speed of v = 0.25 mm/s was up to $N \cong 2\times10^3$.

Nanogratings were recorded at the 10 μm depth below the surface of the ultraviolet-grade fused silica (JGS1), and samples were mechanically polished to the depth of the strongest modification.

A short immersion into 1% or 5% wt. aqueous solution of HF for 5 or 1 min correspondingly was used to reveal a surface morphology by scanning electron microscopy (SEM); a 5-10 nm thick gold coating was used for SEM imaging.

2.6 Nanogratings quality

The nanogratings quality can be understand by different ways, however, in our case, we use a visual inspection of the SEM pictures to predict the quality. The high-quality nanogratings were well distinguished and highly ordered. When the ordering and period of the nanogratings appeared hard to predict, and the width of the single grating fluctuated we call them as low-quality nanogratings. The quality of the nanogratings can also be predicted from the birefringence measurements. In our case, when the modified area in the sample was placed between two crossed polarizers in a microscope, the nanogratings which appeared bright were predicted as of high quality. When the uneven structure and no bright regions were observed the nanogratings were predicted as of low quality.

2.7 Characterization setup for optofluidic devices

The microfluidic devices were characterised by the setup presented in Figure 12, where the beam from the He-Ne laser was directed to the microfluidic device mounted on the high-precision 3 axis positioning stage to adjust the device position relative to the laser beam. From the opposite side of the sample, the registration of optical signals was performed. For that, the 10x microscope objective mounted on the translation stage along the beam propagation, the 200 mm focal length lens and CCD beam profiler were used. The CCD profiler recorded the near field intensity

profile. Depending on the microfluidic device type, the beam was directed through the devices in a few ways: the fibre coupling, the coupling with the microscope objective or simply illuminating the device without any objective.

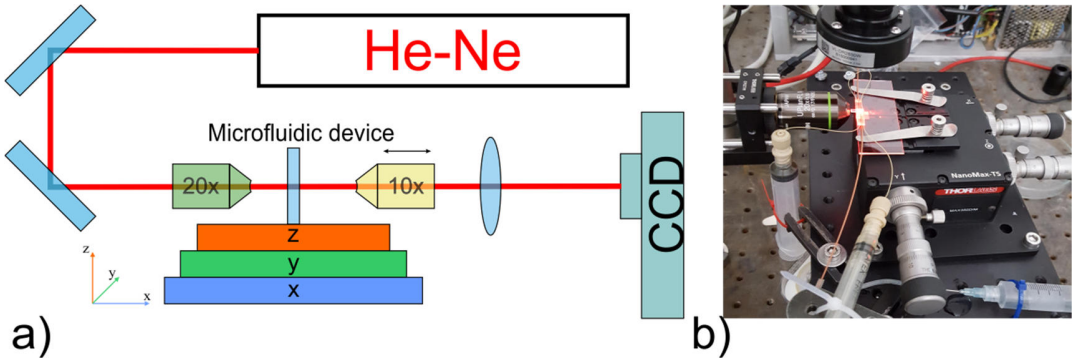

Figure 12 The characterization setup of the microfluidic devices: (a) schematic design; (b) camera photo.

3 Formation of microchannels in fused silica

The results presented in this section are published in the article [P1].

Many microchannels inside fused silica were formed to find the optimal laser writing and etching conditions for fabrication of the complex devices inside the fused silica block. This section is separated into few main parts: laser writing of modifications in the bulk of fused silica with various processing parameters and inspection, sample preparation for etching, etching optimisation and investigation of etching selectivity.

During last decade, numerous works were reported on the microchannels etching in transparent materials [71, 115]. The etching of microchannels can be performed in a few different glasses [71, 94, 116] and few different etching solutions as Hydrofluoric (HF) acid [17] and Potassium hydroxide (KOH) [75] or hybrid etching using both solutions [117]. Both etching solutions were tested in our work. However, HF was selected as the main one, and most of the etching work was done with the HF acid of various concentrations. The individual, single-line and rectangular microchannels by stacking the individual channels were formed inside the fused silica at different depths (from 50 µm to 500 µm below the sample

surface). The microchannels were recorded with various pulse energy, wavelength, processing speed, pulse duration and frequency to find the processing window.

3.1 Influence of polarisation to the etching selectivity

As it is widely known, the II type modification [73] inside fused silica should be formed to initiate the selective material etching. According to the investigations, the etching selectivity is maximal for the polarisation ~ perpendicular to the writing direction [81], however, in the intermediate polarisation state between the parallel and perpendicular polarisation to the writing direction, the etching selectivity has intermediate values. Thus for the first approach, the modifications with different linear polarisation orientation [118] starting from parallel to the writing direction, X-axis (0˚ angle of λ/2 phase plate) and ending perpendicular to the writing direction, X-axis (at 45˚ λ/2 phase plate angle) were formed. The increment step of the λ/2 phase plate was set to 5˚. In this way, 10 modification lines with 3 different pulse energies (264, 372 and 466 nJ with a laser fluence ranging from 7.6 to 13.4 J/cm^2) were prepared. The modifications were formed ~ 220 µm below the sample surface.

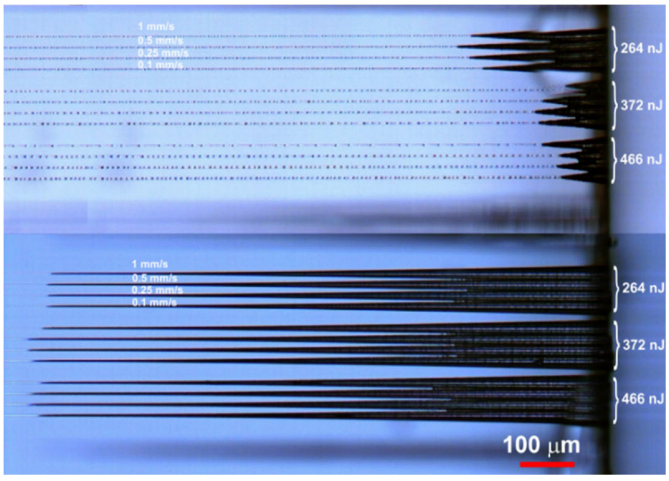

Figure 13 The single-line microchannels inscribed in the fused silica sample. Polarisation was parallel (top) and perpendicular (bottom) to the writing direction. Laser pulse energy: 264, 372, and 466 nJ from top to bottom between a set of 4 lines; writing speed: 1, 0.5, 0.25, and 0.1 mm/s from top to bottom in each set). Etching in 15% HF acid for 6 hours.

The embedded and etched microchannels formed with the polarisation parallel and perpendicular to the writing direction are shown in Figure 13. As it can be expected from the results reported in [81], the minimal etching selectivity was for the polarization parallel to the writing direction due to the nanograting formation perpendicular to the writing direction. When the angle of the nanograting planes changes from 0˚ to 90˚, the etching conditions changed and facilitated acid penetration leading to a higher etching selectivity (Figure 14).

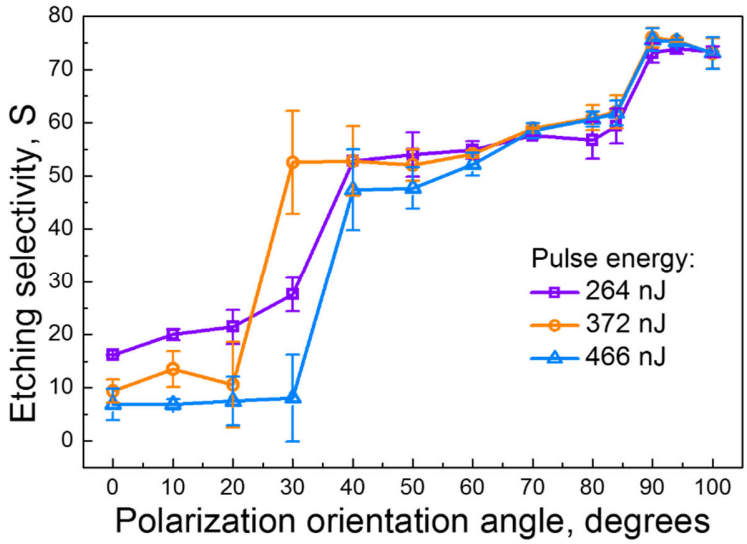

Figure 14 Etching selectivity versus polarization orientation relative to the writing direction (writing speed 250 µm/s, laser repetition rate 500 kHz, etching in 15% HF acid for 6 hours).

The maximum etching selectivity was achieved when the nanograting orientation angle approached to be ~ parallel to the writing direction, and it was > 75:1. For the tested pulse energies, the etching selectivity was of the similar level, that speculates that the nanogratings have the similar quality, however, for the minimal etching selectivity when the linear polarization was parallel to the writing direction, the etching selectivity was bigger for the lower pulse energy (S~16:1), and for the maximal pulse energy of 466 nJ, it was S~ 7:1. This behaviour briefly can be explained by the nanograting quality (mentioned in Section 2.6) that is better for the lower pulse energies [81] and dependence of the nanograting orientation on the pulse energy which is discussed in Chapter 4. Due to the manual polarization

adjustment, the phase plate orientation error appeared, and, in our case, for the lowest pulse energy, the nanogratings were orientated slightly out of the perpendicular direction. The increased pulse energy induced the tilt of the nanogratings in a clockwise direction [119], and that accelerated the nanograting rotation to the perpendicular to the scan direction orientation, and, consequently, the lower etching selectivity was observed.

The polarization angle should be quite precisely adjusted to get the expected maximal etching selectivity. The experiments demonstrating the precision of the polarization to scan direction angle setting was performed by keeping the polarization orientation constant and changing the scan angle by forming, in this way, a fan structure [120]. According to that results, to get the etching rate in the range of 96% of the maximum value, the linear polarization should be precisely oriented with deviation only ~ 2˚ angle.

3.2 Etching with different pulse duration

The pulse duration is one more additional degree of freedom that influences the structural changes in fused silica. It was noted, that depending on the pulse duration, the different morphology of the nanogratings can be achieved [121]. Thus, consequently, it induces different etching characteristics which extend the processing window for the microchannel fabrication.

3.2.1 *Influence of the pulse duration on the etching rate*

Since the distance of the diffraction gratings in the used laser compressor have the ability to be changed, consequently various pulse durations can be achieved. Based on the information mentioned above and report [122] indicating that for the longer pulse duration the etching selectivity can be improved, it was decided to inscribe the internal microchannels with various pulse durations. The positively and negatively chirped pulses with two different wavelengths (515 nm and 1030 nm) were used. The pulse duration of the Pharos laser was measured with SHG-FROG

(EKSPLA) and a single shot autocorrelator (TiPA, Light Conversion) (Section 2.4). Figure 15 depicts the laser pulse duration, and pulse temporal chirp dependence on the distance between the gratings measured in internal compressor units counts.

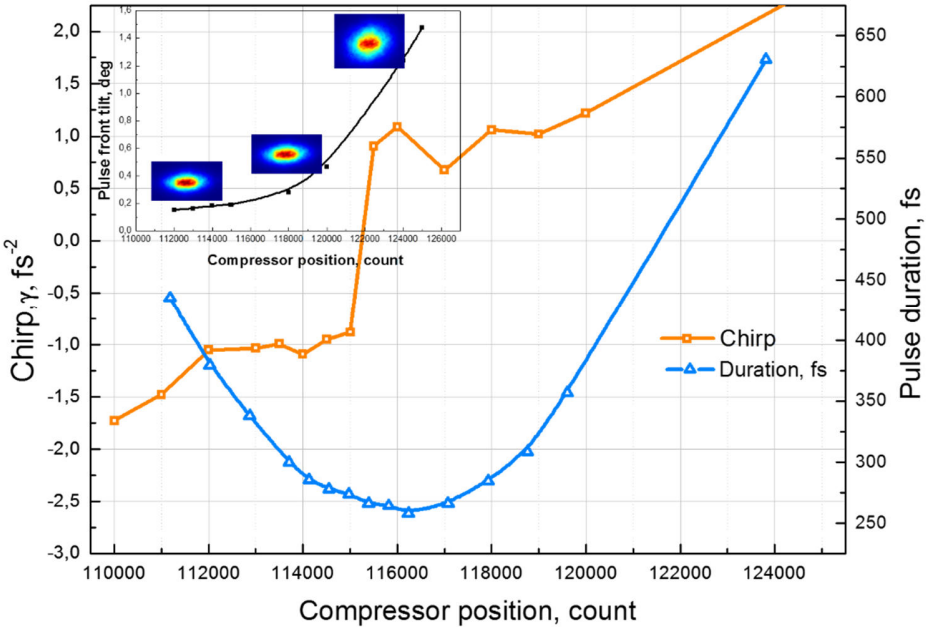

Figure 15 The pulse duration and chirp parameter dependence on the distance between the gratings in the laser compressor. Pulse duration was measured with the SHG-FROG technique.

The shortest pulse duration corresponds to the “neutral” chirp parameter. For negatively and positively chirped pulses, the pulse duration increases.

For the first experimental setup, the 515 nm wavelength was used. The microchannels etching investigations were performed with different pulse durations, starting from 1055 fs (negative chirp, 98000 compressor position) and ending at 2250 fs (positive chirp,148000 compressor position) with 5000 counts incremental step. The modifications were formed at the constant writing speed of 0.25 mm/s (2000 pulses/µm at the 500 kHz repetition rate) and ~ 400 nJ pulse energy for the shortest pulse duration. By changing the pulse duration, the efficiency of the second harmonic generation changes, which lead to the different

pulse energy and, consequently, the writing pulse intensity of each channel. The inscribed modifications are shown in Figure 16.

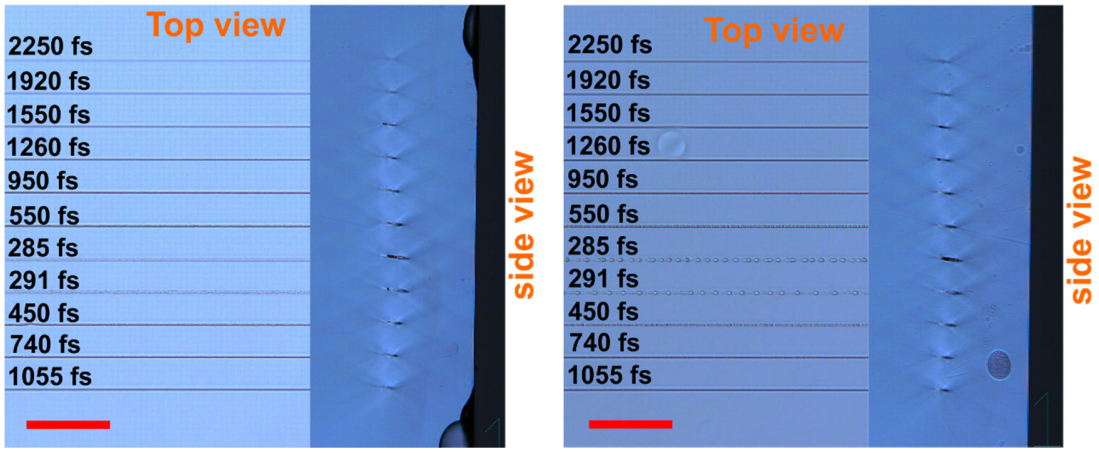

(a) (b)

Figure 16 The modifications inside fused silica fabricated with different pulse durations started from 1055 fs at negative chirp and ending at 2250 fs at positive chirp: (a) modifications with perpendicular polarization top and side view; (b) modification with parallel polarization top and side view. Pulse density 2000 impulses/µm, pulse energy. Respectively: 148, 192, 270, 466, 404, 254, 180, 142, 112, 94, 80 nJ. The red scale bar represents 100 µm length.

The morphology difference for the perpendicular and parallel polarization can be observed. For the parallel polarization, the bubble formation was noticed for the shortest pulse duration. The prepared sample with embedded modifications was side-polished to ensure the initial acid contact with the modification and was rinsed to 10 % HF acid for 6 h etching. The etching results are shown in Figure 17.

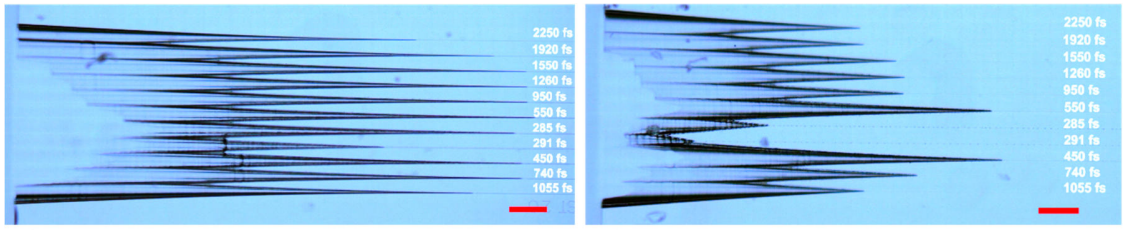

a) b)

Figure 17 Etching results of modifications formed with a) polarization perpendicular to the scan direction ($\mathbf{E}_y$, along y axis) and b) polarization parallel to the scan direction ($\mathbf{E}_x$, along x). 6 h etching in 10% HF acid solution. The red scale bar represents 100 µm length.

The etched length for the perpendicular polarization was larger for the longer pulses, and the minimum etched line length was observed for the shortest pulse duration. The same behaviour was observed for the parallel polarization. However, in this case, the etched line length was much shorter than that for the perpendicular polarization. It should be noted, that for longer pulses, the etched channel length was big enough even for the parallel polarization. The further investigations were performed to figure out the detailed influence of the pulse duration and different wavelengths to etching rate and selectivity.

3.3 Etching selectivity investigation with 515 nm

The more detailed investigations of the etching selectivity dependence on the pulse duration were done by writing microchannels at ~ 100 µm depth under the sample surface. To get more smooth etching, the channels were separated in the middle by a series of perpendicular modifications in the vertical plane (further it will be named – "wall"). The height of the wall started from the microchannel depth to the sample surface with the material damage on the surface. The wall is required to allow the acid to reach all the microchannels at the same time and induce the even etching in both directions. This involved the observation of etching in two directions. The set of lines with different pulse energies: 100 nJ, 200 nJ, 400 nJ, 600 nJ, 800 nJ and 1000 nJ and different writing densities: 100, 500, 1000 and 2000 pulses/µm were fabricated for six various pulse durations. The shortest pulse duration of 264 fs corresponded to the 115500 compressor length. Since the intensity of the 515 nm radiation drops down for longest pulses, and the maximum required pulse energy of 1000 nJ needed to be achieved, the writing frequency was set to 200 kHz instead of 500 kHz, to increase the pulse energy. The pictures of the microchannels etched in 15% HF acid for 30 min in the ultrasonic bath are shown in Figure 18.

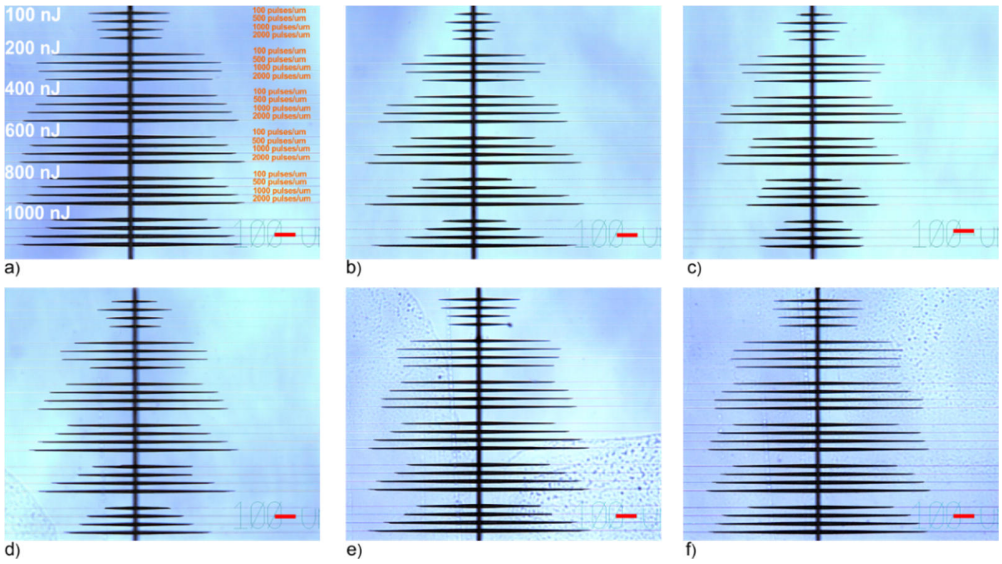

Figure 18 The microscope pictures of the microchannels etched in 15% HF acid solution for 30 min and written using different pulse durations: a)743.6 fs (-); b) 435.5 fs(-); c) 337.9 fs(-); d) 264.3 (0) fs; e) 356.8 fs and f) 630.3 fs, where negative value means negative pulse chirp. The writing wavelength was 515 nm, and the pulse frequency was 200 kHz. The dark lines indicate the etched track length. The set of processing parameters in all figures is same. The red scale bar represents 100 µm length.

M. Hermans et al. [122] performed an investigation of the etching selectivity dependence on the pulse duration, where they used as an etching agent KOH solution and high power, high repetition rate (up to 1 MHz) laser source. In our case, the etching agent was HF, and the etching optimisation for various laser parameters was done. For etching in the KOH solution, it was shown that the etching selectivity increases for longer pulse durations independently on the pulse chirp parameter. During the etching in the HF acid, the maximum etching selectivity in all cases was achieved for pulse duration in the range of ~ 600-700 fs for different pulse density (pulses/ µm) settings (see Figure 19).

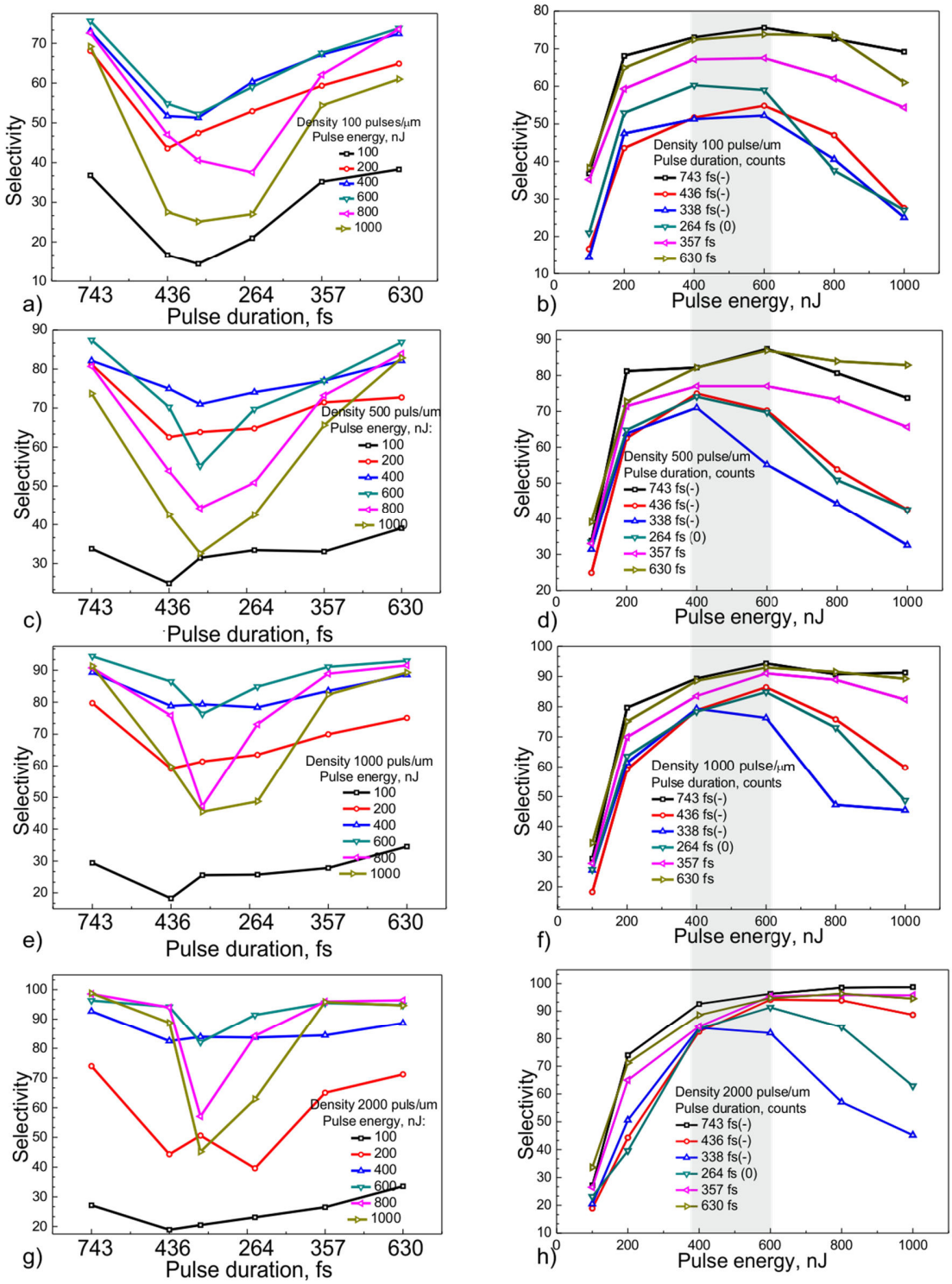

Figure 19 Etching selectivity dependence on the pulse duration for 100, 500, 1000 and 2000 pulses/μm density for different pulse energy (left column, a, c, e, g) and on the pulse energy for 100, 500, 1000 and 2000 pulses/μm density (right column) for different pulse durations at the 515 nm wavelength and 200 kHz repetition rate. The grey area indicates the optimal regimes for various pulse densities.

The analysis of the experimental data presented in Figure 19b, d, f, h shows that the peak etching selectivity can be found for the pulse energies from 400 to 600 nJ and for the 100-2000 pulses/µm pulse densities. The peak selectivity can be extended from 400 to 800 nJ for the longer pulse durations independently on the temporal chirp. The maximum etching selectivity was observed in all cases for the longest pulse duration exceeding ~ 600 – 700 fs (during the experiments we were not able to use longer pulses due the insufficient modifiction intensity) (Figure 19a, c, e, g), however, the maximum absolute value decreased when the pulse density was reduced: from ~ 98:1 at 2000 pulses/µm to ~ 76:1 at 100 pulses/µm. That behaviour can be caused due to the insufficient exposure for the nanograting formation since the quality of the nanogratings is related with the multi-pulse exposure regime. For pulse durations > 400 fs and bigger pulse densities, the etching selectivity grew slowly or stayed constant even for pulse energies up to 1000 nJ. That speculates that the nanogratings are quite stable due the proper exposures.

For the lowest pulse density value of 100 pulses/µm and pulse energies from 100 to 1000 µJ, the etching selectivity behaviour had the similar tendency. For the longest tested pulse duration of 700 fs, the etching selectivity was maximal and dropped to the minimum value at the shortest pulse duration of ~ 264 fs. The pulse chirp influence for the etching selectivity was not observed. When the pulse density increased from 100 to 2000 pulses/µm, the etching selectivity for the lower pulse energy of 100 nJ and the pulse energies of 400-600 nJ appeared almost constant for the entire pulse duration range. Only small selectivity drop up to ~10:1 was observed for the pulse energies of 400-600 nJ. For the pulse energy of 100 nJ, the etching selectivity deviated up to 5:1 for the entire pulse duration range, however, for that pulse energy, the etching selectivity was only ~ 30:1 - 40:1 and is not useful for practical fabrication of microchannels or 3D devices. The optimal processing window for the 515 nm wavelength fabrication was 400-600 nJ pulse energy and 500-2000 pulses/µm density. The processing speed can be increased by setting the

lowest possible pulse density that allows fabrication up to 1 mm/s at the 500 kHz repetition rate with the 0.55 numerical aperture microscope objective.

The immediate etching selectivity drop was initiated when the pulse energies bigger than 600 nJ were used, and the pulse duration decreased to its shortest value. This behaviour indicates, that pulse intensity dramatically increased and destroyed the ordered nanograting structure. The detailed nanograting morphology dependence on the focusing depth and pulse duration is analysed in Section 3.4.

3.3.1 *Etching selectivity investigation with the 1030 nm wavelength*

The wavelength of the laser beam influences the pulse intensity that can be reached at the constant pulse energy and also the period of the nanogratings. This can lead to the different etching selectivity results due to the amount of unmodified material between nanograting planes. The etching selectivity experiments with the same conditions were repeated using the 1030 nm wavelength. Contrary to the 515 nm wavelength, the pulse duration does not affect the pulse energy, and it allowed the simpler experimental conditions.

The matrix of microchannels was fabricated with the same pulse energy, pulse density and pulse duration parameters as for 515 nm wavelength. The 3 mm length channels were inscribed 200 µm below the sample surface and separated in the middle by the wall. The microchannels etched in 15 % HF acid for 30 min are shown in Figure 20a-f. The black lines show the etched part of the modifications. The calculated results of the etching selectivity according to the method described in Section 2.3 for the 1030 nm wavelength are shown in Figure 21.

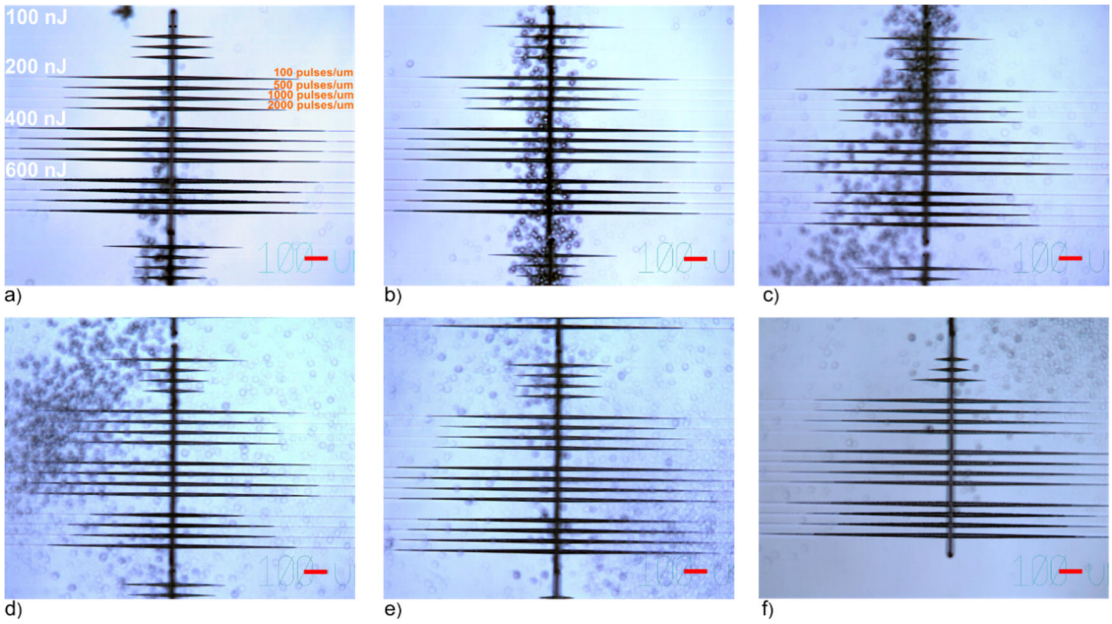

Figure 20 The microscope pictures of the microchannels etched in 15% HF acid solution for 30 min laser-written using various pulse durations: a)743.6 fs(-); b) 435.5 fs(-); c) 337.9 fs(-); d) 264.3 (0) fs; e) 356.8 fs and f) 630.3 fs, where negative value means negative pulse chirp. The writing wavelength was 1030 nm, and pulse frequency was 500 kHz. The black lines indicate the etched volume. The red scale bar represents 100 µm length.

It worth to highlight that for the lowest pulse density parameter at the lowest pulse energy of 100 nJ, and shortest pulse duration, the etching selectivity was maximal for that pulse energy and decreased to the 1:1 value when the pulse duration increased up to 700 fs. Here, the opposite behaviour than in the 515 nm case for the same pulse energy was observed. However, for higher pulse energies of 200-400 nJ, the etching selectivity was almost constant at all tested pulse durations. The contrary behaviour was for the maximal pulse energy and for the shortest pulse duration value where the etching selectivity dropped down dramatically (Figure 21a). The processing window was narrower than for the 515 nm case, and the best selectivity of ~ 140:1 was reached for the pulse energies range from 400 nJ to 600 nJ at the pulse duration of 630 fs. We speculate, that the etching selectivity for the 1030 nm was higher due the wider gaps between nanoplatelets in the nanogratings where the acid can penetrate more easily.

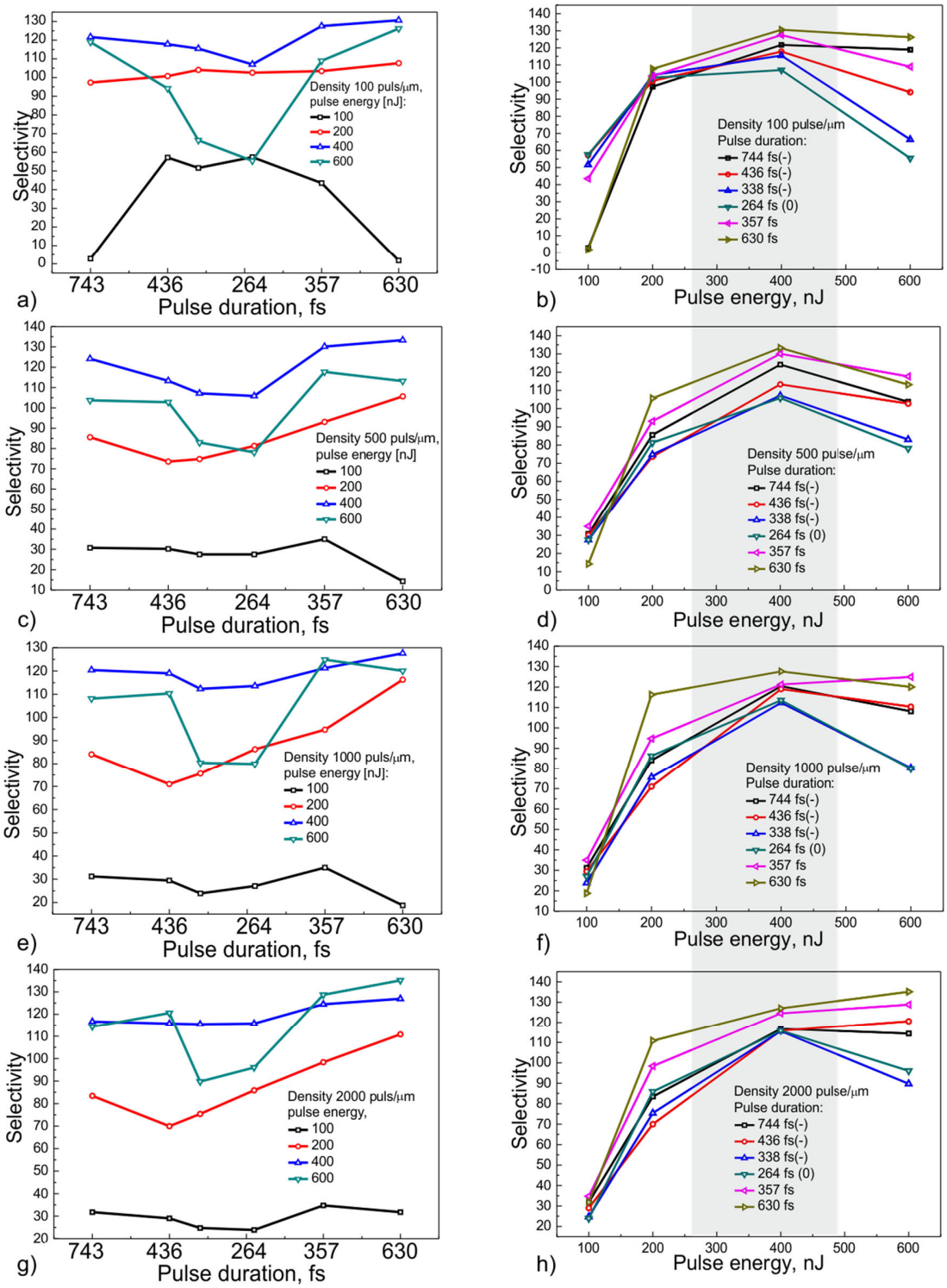

Figure 21 Etching selectivity dependence on the pulse duration for 100, 500, 1000 and 2000 pulses/μm density for different pulse energy (left column, a, c, e, g) and dependence on the pulse energy for 100, 500, 1000 and 2000 pulses/μm density (right column, b, d, f, h) for various pulse durations at 1030 nm wavelength and 500 kHz repetition rate. The grey area indicates the optimal regimes for various pulse densities.

For all used pulse densities (pulses/µm), the selectivity peak was observed for ~ 400 nJ pulse energy at ~ 630 fs pulse duration. For the larger pulse energies, the selectivity was at the same level, however, dropped down for shorter pulse durations. Therefore, when the laser system has no ability to change the pulse duration and operates at ~ 264 fs, then the optimal processing window is to use the 400 nJ pulse energy and the scanning speed up to 5 mm/s (100 pulses/µm density). Meanwhile, if the laser pulse duration can be changed or simply operated at longer pulse durations, the another processing window can be used with the higher pulse energy > 600 nJ and the pulse density starting from 2000 pulses/µm, that means that the processing speed, in this case, is only 0.25 mm/s. The lower process speed is not attractive for large structure fabrication.

The etching selectivity behaviour for the above-mentioned case of 100 pulses/µm and 100 nJ pulse energy can be explained by the threshold intensity required for the nanograting formation. For the shortest pulse duration, nanogratings are formed and, when the pulse duration increases, the laser intensity drops down and weakly ordered nanogratings are formed, and, finally, for the longest pulse duration, only the refractive index modification can be observed. For the higher energies, the optimal nanogratings are formed, however, with 600 nJ pulse energy, the ordered structure of nanogratings is destroyed due to the high pulse intensity at the shortest pulse duration. In contrary to the 515 nm wavelength, the intensity is big enough even for 100 nJ pulse energy to initiate the ordered nanograting formation and to achieve higher selectivity for the longest pulse durations.

To summarise, the etching selectivity for the 1030 nm wavelength was ~ 20% higher than for the 515 nm wavelength. The difference is the following: the selectivity for the 1030 nm wavelength for all used pulse densities was less or the same, while for the 515 nm wavelength the selectivity gradually grew when the number of pulses per one micrometre increased till 2000 pulses/µm. Interestingly, that using the 515 nm wavelength even for a large pulse energy of 1000 nJ in

combination with the long pulse duration, the selectivity drop was hard to observe, while for 1030 nm, the selectivity drop was noticeable for energies > 400 nJ. For both cases, the selectivity drop is due the worst quality and disordering of the nanogratings [72], however, for 515 nm, the period of nanogratings is twice smaller and the width of the nanograting is smaller, that could initiate lower material removing rate.

3.4 Investigation of etching selectivity with 520 nm and 1040 nm at the constant pulse duration for various pulse repetition rates

The analogous etching optimisation experiments were performed with a femtoREGEN HighQ laser (two harmonics: 1040 nm and 520 nm wavelengths). The used laser was able to run at high repetition rate up to 1 MHz when the heat accumulation effects should be taken into account [109].

The modifications with two wavelengths (1040 nm and 520 nm) were embedded 50 µm and 200 µm under the sample surface. For each depth, 3 different repetition rates were used: 200 kHz, 500 kHz, and 1 MHz. The used pulse energy was the same as in the previous experiments: 100, 200, 400, and 600 nJ for each repetition rate value. The microscope pictures of the created modifications, where two wavelengths were used are shown in Figure 22.

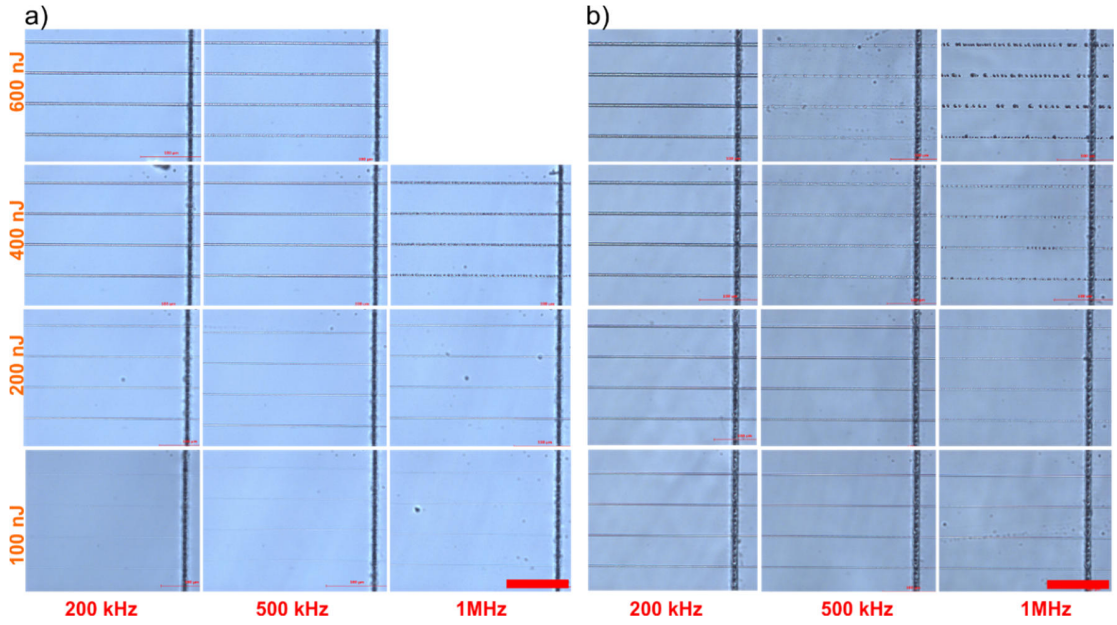

Figure 22 Modifications fabricated with different pulse energies 100, 200, 400, and 600 nJ, and different repetition rates (200 kHz, 500 kHz, 1 MHz): a) 520 nm and b) 1040 nm. The laser was operating at the 317 fs pulse duration.

The modifications fabricated with 200 kHz appeared smooth and birefringent without any anomalies for both wavelengths. When the repetition rate increased (Figure 22b), the bubble structure started to be noticeable (for > 400 nJ pulse energy), and at 1 MHz repetition rate this bubble structure appeared extremely visible. For the 520 nm wavelength, the similar modifications behaviour was observed, however, the bubble structure for maximal pulse energy had not such a strong influence. The bubbles in both cases were induced at the 1 MHz repetition rate that speculates for the appearance of the accumulation effects. To investigate the etching opportunities of the fabricated modifications, the sample was rinsed to the 20 % HF acid for 10 min, after that the microscope measurements of the etched channels were performed, and then additional 22 min. etching was done to have the total 30 min. etching time. The etched microchannels are shown in Figure 23, and the etching selectivity measurement is presented in Figure 24.

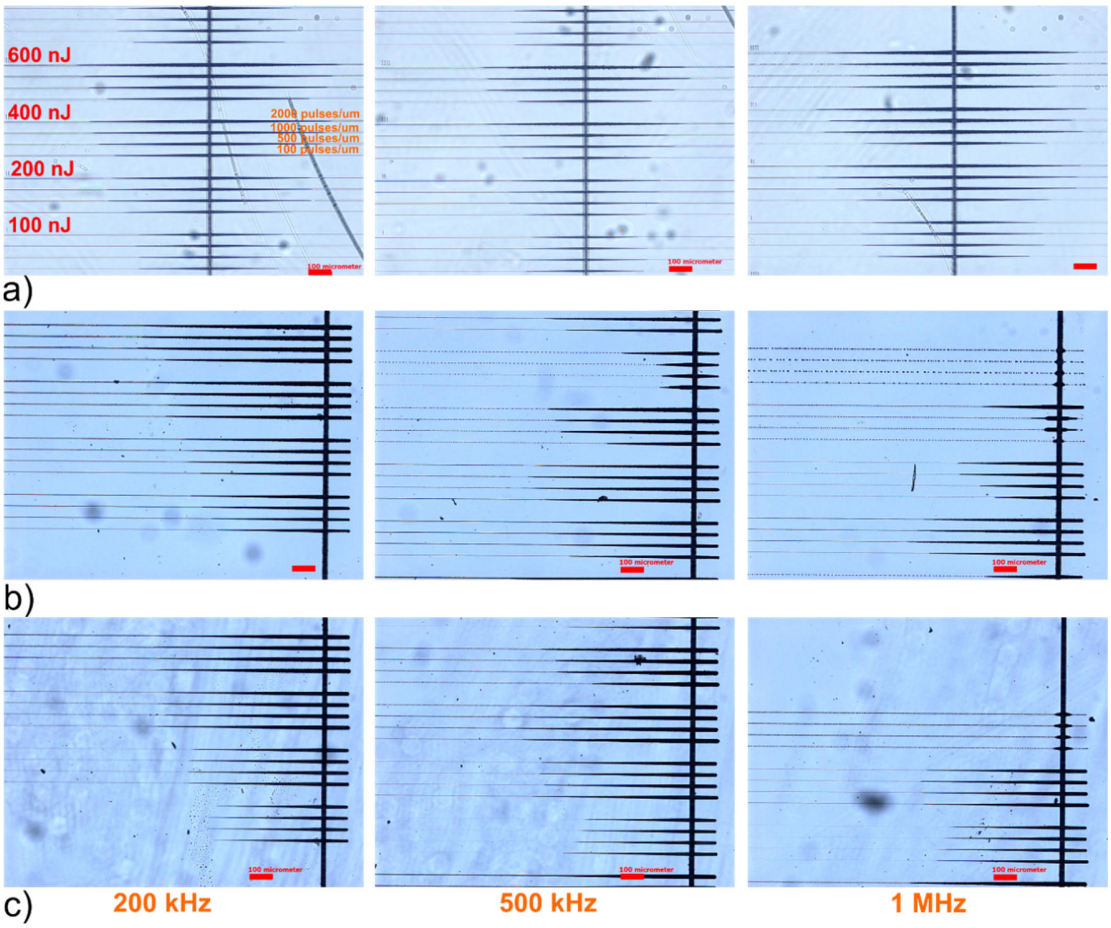

Figure 23 The etching results of microchannels fabricated with the 520 nm wavelength at the 200 µm depth (a); and 50 µm depth (b); microchannels fabricated with the 1040 nm wavelength at 50 µm depth (c). 3 different repetition rates: 200 kHz, 500 kHz and 1 MHz were used. Focusing with the NA=0.6 objective. The red scale bar shows 100 µm length.

According to the etching results, the lowest selectivity was achieved for the 1 MHz repetition rate at the 50 µm depth (Figure 24b). The selectivity results for various repetition rates and speeds are shown in Figure 24. The etching behaviour for the 200 µm depth is similar to that demonstrated for the 515 nm and 1030 nm wavelengths at the 500 kHz repetition rate. However, from this experiment, we can conclude that the 200 kHz repetition rate shows the best performance in 50 µm depth and in 200 µm depth 1 MHz should be used. Nevertheless, the absolute selectivity value of ~120:1 was not exceeded. As could be expected, the optimal pulse energies were in the range of 200-400 nJ for both wavelengths at 200 kHz

and, occasionally, at the 500 kHz repetition rates. The most attractive situation shows the 1 MHz repetition rate where different selectivity behaviour was observed. When the pulse energy grew, the selectivity dramatically dropped from 100:1 at the 100 nJ pulse energy to 1:1 at the 600 nJ pulse energy. This phenomenon was more noticeable for the 520 nm wavelength, probably due to the higher pulse intensity. The explanation can be found in the accumulation effects that are more expressed at the high repetition rate. More heat was induced that caused unpredictable behaviour of the nanogratings, and, most likely, the disordering threshold was reduced to ~ 200 nJ pulse energy.

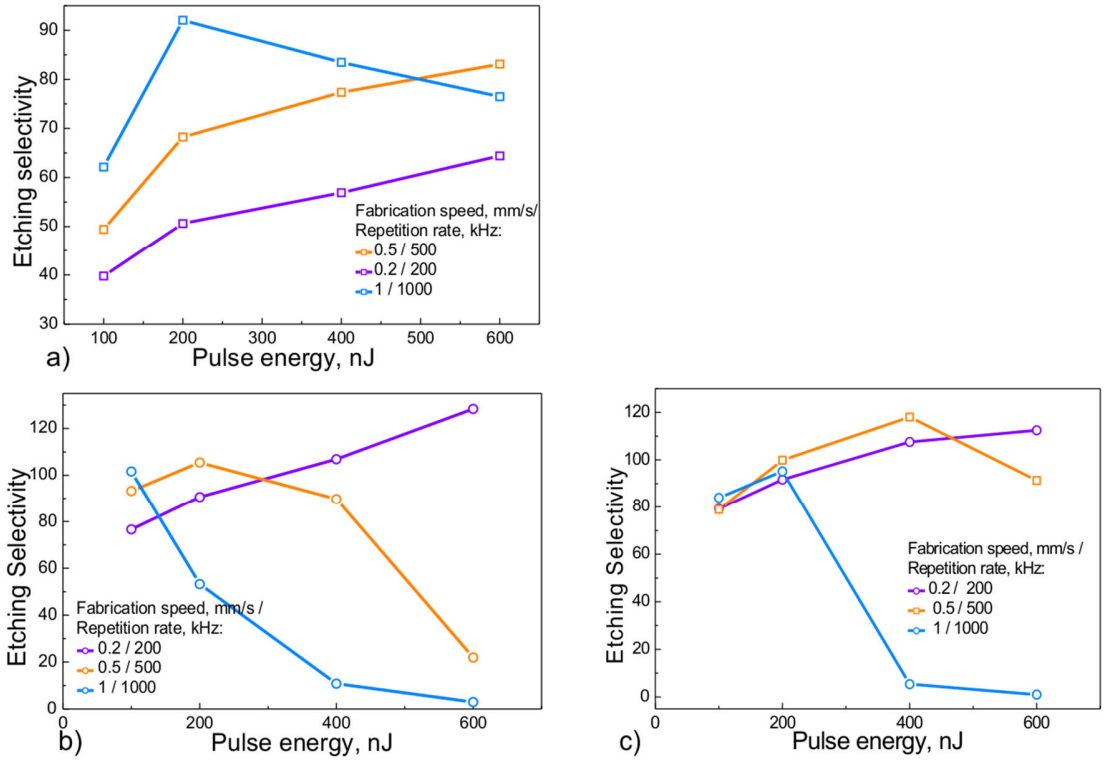

Figure 24 Etching selectivity dependence for the different wavelength and focusing depth: a) 520 nm wavelength and 200 µm focusing depth; b) 520 nm wavelength and 50 µm focusing depth; c) 1040 nm wavelength and 50 µm focusing depth. The pulse density is 100, 500, 1000 and 2000 pulses/um for different pulse energy (100, 200, 400 and 600 nJ). The pulse duration is ~ 317 fs. Etching selectivity for the unmodified material is ~ 13.09 µm/h at 35 °C.

3.5 Investigation of etching selectivity for microchannels fabricated with 0.25 NA objective and different pulse duration

The longer modifications in the vertical direction are achieved using an objective with the numerical aperture of NA= 0.25. The microchannels were inscribed 200 µm below the sample surface with two different laser wavelengths 515 nm and 1030 nm, and with 6 different pulse durations (Section 2.5). The few etched microchannels in 15 % HF for 30 min. are shown in Figure 25.

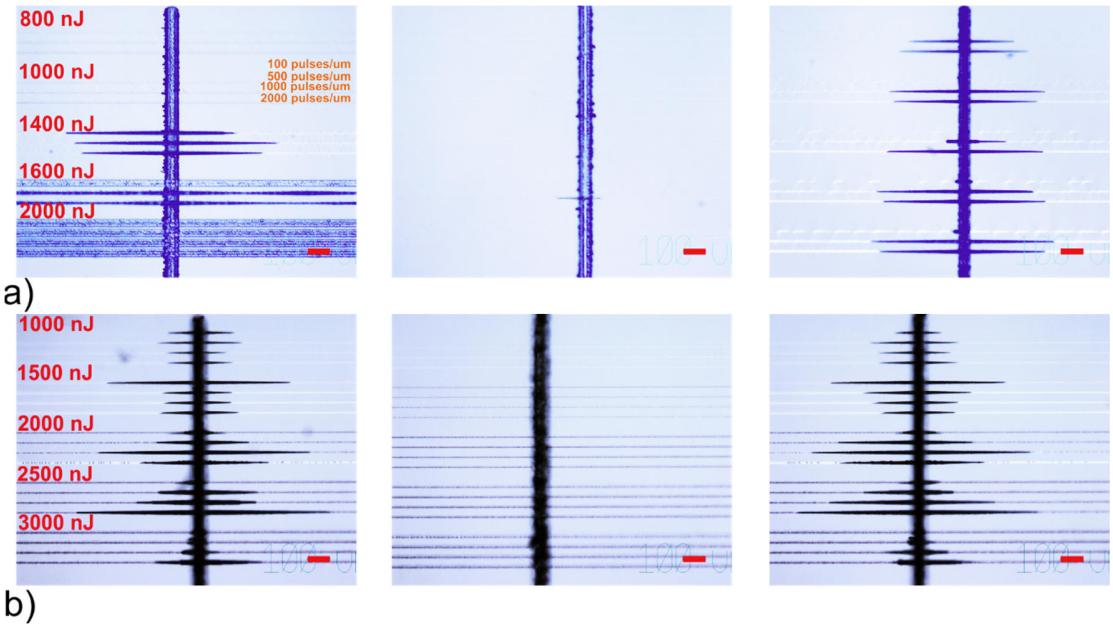

Figure 25. The microchannels fabricated with 0.25 NA microscope objective with two different laser wavelengths (Pharos): a) 515 nm and b) 1030 nm with 743.6 fs(-), 264.3 fs (0) and 630.3 fs from left to right. The red scale bar shows 100 µm length.

The calculated spot size (1.22λ/NA) for 0.25 NA was ~ 2.5 µm for 515 nm and ~5 µm for 1030 nm. The similar pulse energy density as for fabrication with the NA=0.55 objective required the pulse energies in 1000-1600 nJ range for 515 nm and 1000 -3000 nJ pulse energies for the 1030 nm wavelength. Calculated etching selectivity for two wavelengths is shown in Figure 26. The etching selectivity was maximal for the longest pulse duration for both positively and negatively chirped pulses. Therefore, for the shortest pulse duration and the 30 min etching time, almost no channels etching for both wavelengths was observed. Even for the low

numerical apertures, the longer pulse duration allows the better etching selectivity. This speculates that pulse duration plays a crucial role in the nanograting formation and selective etching. According to the optical microscope pictures, the best etching was observed for the channels that appeared brightest in a microscope with crossed polarisers. For 515 nm wavelength, the selective etching was reached only for two different pulse energies of 1400 nJ and 1600 nJ and for 2000 pulses/mm pulse density. For bigger pulse energy, the etching selectivity appeared higher, however, at the maximal pulse duration, the selectivity for both energies approached to the same value. For 1030 nm, the selectivity was larger by 10% comparing with 515 nm.

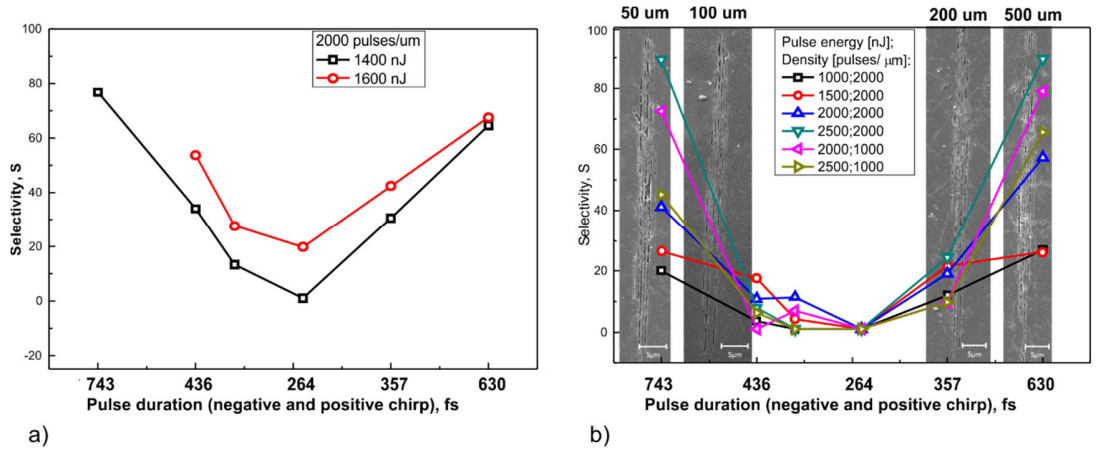

Figure 26 The etching selectivity of the microchannels fabricated with the 0.25 NA focusing objective for a) 515 nm and b) 1030 nm at 6 different pulse durations. The SEM pictures show the cross sections of the microchannels at different depths recorded with the 1000 nJ pulse energy and 264 fs pulse duration.

For the 1030 nm wavelength the three different pulse energies and pulse densities of 1000-2000 pulses/mm showed good etching results. The pulse energy was up to 3000 nJ in this case. Comparing the maximal etching selectivity for 0.25 NA and 0.55 NA objectives, it can be found that in both cases, the optimal pulse intensity for 515 nm was 19.5-39 J/cm^2 which corresponds to the 200-400 nJ pulse energy in the case of the 0.55 NA objective. For the 1030 nm wavelength, the optimal etching selectivity was at the 9.8-14.6 J/cm^2 fluence which corresponds to the 400-600 nJ

pulse energy in the case of the 0.55 NA objective. It can be noted that for the 1030 nm wavelength, only slightly bigger pulse energy should be used. However, the pulse density was ~ 2.5 times lower. This demonstrates that lower fluence is required to form the adequate nanograting quality using the 1030 nm wavelength.

3.6 Etching rate comparison with and without ultrasonic bath

Usually, the etching is the time-consuming process that should be shortened as much as possible to make this technique more attractive. Due to this reason, a few experiments were performed to investigate the differences between the microchannels etched in an ultrasonic bath and without an ultrasonic bath. Two identical samples were fabricated using the 515 nm wavelength at two different repetition rates of 200 kHz and 500 kHz for that. The processing parameters were similar to that described in Section 3.3.1 (4 different fabrication depths, pulses densities of 100, 500, 1000 and 2000 pulses/mm and pulse energies of 100, 200, 400 and 600 nJ). One sample was immersed to the jar with the 15 % solution of HF at ambient temperature, and another sample was immersed to the same jar and placed into the ultrasonic bath (Bandelin, Sonorex Super). The etching took 30 min. After that, the samples were removed from the HF solution and washed in deionized water. The microscope pictures of the etched channels are presented in Figure 27.

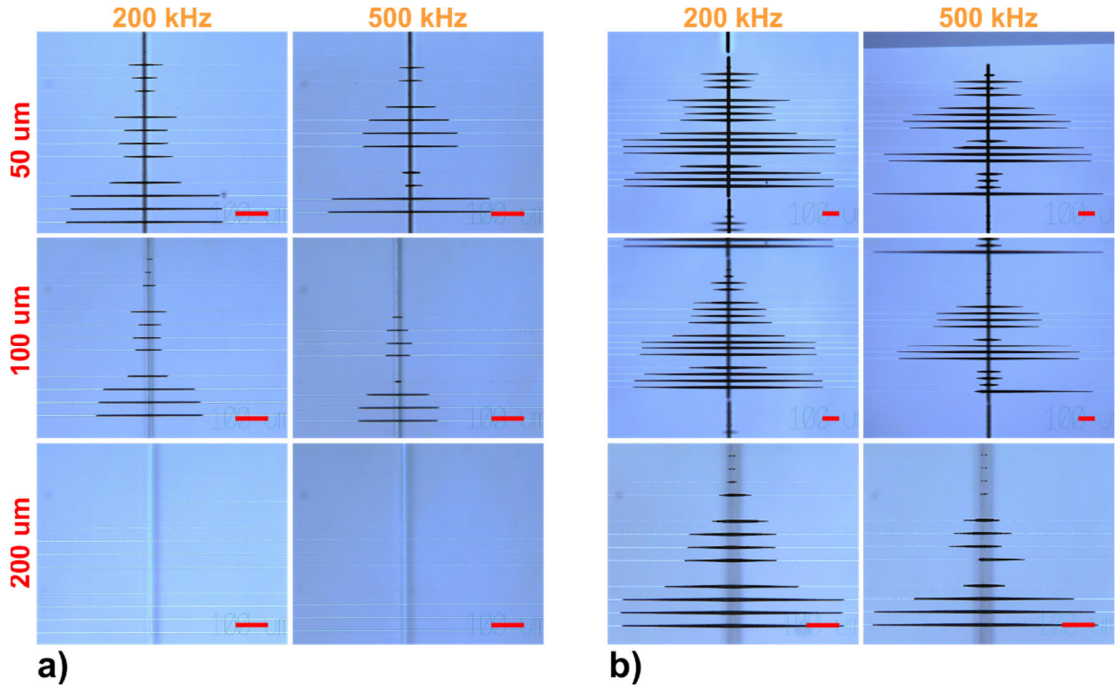

Figure 27 Comparison of the selective etching of microchannels fabricated with for 515 nm for two different repetition rates of 200 kHz and 500 kHz: a) without ultrasonic bath; b) with ultrasonic bath. The red scale bar shows 100 µm length.

There is a significant difference that confirms that ultrasonic bath increased the etched microchannel length. For the 200 µm depth, no etching during 30 min. was observed for the samples etched without an ultrasonic bath. Using the ultrasonic bath to vibrate the sample, the microchannels at the 200 µm depth started to be etched. The measured results of the etching selectivity of both cases are depicted in Figure 28. It can be seen that the microchannels fabricated with the 500 kHz repetition rate are etched with a poorer quality which is confirmed by the brightest channels seen in a microscope for 200 kHz repetition rate (Figure 27). The etching rate of non-modified fused silica was estimated for the etching without an ultrasonic bath to be equal to ~3.5 ± 0.45 µm/h, and with it ~11.6 ± 0.6 µm/h. It is interesting that due the different etching rates for non-modified fused silica in two cases the calculated etching selectivity shows similar results for two samples. This means that by using ultrasonic bath ~ 3.3 times longer channels can be achieved during the

same etching time, however, the spatial resolution is lost due to the higher etching rate of the unmodified material.

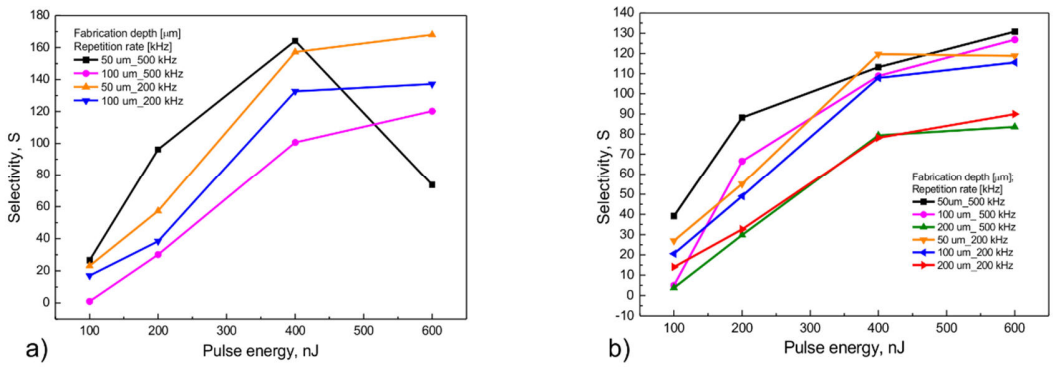

Figure 28 Etching selectivity of fused silica in ambient temperature in 15% HF acid for 30 min: a) without ultrasonic bath and b) with ultrasonic bath. The pulse density for both cases is 2000 pulses/μm. The etching time for different depth was scaled accordingly taking into account the etching time of the walls.

For higher temperatures, the etching rate of unmodified fused silica increases and the etching selectivity remains at the same level due to increased etching rate of the unmodified fused silica as well. The etching saturation is inevitable that speculates that for the HF etchant, it is not possible to achieve higher etching selectivity that ~ 160:1. When the length of the etched channels increases, the selectivity drops to 1:1 and the maximum channel length of ~ 2 mm can be achieved. The calculated etching of the unmodified fused silica is even higher ~ 40 μm/h for the HF temperature of ~ 70 degrees.

3.7 Focusing depth influence to the nanograting morphology and etching selectivity

Depending on the focusing depth and the used wavelength, the different morphology of the nanogratings can be achieved. For conventionally used focusing objectives of 0.2-0.6 NA, aberrations play a significant role in getting the required intensity field distribution needed for the nanograting formation. In this study, the influence of different focusing depth for nanograting formation is demonstrated. The longitudinal internal modifications formed along the horizontal plane were

fabricated with objectives of two different numerical apertures (NA = 0.25 and NA= 0.55). For the first step to evaluate the etching selectivity of the microchannels, a sample with longitudinal modifications using the 515 nm and 1030 nm laser wavelengths was etched in 15% HF acid for 30 min. Later, the sample was side-polished to have the direct access to the vertical modification plane and etched for 1 min in 5% HF acid to reveal the nanogratings (Figure 29 a, b). For a better understanding of the phenomena involved and to take polarization of the focused beam at tight focusing into account, the Debye vectorial focusing [123] calculations was used to model the intensity field distribution at different focusing depths and compare them with the experimental data. The modelling results are presented in the Figure 29 c-e where the revealed nanogratings are associated with the modelled intensity distribution. The 1D intensity cross-section shows that the maximal intensity is achieved for the 50 µm depth, and for a deeper focusing, the intensity drops down due to the aberrations.

It should be noted that the well-structured nanogratings were achieved for a deeper focusing where the intensity was lower than for focusing near the surface (Figure 29 e). The structural modifications with the two side wings (Figure 29 f) are observed with the good agreements with the theoretical modelling results.

The measured results link the length of the etched microchannels (Figure 30) with the quality and morphology of the nanogratings formed at various depths extracted from the scanning electron microscope images. This association helps us to understand how critical is the quality of the nanogratings for the etching selectivity of the microchannels.

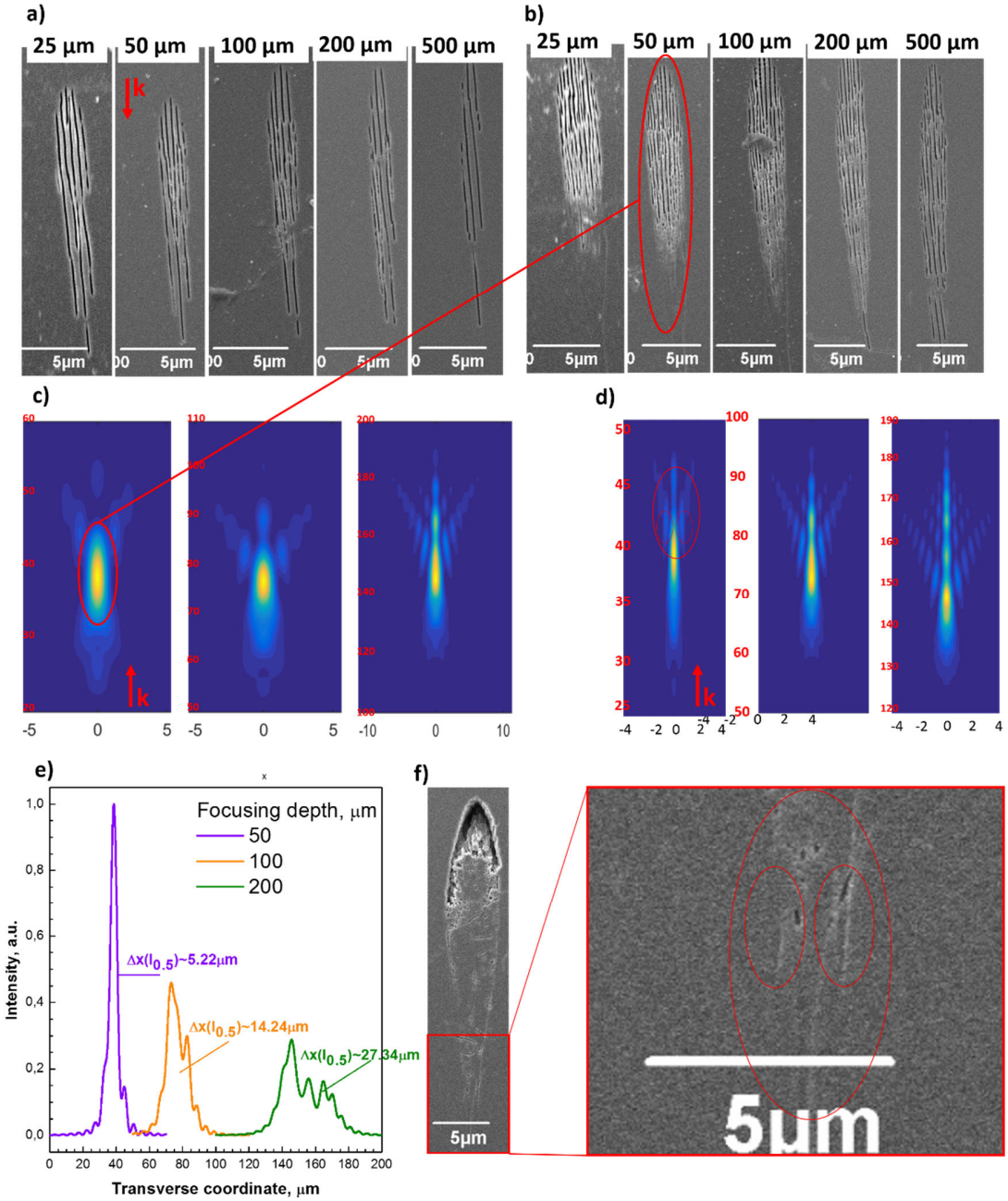

Figure 29 SEM images of the polished and etched for 5 min in 1% HF solution microchannels in yz plane recorded with 1030 nm at different depths in fused silica: (a) pulse energy 200 nJ, scan speed 0.25 mm/s; (b) 400 nJ, and 0.25 mm/s. Theoretical modelling results of the focused femtosecond laser beam in bulk fused silica using: (c) 1030 nm and (d) 515 nm wavelengths. The focusing depths were 50 µm, 100 µm and 200 µm; (e) The modelled intensity profiles along the focusing depth in the 1D case; (f) SEM image of the modified cross-section recorded with the 600 nJ pulse energy at 50 µm depth formed with 515 nm wavelength. The wavevector indicated the beam propagation direction.

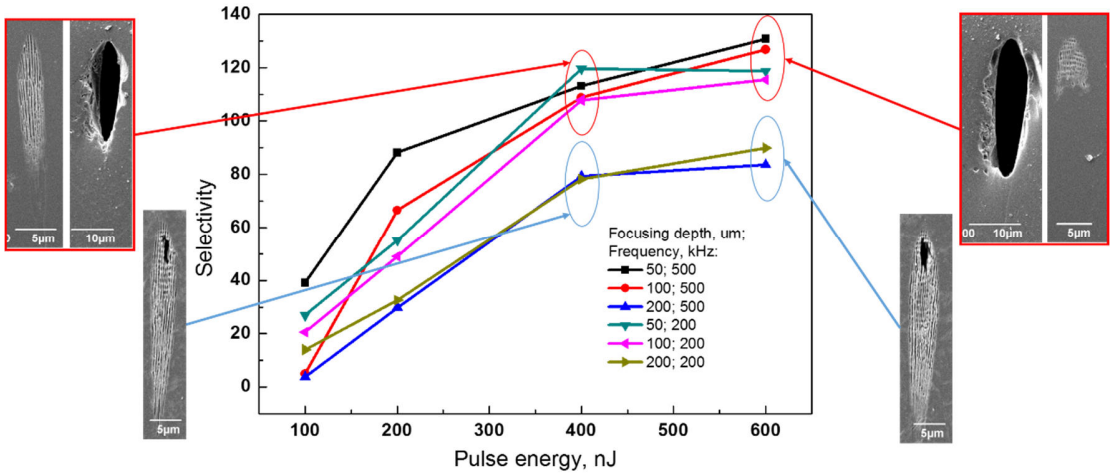

Figure 30 a) Dependence of the etching selectivity on the recording depth of a channel using the 1030 nm wavelength. The channel writing parameters were the 260 fs pulse duration and 2000 impulses/μm density. The insets show the transversal profiles of the channels before and after etching for a specified depth

Depending on the focusing depth, the different etching selectivity was measured. For pulse energies of 100-200 nJ, the etching selectivity was maximal for the 50 μm focusing depth, while for the 200 μm depth the selectivity was almost 1:1. This suggests that for that depth, the intensity is too low to initiate the nanograting formation. For pulse energies from 400 to 600 nJ, the etching selectivity for the 50 and 100 μm focusing depths was in the similar range. This case can be explained by the process window where the intensities are in the range satisfying the well-structured nanogratings. According to the SEM pictures, it can be noted that the etching started from the top part of the modification where the intensity level was lower. The nanograting period dependence on the pulse energy for different focusing depth was found after detailed investigation (Figure 31).

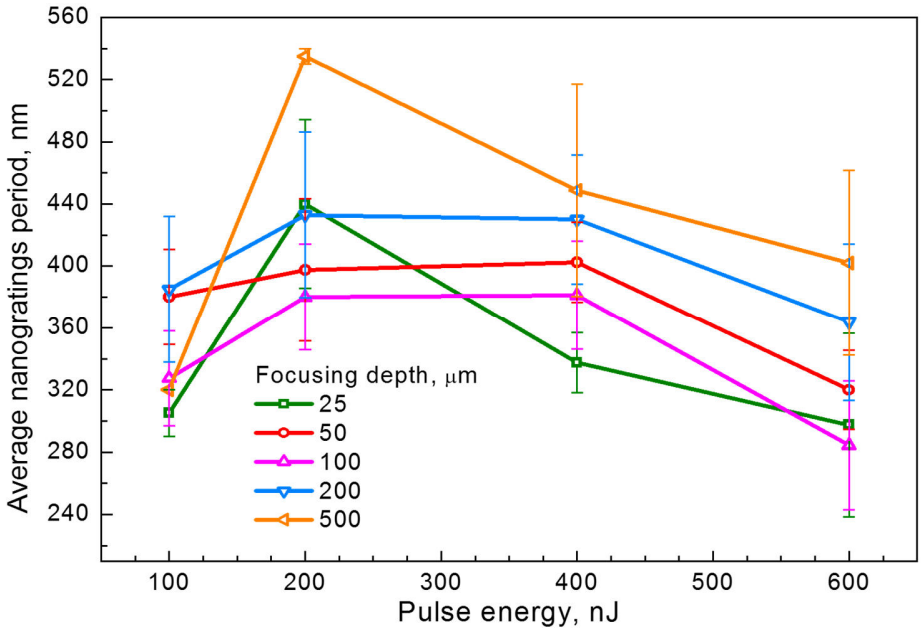

Figure 31 Dependence of the average nanograting period on the focusing depth and pulse energy for 1030 nm wavelength and ~ 264 fs pulse duration.

The discovered dependence shows that the nanograting period is related to the focusing depth. For deeper focused modifications, the period was maximal, and for the 500 μm focusing depth, it was equal to ~ λ/2. However, when the focusing was near the surface, the period dropped and was equal to ~ λ/2n. From 100 to 200 nJ pulse energy, the period grew, and it was maximal for the 200 nJ energy for all focusing depths. The further pulse energy growth initiated the period drop. For 100 nJ pulse energy, the nanogratings started to be formed and, had not well arranged period. For the 200 nJ pulse energy, we had the optimal conditions and for bigger pulse energies the period started to densify the lower nanograting quality consequently was achieved.

3.8 Rectangular channels formation

For many applications [118], the microchannels with wider and rectangular cross section are required. In this section, the writing procedure of the microchannels with a rectangular shape with the 515 nm wavelength and repetition rate ranging from 100 to 500 kHz is described.

The principle of rectangular channels formation is shown in Figure 32a, where multiple lines are inscribed close to each other ~ 250 µm under the sample surface. The rectangular microchannels were recorded with 4 different pulse energies: 200, 660, 1300, and 1700 nJ (appropriate fluencies are 5.8, 19.1, 37.5, and 49 J/cm^2) at the repetition rate of 100 kHz. Each of that channels was repeated four times by varying writing speed (0.05, 0.2, 0.5, and 1 mm/s). The multiple-line scanning in the y direction with a spacing between the lines in x (1 µm) and z (15 µm) direction was utilised. In such a way, the channels with a square cross section were formed by 8 x 3 scanning lines in x and z directions before the etching. The recorded microchannels array is shown in Figure 32b which depicts the microscope picture with the crossed polarizers. The brightest channels indicated the largest birefringence caused by the existence of the nanogratings [81].

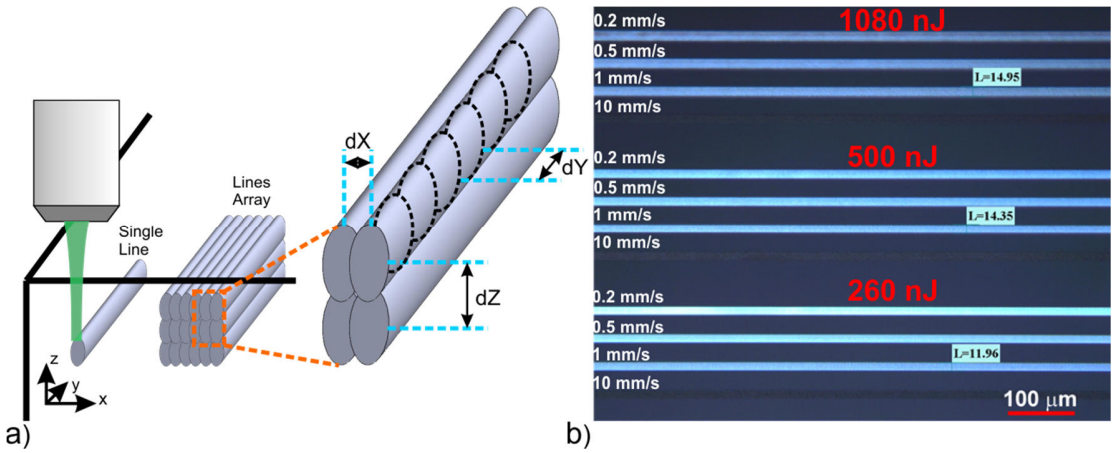

Figure 32 Rectangular channels formation principle by stacking modifications in x y and z directions (a); Microscope picture of formed rectangular modifications with different processing parameters (8 x 3 line array) (b). dx, dy and dz indicates the distance between the pulses in x, y and z directions.

The irradiated samples were immersed into an aqueous dilution of HF acid of 10 % of concentration and etched 6 hours at the room temperature. After the etching procedure, the samples were rinsed into 2-propanol for 5 min. The etching results are represented in Figure 33.

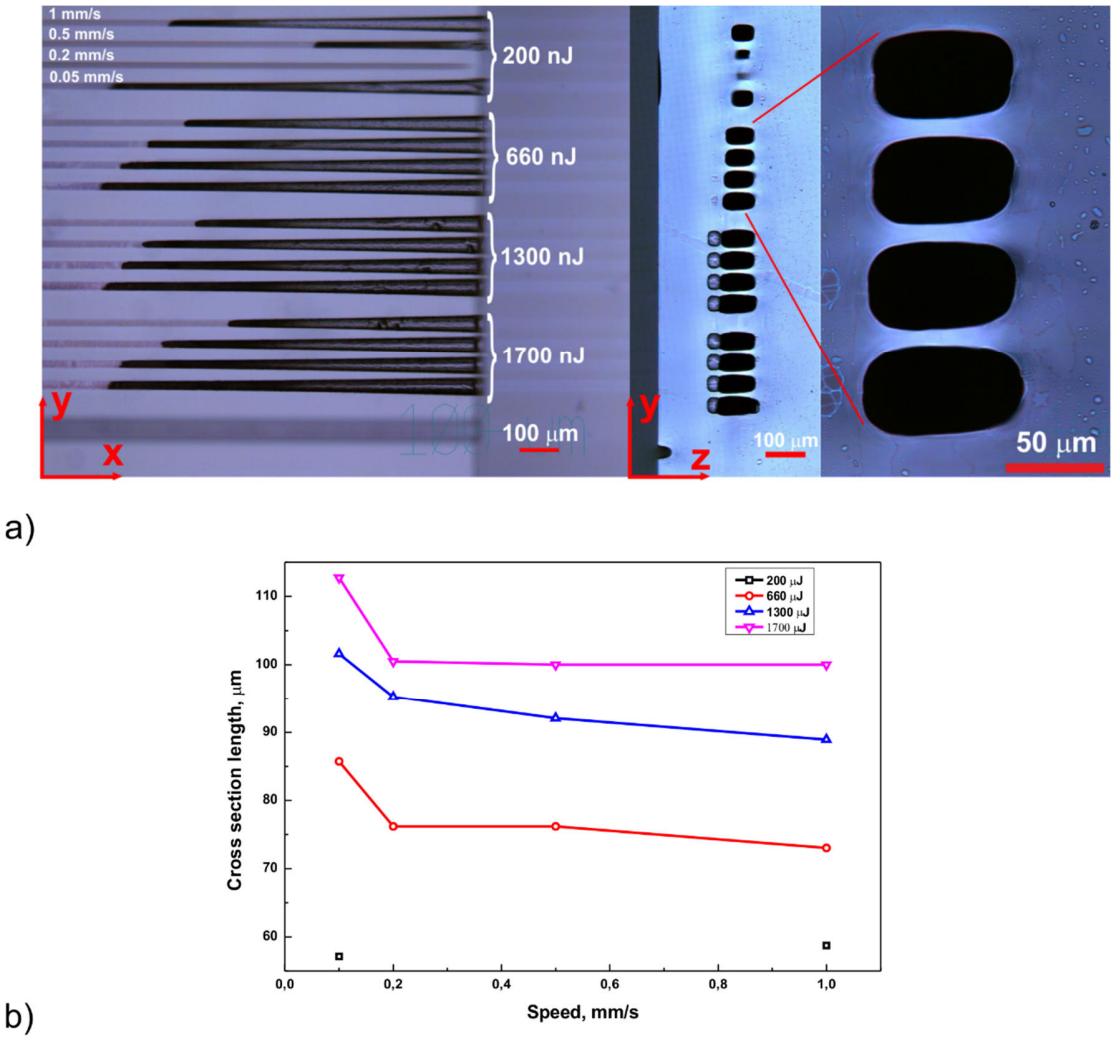

Figure 33 Transmission-light optical microscope pictures of micro-channels etched in 10 % HF acid for 6 h (8 × 3line array) inscribed with polarization perpendicular to the writing direction and repetition rate of 100 kHz: (a) xy-view (right) and zy-view (left) (laser pulse energy:200, 660, 1300, and 1700 nJ from top to bottom between groups; writing speed: 1, 0.5, 0.2, and 0.05 mm/s from top to bottom in each group) and (b) microchannel cross section length dependence on the scanning speed with different laser pulse energies.

3.9 Conclusions

The wide range of process parameters such as the laser wavelengths, repetition rate, pulse duration, focusing depth with two different laser systems and few different focusing objectives was applied to find the optimal etching parameters of fused silica in diluted HF acid. It was found that the critical influence to the etching selectivity plays the pulse energy that should be set in the range of 200-400 nJ for

the 0.55 NA objective and the range of 1400-2500 nJ for the 0.25 NA objective, and the pulse duration, that for all cases exceeded the ~700 fs value. The etching time can be improved more than 3 times by maintaining the same etching selectivity by using an ultrasonic bath. To improve even more the etching time, the etchant temperature needs to be increased up to 70 degrees. However, the spatial resolution is lost in this case.

The method of inscribing micro-channels in fused silica using the line-array writing is presented. This method can be applied for formation of channels with the rectangular cross-section of different size. The size of rectangular cross-section is controlled by adjusting laser pulse energy and dimension of the lines array. By increasing laser pulse energy, the longitudinal modification of voxel increases faster than the transversal modification, and the height-to-width ratio of rectangular channel increases. The processing speed used in this work just slightly influences the channel cross-section dimensions. The negligible changes of the channel cross-section appear due to the laser pulse energy.

The experiments demonstrated that the processing speed could be increased when the laser with a higher repetition rate is used. The processing speed up to 1 mm/s was achieved with the 500 kHz repetition rate laser.

These experiments are an introduction to the formation of more complicated 3D structures in fused silica substrates for fluidic applications.

4 Orientation of sub-surface nanogratings

The results presented in this section were published in articles [P4].

Understanding of material behaviour at nanoscale under intense laser excitation is underpinning future laser processing technologies. Mechanical, optical, structural and compositional properties of materials can be tailored for novel alloy formation, catalytic and sensor applications. Light polarization is an effective parameter to control the energy delivery in laser structuring of surfaces and volumes [124–128]. The orientation of self-organized deposition of materials [129], melting and oxidation of thin films by dewetting [130], laser ablation [131, 132], and self-organized ripple nano-patterns induced on the surface [51, 133] are some examples of polarization related phenomena that gained interest recently.

The creation of surface ripples in metals or dielectric materials under the laser irradiation is a well-known method to nanotexture a surface, where the ripple orientation can be finely controlled with the polarization direction [51] and extended over two dimensions field [134, 135]. In dielectrics, nanostructuring is also possible below the surface, in the bulk of the material, by using femtosecond lasers. In particular, laser irradiation can create self-organized nanogratings in the volume of a fused silica substrate with a period in the order of a fraction of the laser wavelength [14]. Besides the fundamental interest in these nanogratings, which are the smallest structures that can be created by the light inside of a transparent material, a few applications stemmed from these structures. In fact, it was understood that they are the basis of the microchannel formation when using the FLICE technique [81], which paved the way for the development of several optofluidic devices for biophotonic applications [79]. Another important application of nanograting formation in fused silica is the direct writing of spin-orbital polarization converters [136], e.g. for fabrication of q-plates [137]. In addition, nanograting can be exploited to write permanent optical memories with a very high capacity [138]. In many of these devices, an ultrafine control of the laser-

induced nanogratings is crucial. As an example, it was found that optical function of q-plates in silica is affected by nonhomogeneous fluorescence across the optical element due to a complex spatial pattern of the light absorbing defects [139]. This anisotropy is presumably due to a heat conduction alteration during fabrication, which affects the laser writing itself and, in the end, the performance of the optical element. Therefore, vectorial nature of the light-matter interaction has to be better understood in the case of nanograting formation [140].

Here, a systematic study of the nanograting width, period and orientation as a function of several irradiation parameters and most notably of the writing scan direction was carried out in fused silica, which is an isotropic matrix regarding absorption and heat diffusion. Fourier analysis of scanning electron microscope images revealed unexpected features of the nanograting that were never reported before. While it was widely considered that nanogratings are occurring perfectly perpendicular to the incident laser polarization [15, 55], however, we demonstrate that the significant tilt is observed depending on the scanning direction relative to the laser polarization. Repeated experiments on various femtosecond laser fabrication setups and various focusing conditions were implemented, and consistently confirmed the period variations and tilting of the nanogratings for different writing directions at industrial laser printing conditions. A vectorial light-matter interaction model is put forward to explain all the observed features and to improve our understanding and control of nanograting formation.

4.1 Estimation of the nanograting tilt angle

In order to determine the angle Ψ between the orientation of nanogratings and polarization for different scanning directions, the following procedure was carried out (see Figure 34). The orientation angle Ψ_p of the wave vector $K=2\pi/\Lambda$ of the nanogratings was determined for each scan direction with respect to the SEM image X-axis. There were 24 scan directions, φ, in a star pattern with $\Delta\varphi=15°$ separation

between the neighbouring rays (Figure. 34c). A fixed polarization, $\boldsymbol{E_y}$ orientated along Y-axis, i.e. it is always perpendicular to the X-axis translation was used to write all the lines, i.e. a polarization parallel to the ***K***-wave vector at φ =0°. The tilt angle of the nanograting wave vector with respect to the polarization direction was calculated as $\Psi_p(0°) - \Psi_p(\varphi)$ for the various scanning directions in order to compensate the possible misalignments between the image X-axis and the φ =90° orientation when placing the sample in the SEM. By this definition, the positive tilt +Ψ corresponded to a clockwise (cw) rotation of the nanograting orientation. This is a determination of the tilt angles in respect to the initial scan angle φ=0°. To further reduce errors in positioning and judgement of nanograting orientation, the Fast Fourier Transform (FFT) of the images were calculated in random and sequential order with respect to the φ angles. In addition, a test of two different people carrying out the analysis using the same SEM images with the Gwyddion and ImageJ freeware packages was used as a reference test.

In Section 4.3.2., the nanogratings orientation angle dependence on the half-wave plate rotation angle ϕ was determined, and the relevant nanograting orientation angle is defined as $\Psi'(\phi) = \Psi'(\phi=0°) - \Psi'(\phi;)$ at E_p=const. Here the nanogratings rotates because the laser polarization direction is changed and therefore this is the classical nanogratings rotation but not the nanogratings tilt.

The tilt angle for different pulse durations in Section 4.3.4 was determined relative to the smallest pulse energy and the shortest pulse duration $\Psi = \Psi(\tau=264\ fs;\ E_p=50\ nJ) - \Psi(\tau;\ E_p=const), \text{ at } \phi=const$.

In this document, the term “nanogratings tilt” is used to describe the nanogratings angle deviation from the direction perpendicular to the polarization orientation and is related to the scan direction, pulse front tilt or pulse energy. However, this term is not related to the polarization direction.

4.2 Subsurface nanogratings induced with 1040 nm wavelength

The fabrication method of the subsurface nanogratings is described in Section 2.5. In the case of linear polarization, the orientation of the nanogratings is usually predefined by the polarization orientation, $\boldsymbol{E_y}$. However, the corresponding wave vector $\boldsymbol{K}$ defining the period and orientation of the nanogratings was found to be affected by the scan orientation and was systematically studied here. The wave vector $\boldsymbol{K}$ is defined as $K = 2\pi/\Lambda$, where Λ is the nanograting period, and the $\boldsymbol{K}$ direction is orthogonal to the nanograting orientation (Figure 34a). The angle Ψ_p is defined as the angle between the horizontal reference axis and the nanograting wave vector (Figure 34b). The tilt angle of the nanograting orientation $\Psi(\varphi)$ is determined precisely for various scan directions as explained in Figure 34c.

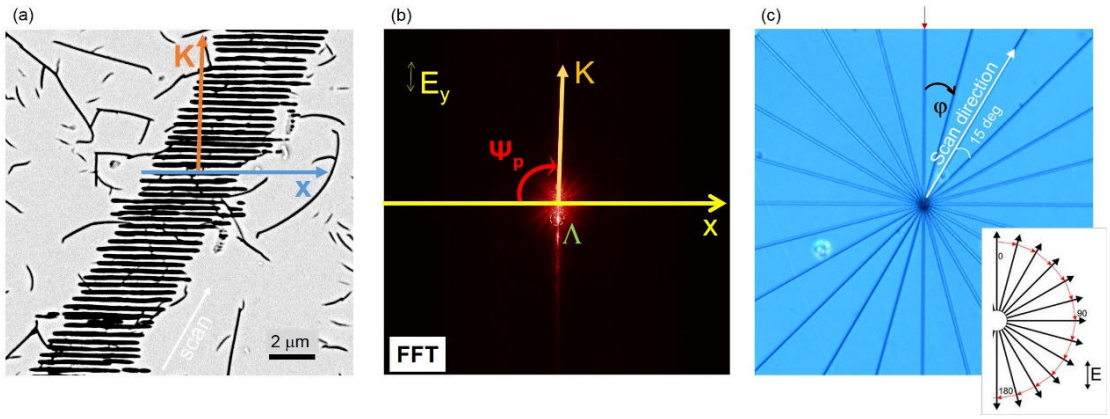

Figure 34 Determination of the nanograting tilt angle Ψ for different scanning directions. (a) SEM image of sub-surface nanogratings in fused silica recorded at 10 µm depth and polished afterwards for observation. (b) Fast Fourier transform (FFT) image of the SEM image shown in (a); polarization $\boldsymbol{E_y}$ is fixed in all experiments. (c) Optical image of the *star* pattern with the $\Delta\varphi = 15°$ angle between subsequent rays. The red arrow shows $\varphi = 0°$ position; inset shows fabrication orientation with all lines drawn from the centre outwards.

A few representative examples of SEM images of the polished and wet-etched samples are shown in Figure 35 shows. The spot size at the focus (represented by the yellow circle in the figure) had a diameter $d = 1.22\lambda/NA \cong 2.1$ µm with $NA = 0.6$. Measurements were carried out for all 24 scan orientations (only 6 are

shown here). Polarization was fixed as $\boldsymbol{E}_y$. Immersion into aqueous hydrofluoric acid solution was used to reveal the nanogratings better, but also enhanced the visibility of random scratches in the laser non-exposed surrounding areas due to non-optimal polishing process.

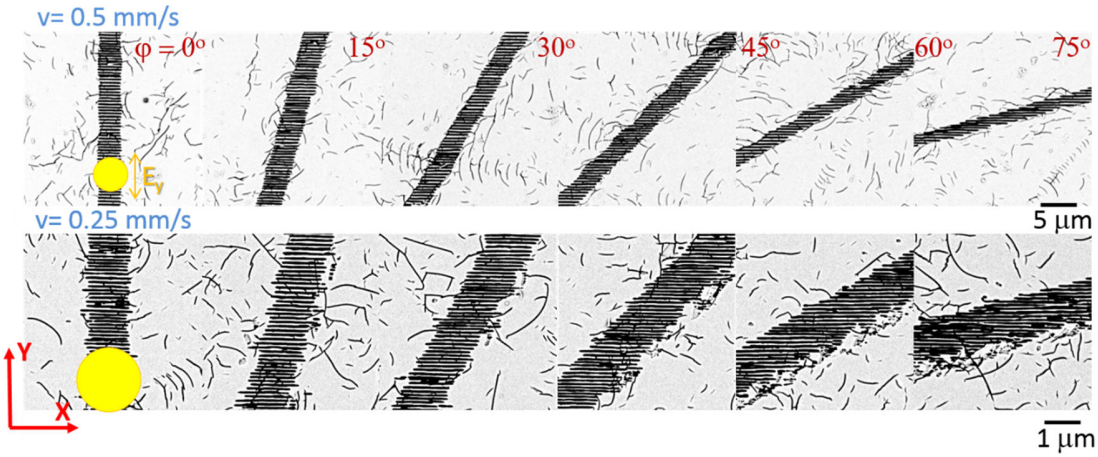

Figure 35 SEM images of nanogratings recorded at different scan directions φ. Processing parameters were λ=1040nm, τ_p=317fs pulses (HighQ Laser) of E_p=600nJ energy (measured on target after the objective lens) at the repetition rate of 500 kHz. Results for two different scanning speeds v are presented in the two rows of images. The yellow circle in the figure represents the spot size in the focus with a diameter ~ 2.1 µm.

Figure 36 shows that a tilt between the nanograting orientation (wave vector) and the polarization for different scan directions can be as high as $\Psi \sim 2°$ (measured according to the method described in Section 4.1, and the tilt angle was maximal when directions of the scan and the polarization had an angle of ~π/4. This tendency was observed for various scanning speeds, pulse energies, and numerical apertures at a moderate focusing.

The SEM image analysis (Figure 34) also revealed that there was an evident difference in the width of the nanograting region depending on the scanning direction. Interestingly, FFT data showed that also the nanograting period had a remarkable angular dependence. Results of the analysis are presented in Figure 37.

A continuous change of the width of the nanostructured line, *w*, between φ=0 and π/2 was observed, with a maximum at φ=0. This tendency was present for different pulse energies, pulse durations (for up to twice longer pulses), focusing conditions and scanning speeds; not all results are shown for brevity. A linear dependence was observed for the modification width, *w*, on the pulse energy (Figure 37b).

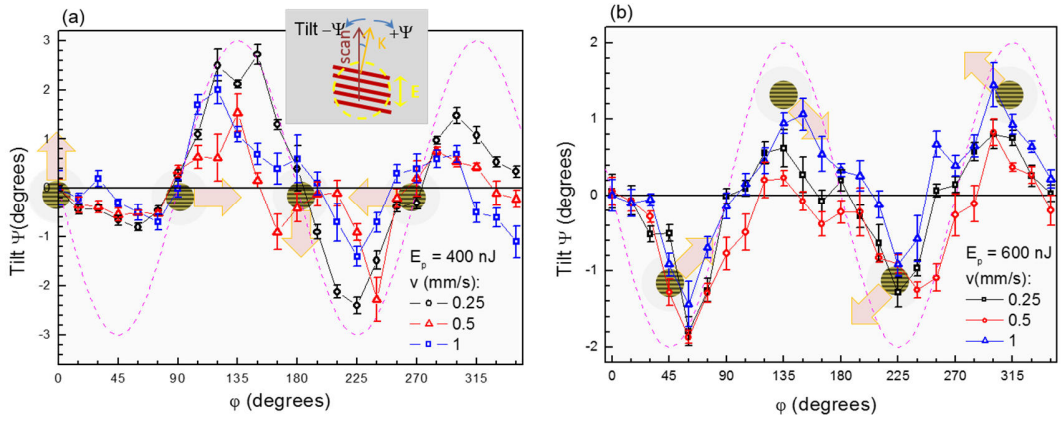

Figure 36 Tilt angle orientational distribution $\Psi(\varphi)$ for the different scan speeds, v at pulse energies**.** (a) E_p = 400 nJ, $NA = 0.6$ and (b) E_p = 600 nJ, $NA = 0.4$. The inset in panel (a) defines all the relevant quantities. The dashed line is a sinusoidal function plotted as a guide for the eye. Schematic markers show the average orientation of nanogratings (corresponding to an electric field along the y-direction) while the block arrows mark the scan direction; the markers are placed at the corresponding φ positions. This figure presents an analysis of the data partially shown in Figure 34. Error bars represent the standard deviation of data from five different analysed areas of nanogratings.

A substantial change in the period of nanogratings Λ was observed with a strong increase at around φ = π/2 and 3π/2 (Figure 35c). At these angles, the scan direction was perpendicular to the electric field $\boldsymbol{E}_y$ of the laser radiation. On the contrary, the smallest period was observed when the scan direction was parallel to the electric field. The strong dependence of the period on the orientation of scans is intriguing since the pulse energy was maintained constant and focusing was too loose (*NA* < *0.7*) to justify polarization effects at the focal spot, like those predicted by the Debye vectorial focusing [141]. The largest period Λ of nanogratings was observed at the orientation of the scanned lines where the width of the line *w* was minimal.

Differences in light absorption and heat diffusion for the different scan directions have been investigated, and they are discussed in the following section.

4.2.1 *A theoretical model of the nanogratings tilt*

Formation of nanogratings inside materials [14] and on the surface [34, 40, 142] are related to the same phenomenon in the case of dielectric materials [51, 56, 57, 133]. Inside transparent materials, the period of the nanogratings becomes intensity-dependent via the permittivity $\varepsilon \equiv (n+ik)^2$ at the focal volume and is approximately following the $\Lambda(I) \cong (\lambda / n(I))/2$ dependence, where n and k are the real and imaginary parts of the refractive index, respectively.

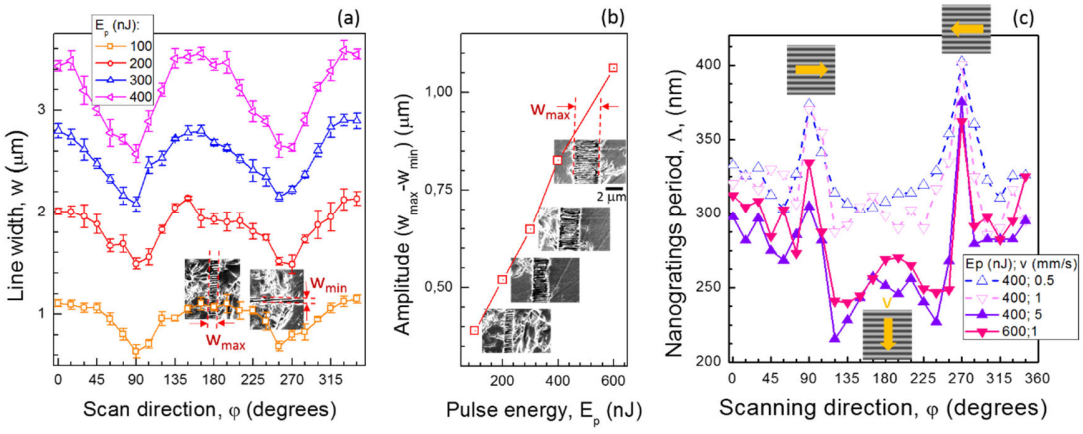

Figure 37 Dependence of the width and period of the nanogratings on the laser writing (scan) direction: (a) The width of the nanogratings, w, vs. scanning orientation, φ, at different pulse energies, E_p. Focusing was $NA = 0.5$; laser pulses at $\lambda = 1030$nm and $\tau_p = 570$fs (Pharos laser); (b) The span of the width of nanograting line ($w_{max} - w_{min}$) at different pulse energies E_p; (c) Period of nanogratings, Λ, vs. scan orientation, φ, at different scan speeds, v. Focusing was $NA = 0.6$; laser pulses $\lambda = 1040$ nm, $\tau_p = 317$fs (HighQ Laser). Insets in (a) and (b) show corresponding SEM images; arrow markers in (c) show the scan direction and schematic nanograting orientation. In all cases, polarization was $\boldsymbol{E}_y$.

A significant departure from such prediction was observed when surface plasma waves – the surface plasmon polaritons (SPP) - were excited at the interface of plasma and the dielectric inside the sample. The SPP wave between dielectric

(glass) and plasma can be launched when $\mathrm{Re}(\varepsilon_p) \le -n^2$, where ε_p is the permittivity of plasma at the focal volume (a necessary condition with the Bragg phase-matching being the satisfactory condition) [51, 143–146]. This follows from the requirement of the wave vector of the surface wave $k_{spp} = k_0\sqrt{\varepsilon_p\varepsilon/(\varepsilon_p+\varepsilon)}$ to be a real number, where $k_0 = 2\pi/\lambda$.

Nanogratings are imprinted at the plasma-dielectric interface with a period corresponding to the half wavelength of the standing wave, the Bragg condition. This is why a smaller period is expected for a larger plasma density (more negative values of $(-|\mathrm{Re}(\varepsilon_p)|)$), induced by a stronger absorption of the femtosecond laser pulses.

However, if the pulse energy is fixed, what can modulate the light absorption in the material? One possible mechanism is the incubation of defects in the heat-affected zone. In fact, defects or modified bonds induced by laser irradiation can favour ionisation when the same region is irradiated again by subsequent laser pulses. We can, therefore, expect that absorption in the area that has been heat-affected by laser irradiation will be enhanced with respect to absorption in an unmodified zone. Heat accumulation effects in fused silica are not dominating, in particular for a repetition rate of 500 kHz and bellow [109]. Therefore, a single-pulse modification of the material should be taken into account. This means that the incubation of defects should depend on the pulse energy and the number of pulses impinging on the same area and not on the time separation between laser pulses.

A careful analysis of the heat flow in the presence of E-field reveals that an anisotropic heat diffusion is present in a thermally isotropic material, and this causes a dependence of the absorption process on the scan direction. The heat conduction flux *q* in the plasma placed inside an external high-frequency electric field, linearly polarised along the y-direction can be expressed as [147, 148]:

$$q_\alpha = -\kappa_1 \frac{\partial T}{\partial \alpha} - \kappa_2 \left| \vec{e}_\alpha \cdot \vec{e}_y \right| \frac{\partial T}{\partial y}, \qquad (4.1)$$

where the unit vectors $\vec{e}_\alpha$ and $\vec{e}_y$ correspond to a generic direction α and the direction of the electric field in our case, respectively. The coefficients $\kappa_{1,2}$ are two scalar quantities obtained from the solution of the kinetic equation [147]. It follows from (4.1) that the heat diffusion process can be decomposed into two terms. The first one is a conventional isotropic heat diffusion, while the second one is influenced by the presence of the electric field and its orientation. In particular, the field-related term induces an enhanced heat flux in the direction of the electric field while its contribution vanishes in the direction orthogonal to the electric field. The heat affected zone, after the plasma creation in the focal volume is, therefore, asymmetrically shaped with an elliptical cross section (see Figure 37a), where the major axis is aligned with the linearly polarised electric field. The absorption of subsequent pulses with a strong spatial overlap (~10^3 pulses per spot in our experimental conditions) should thus be influenced by the shape of the pre-modified region. In fact, as previously discussed, the presence of defects in the heat-affected zones enhances the ionisation of the material with respect to unmodified zones. The asymmetry of the heat-affected zone can explain the observed variations in the nanograting period, width and tilt, as discussed in details in the following sections. It should be noted that the manifestation of such enhanced heat diffusion along the E-field in 3D laser printing has also been observed for the two-photon polymerization process [128].

4.2.2 *Explanation suggestion of the nanograting period and line-width*

Figure 37 shows a dependence of the width and period with respect to the pulse energy used to inscribe the nanogratings. In fact, for an increasing pulse energy, the width of the written lines expands, and the nanograting period shrinks for all

scanning directions. This general behaviour can be explained considering that the absorption process is nonlinear. Hence a higher pulse intensity can broaden the absorption volume (thus increasing the width of the nanograting region) and also increase the plasma density, and therefore, reduced transmission [149] (thus reducing the nanograting period, as discussed in the previous section). These two effects are rather straightforward, but they do not take into account that the width and period of the nanogratings can also vary for different scan directions using the same pulse energy. This aspect can be simple explained based on the theoretical model presented in Section 4.1.1. The largest periods of the nanogratings were observed at the scan orientations equal to $\varphi=\pi/2$ and $3\pi/2$, in correspondence to the minimum widths of the modified region. As previously mentioned, during the sample scanning, the laser absorption is modified by the defects accumulated in the heat-affected regions. However, as shown in (4.1), the heat diffusion process during the laser irradiation is anisotropic, and that creates a heat affected zone which is elliptical in the plane orthogonal to the direction of the laser beam propagation (see Figure 38a). As a consequence, the beam moving in different scanning directions encounters a material which has been more or less pre-modified and thus prepared to a larger or weaker absorption. Figure 38b-d clearly visualises three distinct situations. When the scanning direction is along the electric field ($\varphi=0, \pi$), the subsequent pulses encounter a pre-modified substrate and experience the maximum absorption. When $\varphi=\pi/2$ and $3\pi/2$, instead, the absorption is at the minimum, while, in all other directions, we have an intermediate situation. Since larger absorption leads to wider modification with a smaller nanograting period (due to higher plasma density), as already discussed, this mechanism fully explains the observed peculiarities in nanograting variation depending on the scanning direction.

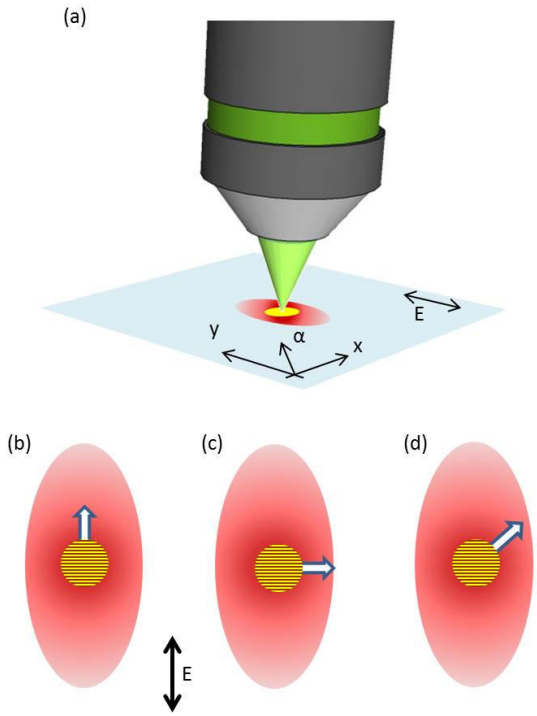

Figure 38 Schematics of the thermal diffusion process affected by the coupling between the plasma electrons and the electric field. (a) The anisotropic heat affected zone (red region) due to an enhanced heat flux along the electric field direction. Yellow spot represents the plasma in the focal volume. (b)- (d) Three different scan directions (represented by the arrows) oriented relative to the heat affected region. The average orientation of the nanogratings is also schematically reported as a reference.

4.2.3 *Explanation suggestion of the nanograting tilt*

The tilt of the nanograting orientation is an even more puzzling phenomenon which was observed here for the first time (Figure 36). No tilt of the nanograting orientation was observed for the scanning directions corresponding to $\varphi = 0, \pi/2, \pi$ and $3\pi/2$; while the maximum rotation was observed for $\varphi = \pi/4, 3\pi/4, 5\pi/4$ and $7\pi/4$.

Since the formation of nanogratings is defined primarily by the electron plasma excitation, initially, the possible role of the temporal and spatial chirp of the ultra-short laser pulses was investigated. Temporal and spatial chirps were measured, varied and correlated with the tilt and period of nanogratings. Both the temporal and spatial chirps were found having an influence on the tilt of the nanogratings, but

only at very large chirp values. At the conditions used in the experiments presented here, the pulse duration was the shortest, and the pulse front tilt was negligible. Therefore, temporal and spatial chirps cannot be invoked to explain the nanograting tilt dependence on the scanning direction.

The same theoretical model, used to explain the dependence of the width and period of the nanogratings, can also explain the tilting effect. The conditions when no tilt was observed corresponded to a symmetric heat affected zone with respect to the scanning direction (see Figure 38b, c), while the maximum tilt was observed when the heat affected zone had the largest asymmetry with respect to the scanning direction. The symmetric heat affected zone means that the subsequent pulses hit an evenly preheated material. Thus, the absorption process is the same in the whole focal volume, and the symmetry of the process forces the nanograting wave vector $\boldsymbol{K}$ to be parallel or orthogonal to the polarization. On the contrary, when the heat affected zone is asymmetric with respect to the scanning direction, absorption is different on the two sides of the focal volume, and that induces a nanograting period which is shorter (longer) at the pre-modified (unmodified) side. As a consequence, the overall nanograting orientation is affected, with the wave vector $\boldsymbol{K}$ rotated toward the pre-modified side.

As an example, the situation for $\varphi = \pi/4$ is presented schematically in Figure 38d. In this case, each new-coming light pulse meets the material that it hotter on the left side of the scanning direction and colder on the right side. Therefore, the periodicity of the nanogratings (generally orthogonal to the electric field direction) is slightly reduced on the left side comparing to the right one. This results in a negative tilt $\Psi<0$ of the nanogratings for this particular scanning direction, what is exactly observed experimentally (Figure 36).

Figure 36 also shows that the amplitude of the nanograting tilt increases with the pulse fluence (compare panel (a) and (b), where a fluence of 11.4 J/cm^2 and 7.6 J/cm^2 was used, respectively), while the dependence on the scanning direction is the same. This further feature can also be explained by the above model. In fact,

a larger pulse fluence means a stronger temperature gradient induced in the focal volume. According to (4.1), that corresponds to a stronger contribution of the field-related term in the heat diffusion process, resulting in a more elliptical heat affected region. This causes even stronger unbalance of the material temperature on the two sides of the scanning direction at $\varphi = \pi/4$, thus inducing a stronger rotation of the nanograting orientation. Consistently with the proposed model, a larger tilt was observed for the larger pulse fluence.

Further studies are required to elucidate the effect of stress in writing of nanogratings. A presence of stress can cause alterations in heat transport in silica [150]. It could be expected, that coupling between the pulse front tilt and stress takes place, however, in all our experiments the tilt of nanogratings was extracted from experiments with the chirp-free (temporal and spatial) pulses. Also, if stress was playing a significant role in the tilt of nanogratings, one would expect a strong variation of the effect at the different depths, according to a non-uniform stress distribution in that direction [151]. However, that was not observed experimentally. Stress distribution around the affected zone was investigated earlier [152], showing a dependence of the generated amount of stress on the scan direction. However, no stress asymmetry was observed around each scan line [152] that could justify the nanograting tilt discussed in this work.

4.2.4 *Influence of the pulse front tilt (PFT)*

Dependence of the nanograting tilt on the temporal pulse chirp γ was measured by changing the pulse compressor grating position, hence, varying the second order dispersion of the fs-laser pulse. The compressor position for the shortest pulse duration corresponded to the chirp-free or Fourier transform limited bandwidth pulses with the chirp parameter $\gamma = 0\,\mathrm{fs}^{-2}$. The pulse duration was measured by an SHG-FROG algorithm using (Ekspla, Ltd).

The spatial chirp measurements were carried out directly on the target by mounting the single shot autocorrelator (TiPA, Light Conversion) instead of the sample without a microscope objective. In this way, any tilt induced in the optical path was taken into account. The pulse compressor design in the used lasers can affect the pulse front tilt at the laser output (along the X-axis), i.e., when scanned at $\varphi=\pi/2$ direction, there could be a difference in the pulse arrival time on the target at the outmost left and right parts of the focal spot, a "quill writing" effect (inset in Figure 39c). The temporal and spatial chirps were measured for this $\varphi=\pi/2$ condition. It is noteworthy, such measurement characterises laser pulses of the fundamental wavelength of 1030 nm and not directly of the second harmonics at 515 nm which was also used in the nanograting formation. The pulse duration at SHG was estimated from an I^2 envelope of the Gaussian pulse. The second harmonics pulses are usually preferable for laser structuring since the excitation of plasma by a nanosecond pedestal that can present for the pulses at the fundamental frequency can be avoided [153] (peak the intensity of the pedestal is only10^{-3}, however, the entire energy can be substantial due to long ~ 20 ns duration). Figure 39 summarises experimental observations of the chirp measurements.

The temporal chirp was tuned by the pulse compressor stage position (Figure 39a, b). Around the shortest pulse $\tau_p=260$ *fs* setting of the compressor stage, there was a sign change of the nanograting tilt angle from negative values $\Psi < 0$ (at $\gamma < 0$) to the positive ones $\Psi > 0$ (at $\gamma > 0$), however, the overall effect was not strong. Experiments showed that no tilt could be expected $\Psi \cong 0$ for the shortest pulse ($\gamma=0$). For the strongly positively chirped pulses, a tilt of nanogratings returned to negative values $\Psi < 0$ (Figure 39a). The front tilt measurements were carried out with a 2-mm-diameter beam at the target location using the Pharos laser. The pulse front tilt at the compressor settings around the shortest pulse duration showed a presence of the $\theta \cong (0.15 - 0.5)°$ pulse front tilt (Figure 39c) for $\gamma \cong \mp 2\,\mathrm{fs}^{-2}$ (i.e., pulse duration was changed by a factor 2.2 times as

compared to the shortest pulse setting). The sign of the pulse front tilt was always the same. The spatial chirp can be considered negligible at the compressor position corresponding to the shortest pulse (close to the bandwidth-limited duration).

By the focusing of the 1 μm wavelength laser pulses with a commercial objective lens optimised for the visible spectral range, it is expected to increase the pulse front tilt. Even for exaggerated θ=1° the difference between the left- and right-side (see the top-view image in the inset of Figure 39c incidence correspond to only $d\tan(1°) \cong 22$ nm for the d = 2.5 μm-diameter focal spot or ~0.2 fs in time inside the glass. Even though these values appear small, they can still play an important role at ~ 1 TW/cm^2 peak intensities in the electron generation rate since the plasma density can change by a factor of two (or more) within of an optical cycle of ~ 3.5 fs [154]. The electron-ion relaxation time is even shorter ~ 1.1 fs [155] at the glass breakdown conditions, and the "quill writing" effect pushing electrons by the tilted pulse front can influence the formation of self-trapped excitons and defect formation at later times (~ μs).

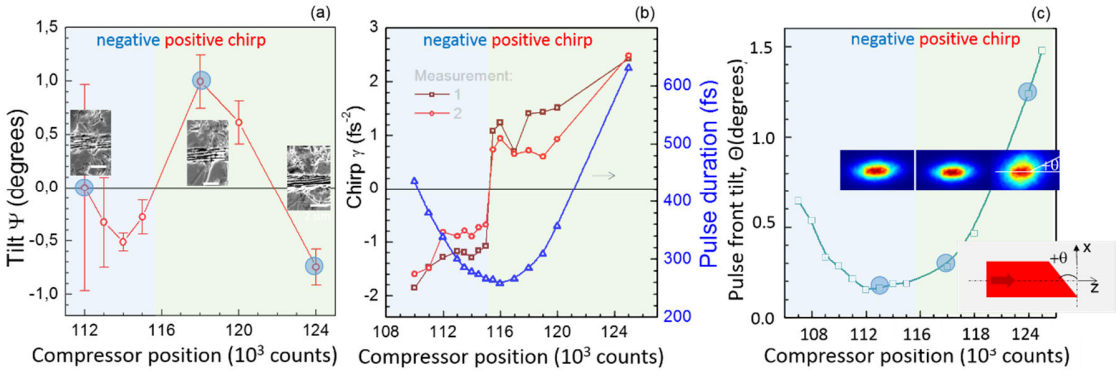

Figure 39 Spatial and temporal chirp influence to the nanograting tilt angle**.** (a) The tilt angle Ψ vs. compressor position (a measure for a temporal chirp, γ). Insets show corresponding SEM images of nanogratings at three different compressor positions; (b) The chirp, $\gamma[\text{fs}^{-2}]$ and pulse duration, τ_p, dependence on the compressor setting. Two scans of compressor stage in positive and negative directions were carried out; (c) Spatial chirp, the pulse front tilt vs. the compressor position. Insets show corresponding second harmonics intensity distribution profile measured by single shot autocorrelation; top inset shows schematically the spatial chirp (pulse front tilt) along the propagation (z-axis). Laser pulses were λ = 1030 nm , τ_p = 260fs (Pharos).

The first observation of the “quill writing” effect [156] was analysed considering much higher intensities and several degrees of the front tilt when the difference in structural changes of glass along two opposite directions of a scan was observed.

In conclusion, we demonstrated that the pulse front tilt and chirp parameters at the 1030 nm wavelength can induce negligible nanogratings tilt effect (< 1 degree) when the constant pulse energy is used. However, the experiments of the star writing were performed using the shortest pulse duration when any PFT influence was eliminated. The more detailed investigation on the nanogratings tilt dependencies was performed with the 515 nm wavelength. In Section 4.3.4, we demonstrate the significant pulse front tilt and pulse duration influence to the nanogratings tilt when various pulse energies were used.

4.3 Nanograting rotation using a laser with the 515 nm wavelength

Induced rotation of nanoplanes embedded in fused silica under the tightly focused 515 nm femtosecond laser pulses at a 5-10 μm depth were systematically studied. A significant > 3 degrees tilt of nanogratings from the polarization orientation at different scan directions was observed, and it was larger than the tilt for the gratings recorded using the 1030 nm wavelength. The tilt was dependent on the pulse energy, pulse front tilt of the laser beam, and pulse duration at the constant pulse intensity for the fixed scan direction. An asymmetrical heat distribution on two sides of the scan-line can be responsible for the tilt of nanogratings.

4.3.1 *Orientation instabilities of nanogratings fabricated with 515 nm wavelength*

The experiments performed with the 1030 nm wavelength were repeated using the 515 nm wavelength. Hence the 515 nm wavelength is generated in a nonlinear crystal, the larger intensity of 1030 nm pulses is required to increase the SH generation efficiency. Therefore, the shortest pulses should be used. It can be supposed that nanosecond pedestal emergent for 1030 nm should be separated by

the nonlinear crystal. For that reason, the results achieved with 515 nm can differ from that using 1030 nm and should bring the major interest.

The femtosecond Pharos laser operating at the 515 nm wavelength and 500 kHz repetition rate was used to record the embedded nanogratings inside fused silica with the system described in Section 2.1. The star pattern was inscribed with the shortest pulse duration of ~ 260 fs with ~ minimal PFT and the 0.25 mm/s scanning speed. The detailed fabrication method of subsurface nanogratings is described in Section 2.5.

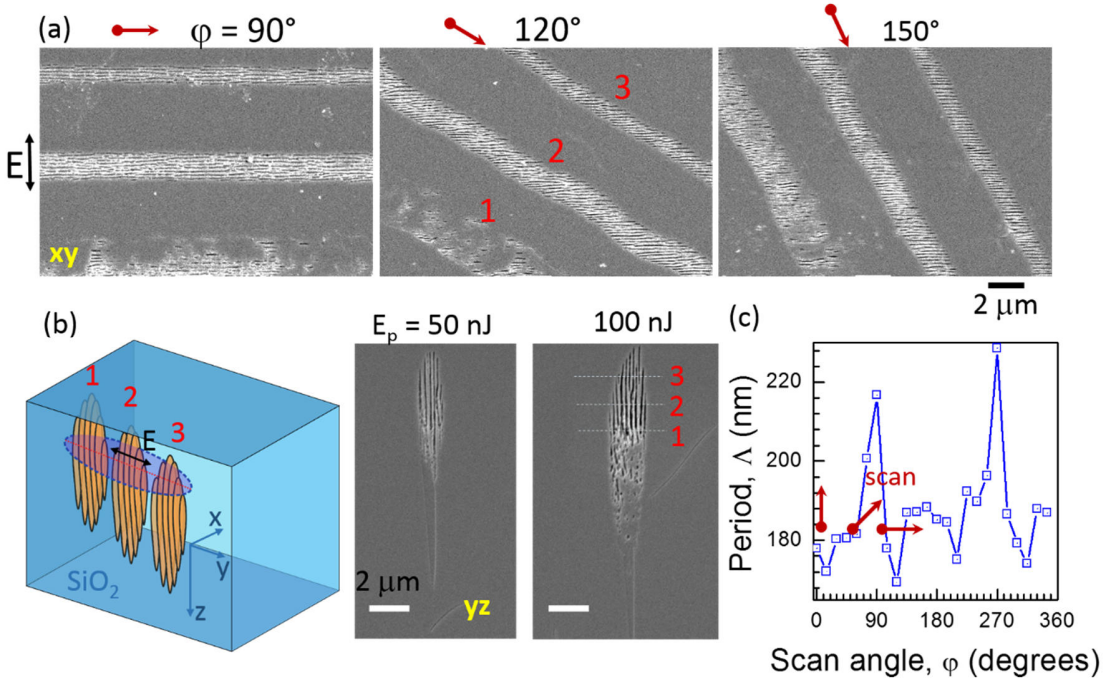

Figure 40 (a) SEM images of nanogratings recorded with λ=515 nm wavelength fs-laser pulses at various scan directions φ (scan along x-axis corresponds to φ = 90 deg). Pulse duration was τ_p=264 fs and energy E_p=150 nJ at a repetition rate f = 500 kHz. SEM images of the nanograting cross sections are shown from two perspectives: front-view xy-plane (a) and side-view yz-plane (b) for two pulse energies E_p = 50 nJ and 100 nJ; scale bar 2 μm. (b) Schematic 3D view of nanogratings; (c) Period of nanogratings Λ vs. scanning angle φ for the pulse energy E_p = 200 nJ at 0.2 mm/s scanning speed; polarization linear $\mathbf{E}_y$.

The revealed nanogratings recorded at different scan directions are shown in Figure 40 for two perpendicular cross-sections. The length of modification was ~ 15-20 μm (yz-plane) with the strongest modification length of ~ 3-5 μm. Few modification lines were recorded at the same scan angle but different depth with the

Z-step of 1 µm to increase a probability of successful cross section for the SEM analysis. Hence, the XY-plane cross-section in Figure 40 shows three lines made for the same scan angle at three different depths inside the sample.

The tilt angle Ψ of the nanogratings was determined by the procedure described in Section 4.1.

4.3.2 *Dependence of the nanograting tilt on the pulse energy*

It is accepted by default that nanogratings are always perpendicular to the linear laser polarization [81]. However, in most of the experimental studies, nanogratings appear slightly tilted. Among possible reasons considered is depolarization of the laser beam upon delivery to the sample. The main way how to rotate the nanogratings orientation is the rotation of the laser beam polarization during the inscription experiments. Physically, the different nanograting angle was recorded by changing the rotation angle of the half-waveplate around its optical axis. The half-waveplate physical angle ϕ was rotated by 1-degree increment in the range from 0 to 45 degrees. Two sets of the experiments in fused silica with two different pulse energies were performed. The ϕ = 0° half-wave plate orientation (angle) corresponded to the $\mathbf{E}_y$ polarization. The nanograting orientation angle Ψ' was measured in relation to the image X-axis. All subsequent nanogratings angles for each half-waveplate angle value ϕ were measured in the same manner and then were compared relatively with the 100 nJ pulse energy. Results of the nanograting rotation angle vs. the waveplate physical rotation are summarised in Figure 41.

Normally, it is believed that the pulse energy is not related to the nanogratings rotation, however here it was found that the nanograting recorded for a constant half-waveplate angle with two different pulse energies were rotated at different angles in relation to the image X-axis. Subsequently, the nanogratings possessed energy dependent tilt angle ($\Psi'(\phi; E_p$=200 nJ)- $\Psi'(\phi; E_p$=100 nJ),) which can be as large as ~ 10° for ϕ=0° (Figure 41). For the largest used pulse energy of 200 nJ, the

nanogratings rotated clockwise in relation to the orientation observed for the smaller 100 nJ pulse energy. Interestingly, when the physical angle of a waveplate approached ϕ=45°, the difference between the tilt angles of nanogratings recorded using two different pulse energies (100 and 200 nJ) vanished (Ψ' (ϕ=45°; E_p=200 nJ) - Ψ' (ϕ=45°; E_p=200 nJ) ~ 0°. The nanogratings became nearly perpendicular to the scan direction. The linear fits show different curves slope coefficients of 2.29 for 100 nJ and 2.13 for 200 nJ which corresponds to the 1.56° angle difference between the fitted curves. The intersection of the curves was observed at the ϕ ~ 45° waveplate position.

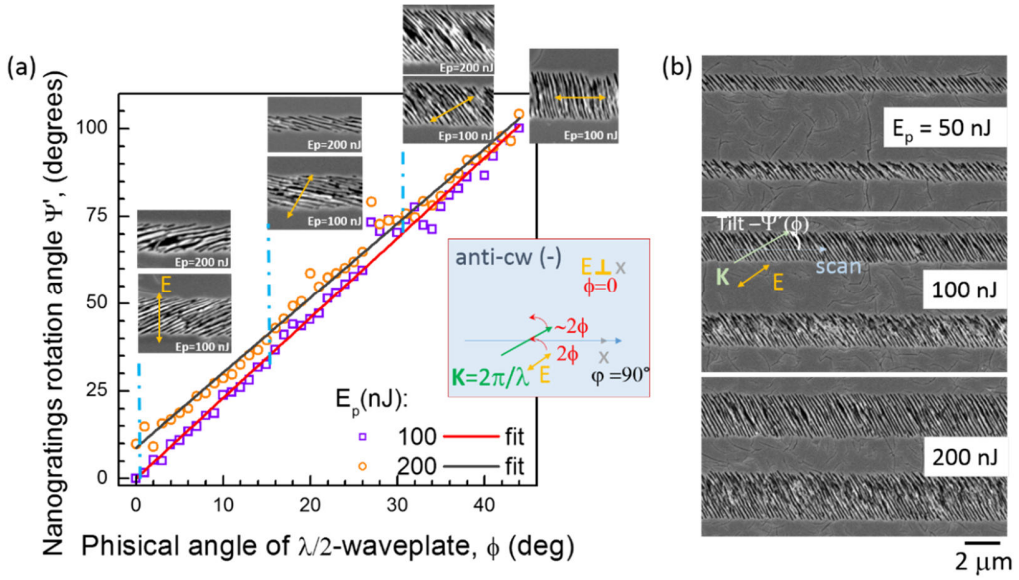

Figure 41 (a) Nanograting rotation angle Ψ' for different phase plate physical angles rotation for the 515 nm wavelength. The phase plate was rotated with a 1-degree incremental step which corresponded to the 2 degrees polarization rotation. The insets show the SEM images of the nanogratings for few selected polarization angles; (b) SEM images of the nanogratings recorded at 22.5 degrees $\lambda/2$ phase plate angle using pulses of τ_p=743 fs duration at different pulse energies. The two lines per a single energy image were recorded with Δz = 1 μm shift (cross sections 2 and 3 in the convention shown in Figure 40). Incident E-field polarization is shown as polarization after passing the $\lambda/2$-waveplate.

It should be noted that the nanogratings recorded at ϕ=0° (Figure 41 a, left side inset) are orientated not strictly along the X-axis. Such deviation can be caused due to this reason: the zero-degree orientation of the half-wave plate was calibrated by using the Glan prism polarizer by measuring the minimum transmitted laser power.

The error due to the human factor can be as large as ~ 1-3 degrees for the polariser rotation that should correspond to ~ 2-6 degrees of the nanogratings rotation. However, even when we take into account this error, the initial nanogratings orientation could be as high as ~ 14 degrees for 100 nJ and ~ 4 degrees for 200 nJ pulse energy in relation to the image X-axis for the half-wave plate at ϕ=0° position. Following, the human error factor can partially explain the primary nanogratings orientation not perpendicular to the X-axis and cannot rebut the energy dependent nanogratings tilt.

4.3.3 *Analysis of nanograting tilt*

The nanogratings were recorded at different scanning directions by scanning the star pattern with lines of $\Delta\varphi$=15° scan angle increment (Section 4.1). The five sets of stars were recorded where for each set the constant linear polarization was used with the following half-waveplate physical angles ϕ*:* – 15° for 1 set, 0° for 2 set, 10° for 3 set, 15° for 4 set and 30° for 5 set. The $\phi = 0°$ angle corresponds to the $\boldsymbol{E_y}$ polarization vector. The different nanograting tilt angles were expected. For ϕ = 0° half-waveplate physical angle the wavevector of nanogratings $\boldsymbol{K} = 2\pi/\Lambda$ was perpendicular to the stages X-axis. The nanogratings rotated anti-clockwise, and their tilt was minimum at ~ π/2 scan angle. For the large scan angles, the rotation direction changed to the clockwise. The 0° tilt angle was achieved for the $\varphi \sim \pi$ angle when the electrical vector was parallel to the scan direction. The maximum tilt was obtained for $\varphi \sim 3\pi/4$ scan angle when the electrical vector was perpendicular to the scan direction. The maximum tilt angle of ~ 3° was observed. Comparing with the 1030 nm tilt results, the approximated sinusoidal function for the 515 nm wavelength results have a twice longer period and consequently the tilt minimum was shifted from ~ π/4 to ~ π/2 scan angle. For 515 nm, only one minimum and one maximum were observed during the star writing cycle.

The dependencies presented in Figure 42 show the nanograting tilt for the five recorded stars sets. For each set and the same scanning direction φ, the different nanograting tilt and tilt propensity were observed. The reference for the tilt angle measurement was the scan direction φ where the nanogratings were perpendicular to the scan direction (electrical vector was along the scan direction). All 24 modifications were initially analysed, and the reference scan direction where the nanogratings are perpendicular to the scan direction was selected for the relative tilt angle calculation. To demonstrate what is the difference between the nanogratings tilt tendency recorded in different stars sets, we compared the scanning angle difference between two sets where the maximum (or minimum) tilt angles were observed. According to our concept, the scan angle difference in two different sets where the nanograting tilt was maximal (minimal) should be equal to the linear polarization orientation difference for which the star set was recorded. For example, for the set recorded at ϕ = 30° half-wave plate angle and the φ=0° scan angle, the nanograting tilt corresponded to the negative tilt values, and the maximum tilt angle was at ~ 75-105 degree scan angle. For the set recorded at ϕ = 15° half-wave plate angle, the maximum tilt angle was achieved at the 45-75 degree scan angle. Taking into account the measuring errors, the difference between maximum tilt angles for two stars sets (ϕ=30° and ϕ=15°) was with an average value of ~ 30 degrees, which corresponds well with the half-wave plate rotation by 15 degrees or 30 degrees linear polarization rotation.This behaviour additionally proved the existence of the nanograting tilt.

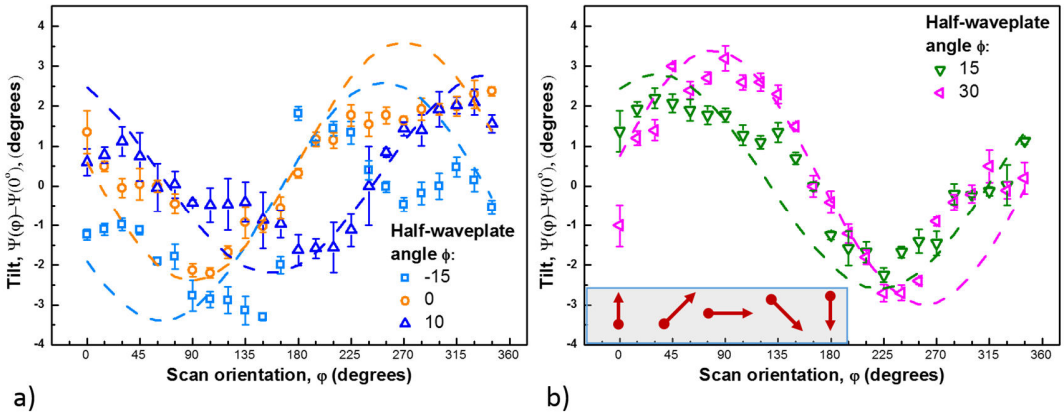

Figure 42 Nanogratings tilt angle orientational distribution *Ψ(φ)* for different stars set recorded at: a) -15, 0 and 10 half-wave plate angles; b) 15 and 30 half-wave plate angles. The pulse energy E_p = 150 nJ was constant for all sets. Pulse duration was 264 fs and focusing with the NA=0.55 objective. The inset with the red directional arrows indicates the scan direction. The dashed line is a sinusoidal function plotted as a guide for the eye

The direction of the nanograting tilt is qualitatively discussed next. As it has been shown in [128], the electron scattering and reduction of its mean free path is the key to the understanding of excessive heating via coupling the temperature gradient and the electrical field vector. When the line is scanned at φ = 45 degrees and polarization is $\mathbf{E}_y$, the most different modification takes place on the opposite sides from the scan line. Due to the polarization and temperature gradient coupling [119, 128], an enhanced thermal diffusion along polarization direction of E-field takes place. Hence, an excessive defects generation and, consequently, heat accumulation occurs on the anti-clockwise side causing anti-clockwise tilt (towards hotter side) as it was demonstrated in [119]. The strongest laser pre-modified zone and structural defect creation takes place when the scan and polarization directions are aligned and the lowest when they make an angle of φ = 90 degrees. The consequence of the enhanced heating leads to stronger absorption and smaller periods as commonly observed in nanogratings on surfaces and in the volume [51]. Thermal disbalance on two opposite sides of the scan line causes a slight difference in the period which is imprinted as a tilted from the E-field orientation [119]. For the twice shorter wavelength (515 nm), an approximately twice larger period of the sinusoidal

function eye guided fit was observed. We discuss this difference as being due to the twice shorter nanogratings period that increases heat localisation (a shorter free mean path of heat carriers).

4.3.4 *Pulse duration and pulse front tilt influence on the nanograting tilt*

A few more laser processing factors were found having an effect to the nanograting tilt: the pulse duration, spatial pulse chirp, or pulse front tilt (PFT). Six pulse durations with negatively and positively chirped pulses were chosen to record a set of sub-surface nanogratings (Figure 43). Since the pulse intensity was different for different pulse durations, two cases were investigated: (i) tilt of nanogratings at the constant pulse energy and (ii) at the constant pulse intensity (the corresponding compensation of the pulse energy was applied).

The tilt angle measurement was carried out as described in Section 4.1. In the constant pulse energy case, three different pulse energies of 50, 100 and 200 nJ were tested in 2 experimental sets. 1 set the 45° polarization, and for 2 set the 90° was used (Figure 43b). In all cases, the minimal nanograting tilt was observed for the shortest pulse duration of ~ 264 fs (reference position). The tilt angle was calculated relative to the lowest pulse energy of 50 nJ. It was observed, that by measuring the nanograting tilt relatively to the shortest pulse duration and lowest pulse energy (reference position) the change of the tilt with the absolute tilt values up to ~ 17.5° can be seen when the larger pulse energies are used. For the longest pulse durations (both negatively and positively chirped pulses), the tilt angle exhibited maximal changes and gradually was decreasing by approaching the shortest pulse duration. For the negatively chirped pulses and therefore the maximal PFT value, the counter-clockwise rotation of the nanogratings was observed going to the shortest pulse duration and the opposite rotation from the shortest pulse in the direction of the positively chirped pulses that correlates well with the PFT signs direction. Starting

with 100 nJ pulse energy, the tilt angle for the 90° polarization shows lower changes that for 45° polarization state.

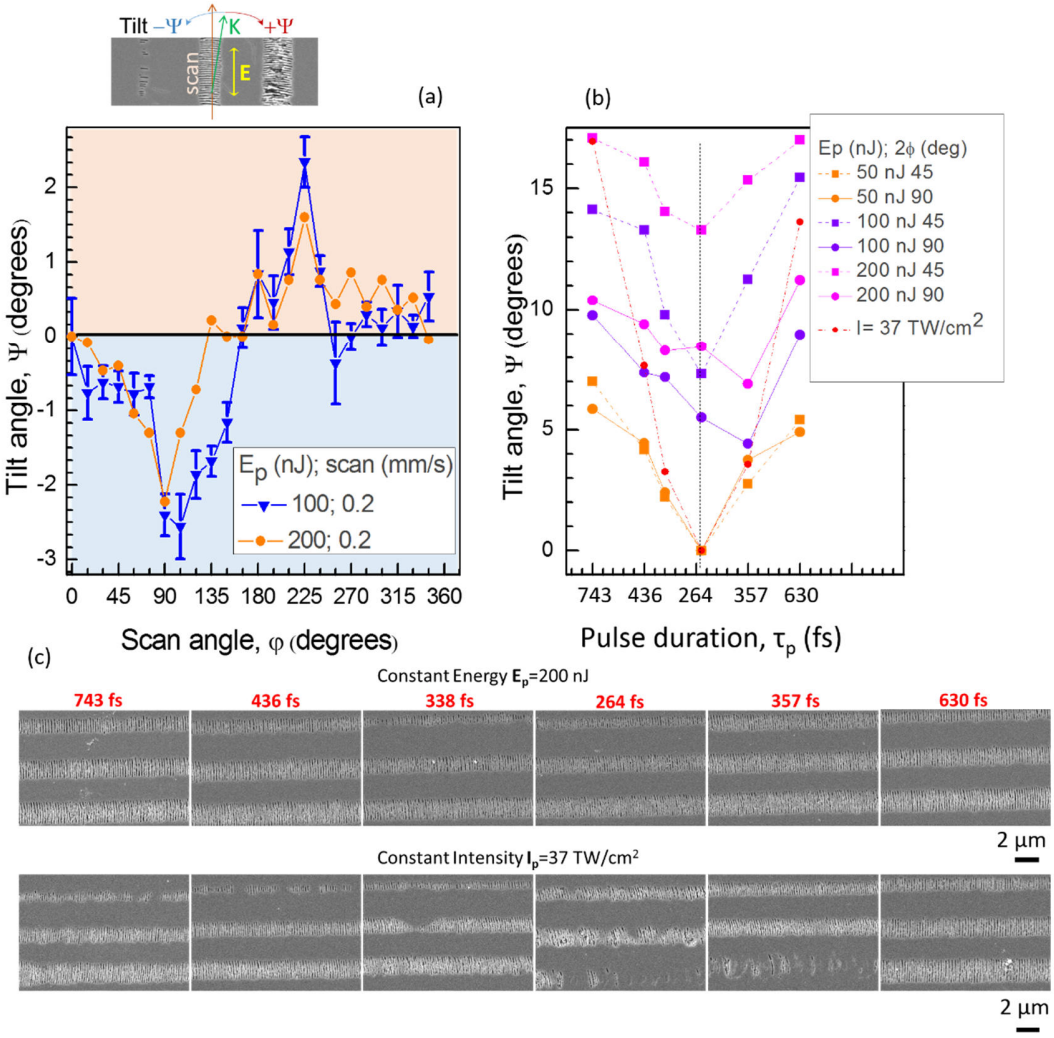

Figure 43 Orientational distribution of the nanograting tilt angle Ψ(φ) depending on the laser pulse duration for a) the constant pulse duration of ~ 264 fs and different scan angle; b) the constant pulse energies of E_p = 50, 100 and 200 nJ and the constant pulse intensity of I_p = 37 TW/cm^2 (100 nJ pulse energy at shortest pulse duration of ~264 fs); c) SEM images of the nanogratings at the ϕ=0° polarization orientation for various pulse durations.

The differential behaviour of the maximal and minimal changes for different pulse energies is the following: 1) for the 45° polarization, the maximal tilt difference was achieved for the 100 nJ pulse energy and decreased for larger pulse energies; 2) for the 90° polarization, the tilt angle linearly decreased in the direction of larger energy values. Such behaviour shows the difference between two

polarizations that can be influenced by a different and non-symmetrical (in respect to the scanning direction) material heating for various polarization orientation [128]. When the pulse energy was kept constant for different pulse durations, very similar nanogratings were formed in terms of the pattern width and period of nanogratings (Figure 43c). Next, the reference pulse energy of 100 nJ for the shortest pulse duration was selected (corresponded to the 37 TW/cm^2/pulse intensity), and nanogratings were recorded at the constant intensity (Figure 43c). The orientation of nanogratings was the same as for the constant energy case, and the nanograting tilt angle difference between maximal and minimal pulse duration was ~ 17.5° which is ~ twice larger than that observed for the constant energy case. The nanograting tilt for three different constant linear polarizations of 0°, 45° and 90° was approximately the same.

Two aspects are noteworthy for the constant pulse energy case. The pulse intensity dropped for longer pulses, and the shortest pulse duration was ~ 2 times larger than in the constant intensity case. Secondly, the larger nanograting tilt was always observed for longer pulse durations even for the lower intensity. The SEM images (Figure 43c) show better-evolved nanogratings quality for longer pulses judged by a wider extension in the z-direction (and wider in the lateral cross section). The nanograting tilt observed in this experiment was influenced by a combination of PFT and the pulse energy. The influence of PFT can be extracted from the constant energy experiments, and the combination of PFT and pulse energy was observed in the constant intensity data. In the latter case, the pulse energy was increased to achieve the same intensity. It was found that PFT was always the same for the fixed pulse duration (defined by compressor position). The increased pulse energy caused the clockwise nanograting rotation in agreement with non-even heating around the scan line [119, 128] discussed in Section 4.2.3.

It should be noted that the experiments for the 1030 nm wavelength were carried out with a constant pulse energy and linear polarization, and only the scan direction was varied. Such kind of experiments was performed firstly and demonstrated the

new phenomena of the nanograting tilt effect. Further, the experiments with the 515 nm wavelength were performed, where the nanogratings tilt was measured not only for the constant pulse energy. Various parameters were varied: the pulse front tilt (as it showed larger influence to the nanogratings tilt), pulse energy and pulse duration. In this case, the different references were selected to estimate the different nanogratings tilt values. The 17.5° nanogratings tilt was noted when the reference was: the shortest pulse duration and smallest pulse energy for the fixed scan direction.

4.4 Conclusions

- A systematic study of the main nanograting features relative to the direction of the laser beam scanning was carried out in a broad range of the parameter space. In particular, the influence of different pulse energies, scanning speeds, focusing, and temporal and spatial chirps were investigated. In all these conditions, it was shown for the first time a reproducible dependence of the nanograting width, period and tilt on the scanning direction, which can affect the performance of directly written photonic components based on the properties of the nanogratings, as the laser-written *q*-plates.
- For the fundamental wavelength (1030 nm) and linearly polarised laser pulses at the constant pulse energy, the strongest variations of the nanograting width and period were observed for the scanning directions parallel and perpendicular to the electric field direction while the maximum tilt of the nanograting orientation was observed when the scanning direction was at $\varphi=45°$ relative to the electric field direction. All these observations can be consistently explained by an anisotropic heat-diffusion model which takes into account coupling of the hot electrons in the plasma with the pulse electric field, enhancing the heat diffusion in the direction of the latter. This anisotropic heating of the substrate could be responsible for a modulated absorption of light along the different scan directions and explains all the observed phenomena.

- The experimental results represent a clear evidence of a polarization-affected light-matter interaction process. The observed features are expected to be even richer in the case of vector beams and at the tight focusing, where the vectorial nature of light has a strong presence. This work paves the way to a clearer understanding of these phenomena and their exploitation for optimisation of current devices and the design of innovative ones taking full advantage of the vectorial aspects of light-matter interaction.
- The tilt of nanogratings formed with the 515 nm femtosecond laser pulses was systematically studied at various fabrication parameters: scan angle, pulse energy, pulse intensity, pulse duration and pulse front tilt. At this second harmonic wavelength, there is no ns-pulse pedestal, and the investigated nanograting tilt dependencies were separated from other heating and absorption mechanisms which are essential for this phenomenon. The tilt was observed by scanning the nanograting structures by forming a star pattern. The maximum tilt angle exceeding $\Psi=3°$ was measured for the 150 nJ pulse energy at the $\pi/2$ and $3\pi/4$ scan angles using the ~ 260 fs-long pulses and polarization perpendicular to the x-axis ($\boldsymbol{E}_y$). By changing the constant polarization direction for each star set, the corresponding tilt of nanogratings was accordingly shifted (followed E-pol.).
- The precise nanograting tilt investigation on the half-wave plate orientation angle for a few different pulse energies for the 515 nm wavelength showed evident nanograting tilt dependence on the pulse energy. The differential tilt change was maximal for polarization perpendicular to the writing direction and vanished for polarization parallel to the writing direction.
- The further investigations demonstrated that combination of the pulse energy, pulse duration and pulse front tilt in the 515 nm wavelength case could induce the tilt angles as high as $\Psi=17.5°$. The larger nanograting tilt angles can be achieved for longer pulse durations referencing to the shortest pulse duration.

The nanograting quality and propensity also increased for longer pulse durations. These observations are important for practical applications of nanogratings in optical memory and formation of polarization optical elements.

5 Microfluidic devices

The results presented in this section were published in articles [P2, P3].

All experience achieved from the experimental microchannels writing activity was used to fabricate micro devices. During the microchannels writing, the required parameters were found which were used as input parameters for the 3D microfluidic devices recording. Due to the complex structure of the microfluidic devices, the geometry compensation and etching parameters adjustment were performed. The different functionalities of the microfluidic devices were demonstrated: from micropump devices to microfluidic device for the ellipsometric application and microfluidic aspherical lens.

Development of the method for formation of three-dimensional (3D) structures etched in bulk fused silica is presented. 3D structures were inscribed inside the transparent material according to the designed 3D CAD drawing and etched with hydrofluoric acid. Two different scanning strategies were used to investigate the volume etching rate. The main technique in this thesis for the formation of three-dimensional structures was based on the laser direct writing by scanning the multiple line arrays slice by slice inside fused silica to obtain rectangular channels. Complex 3D structures were formed by applying different scanning strategies in combination with linear and circular polarization and different pulse energies when the laser fluence was sufficient to induce the type-II modification in fused silica.

5.1 Slice by slice 3D structures with two scanning strategies

In order to get the true 3D structure in a transparent material, the prepared 3D drawing was sliced into layers in the z direction. The distance between slices was kept constant during the experiments (3.5 μm). Two different scanning strategies – lines and contour scanning – were used to investigate the etching rate (Figure 44a, b). The distance ***dl*** between scanning lines was changed from 2 to 3 μm during the experiments.

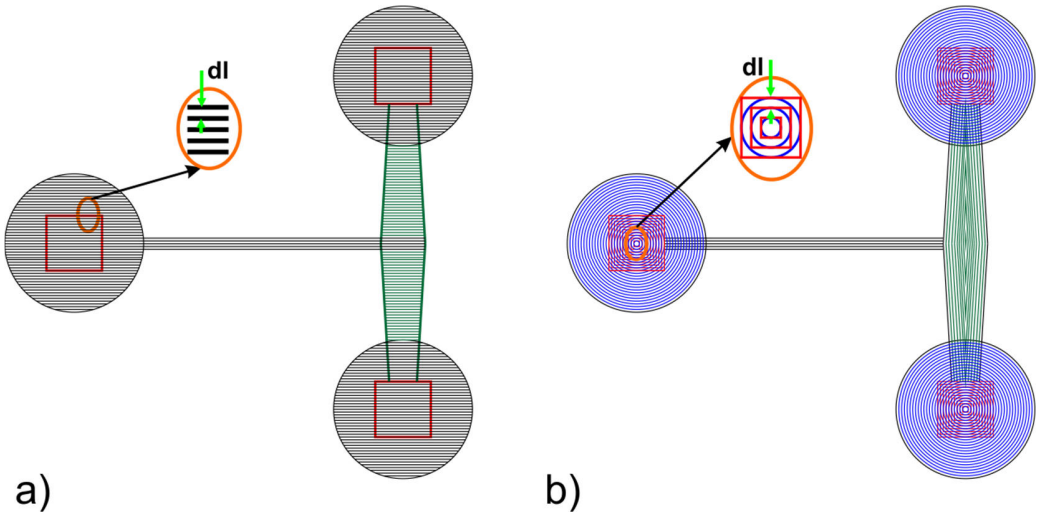

Figure 44 The principle of 3D structure formation by two different scanning strategies: a) Lines scanning strategy (***dl*** – distance between scanned lines); b) contour scanning strategy (***dl*** - distance between contours).

The microstructures for etching testing (Figure 45) were formed using various laser pulse energies. This structure was formed to have one narrow channel perpendicularly oriented to another wider channel with two acid access terminals. In this way, the acid can access the laser-written microstructure in different directions and penetrate to the different volumes along or perpendicular to the formed nanogratings. The laser pulse energy was changed in the processing window where the nanogratings can be formed as was shown in [118] to achieve the highest etching rate. The micro devices were formed using pulse energy 200 nJ, 400 nJ and 600 nJ and the linear polarization perpendicular to the scan (***X***-axis) direction and with the circular polarization using pulse energy of 400 nJ and 600 nJ.

The scanning was performed by the contour scanning strategy that facilitated the penetration of HF acid to the modified region (the polarization was maintained perpendicular to the X-axis). In the case of the contour scanning, the acid always penetrates to the modified region along the scan line direction, and for the line scanning, the acid can penetrate perpendicular or along the scanning line depending on the structure orientation. The etched volume for a micro device fabricated with the different writing parameters was inspected by immersing the sample in 10% HF acid for 13.5 hours. After 6 and 10 hours, the sample was pulled out, and the

removed volume was registered. Figure 46 shows the dependence of the normalised etched volume on the etching time. Some micro device structures were fully etched only after 13.5 hours of etching and fluid transportation through the hollow cavities was implemented.

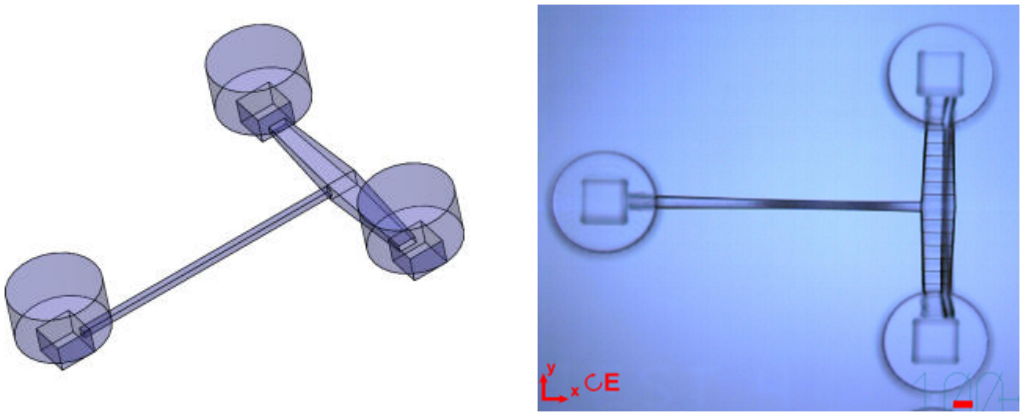

a) b)

Figure 45 a) 3D model of the microdevice for testing applications; b) microstructure modified with the femtosecond laser in fused silica and etched in 10% HF acid for 13.5 h. The red bar indicates 100 μm.

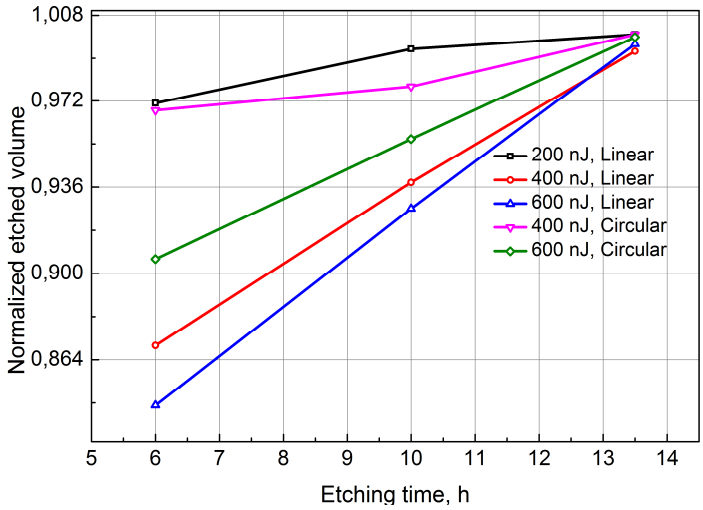

Figure 46 Dependence of the etched volume of the micro device structures formed with the contour scanning on the etching time when linear and circular polarizations were used. The total volume of a micro device was ~ 0.79 mm^3

The maximum etching rate was achieved for the structures fabricated using the pulse energy of 200 nJ (for the linear polarization) and 400 nJ (for the circular

polarization) that may slightly vary with the results achieved for the single channels writing (Chapter 3) due to interaction of the adjacent modifications. As can be seen from Figure 46, the etched volume in the samples fabricated with the circular polarization and 400 nJ pulse energy after 6 h was ~ 11 % larger and with 600 nJ pulse energy ~ 9.3 % larger compared to fabrication with the linear polarization at the same conditions. This dependence shows that circular polarization can improve the etching time for the complex 3D microstructures. The presented results are in good agreement with the data reported in [157]. However, the circular polarization in combination with the contour scanning method is a new way how to improve the acid penetration into the complex structures. The processing with the pulse energies < 600 nJ generated the nanogratings inside the bulk material without microvoid formation [55] which can enhance the acid penetration into the modified material and, in this way, the higher etching rate was achieved. As was discussed before, the line scanning of the complex structures obstructed acid penetration into the modified region as nanograting orientation was optimised only for a single scan direction. To solve this problem, the contour scanning strategy was proposed. Figure 47 shows the difference between micro devices structures fabricated and etched with linear and contour scanning strategies.

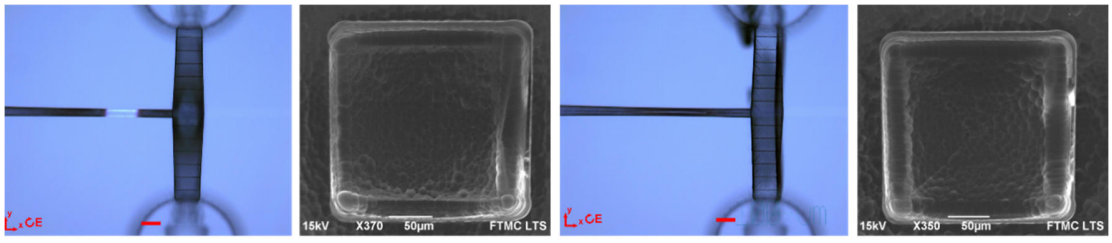

Figure 47 The micro device formed with: the line scanning strategy: a) optical microscope picture; b) SEM micrograph of enlarged etched area; and the contour scanning strategy: c) optical microscope picture; d) SEM micrograph of enlarged etched area. (dl = 2 µm, v = 1 mm/s, E = 400 nJ, circular polarization). The red bar indicates 100 µm.

The surface of the etched devices showed the semi-spherical shape of grain-like morphology. Depending on the laser processing energy, the grains were of a

different size. The orientation of the grains depended on the scanning directions as can be seen from SEM pictures in Figure 47b, d. During the experiment, the grain dimensions were measured after 13.5 h of etching and averaged in three different samples processed with 200 nJ, 400 nJ and 600 nJ with the linear polarization and in two samples processed with 400 nJ and 600 nJ using the circular polarization. Figure 48 shows the grains diameters (sizes) dependence on the fabrication pulse energy.

The devices fabricated with the lower pulse energy have grains of a smaller size. The grains that correspond to the fabrication with the circular polarization are larger than that get with the linear polarization. It follows from the results that the fabrication with a lower pulse energy is necessary to minimise roughness of the etched surface without any post processing of the etched devices. The pulse energy that corresponds to the type II modification threshold should be applied. Anyway, annealing of the samples is required to achieve a smooth surface for micro-optical devices fabrication [157].

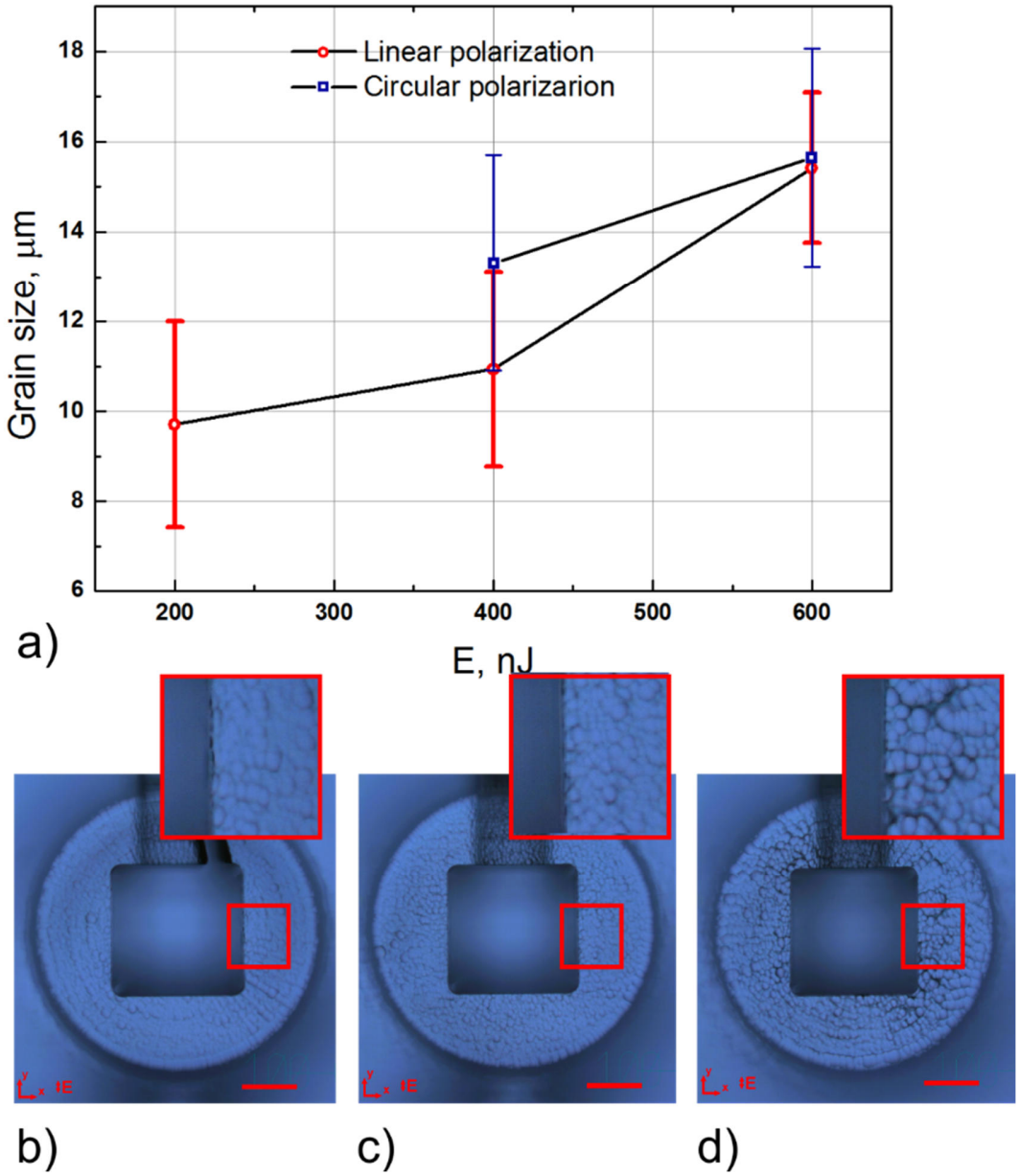

Figure 48 The grain size achieved after the 13.5 h etching depending on the fabrication energy (a); microstructures fabricated with linear polarization and contour scanning strategy: b) 200 nJ; c) 400 nJ; d) 600 nJ. The red bar indicates 100 µm. The insets show the enlarged grain structure.

To find out the morphology of the formed micro device cross-section, the sample was cleaved in the yz-plane, and the SEM analysis was performed (Figure 49). As can be seen from the figure, the sharp edges of the microstructure can be achieved. From the enlarged microchannel, it is evident, that almost perfect rectangular

~40x55 μm^2 cross-section was achieved which can be used for very low volume fluid pumping and transportation. The rough surface of the bottom of a microchannel demonstrates the scanning line orientation and shows that not all the modified material was removed.

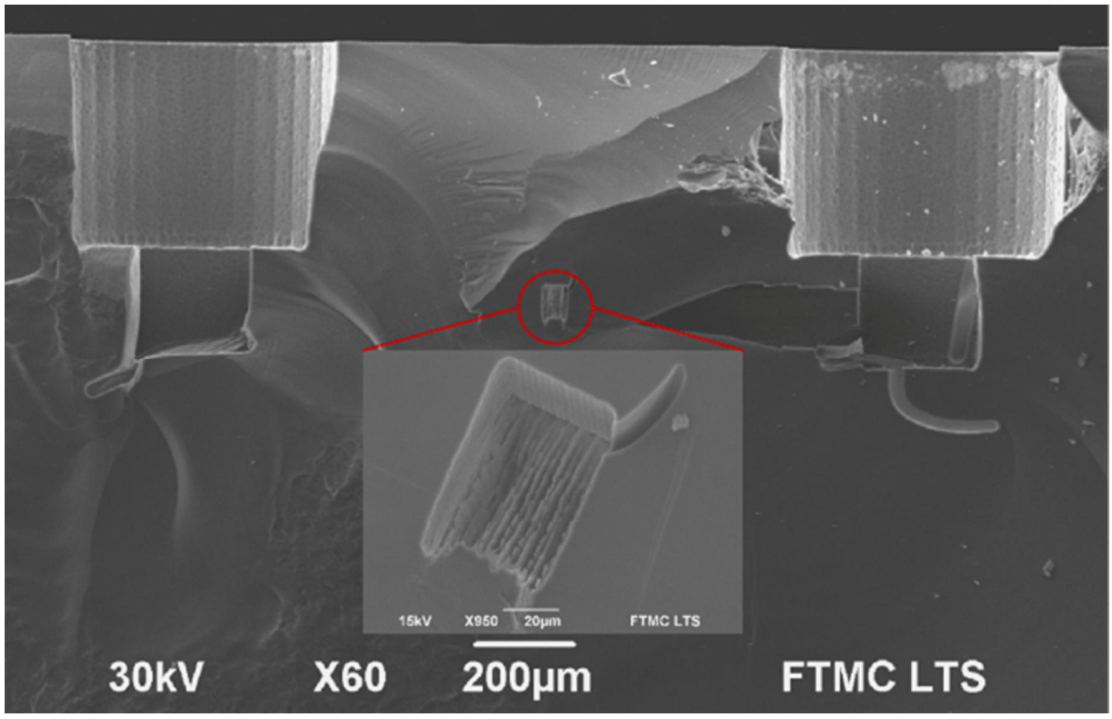

Figure 49 SEM micrograph of the cross-section of the micro device structure cleaved in the yz-plane. The cleaved sample was coated with 5 nm gold layer for SEM analysis. The inset show the enlarged etched microchannel with the residuals of the not etched material.

Finally, the complex structure with the embedded rotator that rotates on its axis was fabricated. The device was designed to compensate the taper angle of the microchannels arising from the etching selectivity limitations. The etched structure was filled with acetone, and the optical microscope pictures were snapped at different time moments during acetone evaporation and show rotation of the micro-rotor due to capillary forces (Figure 50). In the upper part of the microrotor, the terminals which could be used as an interconnection between micro to macro fluidic were formed.

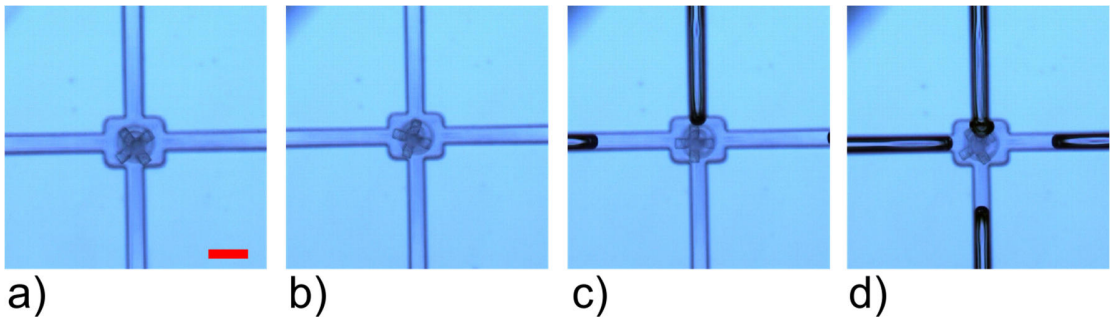

Figure 50 The micro-rotator embedded inside a fused silica and filled with acetone. a), b), c), d) – Acetone evaporation at different time moments. Dark lines show an empty channel. The red bar indicates 100 μm.

5.2 Passive Venturi micropump

In microfluidics, liquids are transported through microchannels, and one of the most important functional components are the micro-pumps and micro-mixers that can be used in active microfluidic devices [85, 158]. Using these components, the fully functional device can be miniaturised and embedded in a single chip. The syringe pumps are one of the most used devices for controlling the flow in microfluidic. The drawback of these pumps is that they are expensive and it is difficult to miniaturise them [159]. Miniaturisation is critical for the use of pumps in microfluidics. Therefore, there is a need for simple methods for creating flow in a microfluidic device. Many types of pumps have been developed for microfluidics that can be divided into mechanical pumps such as membrane pump [160, 161], rotary pump [162], and non-mechanical pumps: electroosmotic/electrophoretic pump [163]. The mechanical pumps have higher pumping velocity but also moving parts. Sensitivity to particle contamination in a fluid makes it difficult to use them in microfluidics as may result in a short lifetime and low reliability. Fabrication of non-mechanical pumps is simpler but small pumping velocity and charged fluid requirement limits their application.

In this section, we demonstrate the novel micro-pump device based on the Venturi tube (Figure 51) fabricated in fused silica by the FLICE technique. The Venturi micro pump is easy to miniaturisation and has no mechanical moving parts,

and that simplifies the fabrication. It is shown the ability of fluid pumping and mixing in a single device that can be attractive in various microfluidic fields. A preliminary study was performed to measure the required negative pressure for suction.

5.2.1 *Design, working principle, and fluid flow simulation*

The Venturi tube [164] produces pressure drop without moving parts in the vena contracta region (the narrowest channel part) and consists of a converging and diverging channels with an additional pumping channel. The liquid enters the device with a cross-section area S_{in}, pressure P_{in} and velocity v_{in}. According to the fluid continuity, the volumetric flow rate at the vena contracta should be maintained constant that means that fluid velocity in the throat will be faster and that can be derived from Bernoulli principle and continuity equation:

$$P_{in} - P_t = \frac{\rho}{2}(v_t^2 - v_{in}^2) = \frac{\rho}{2} v_{in}^2 \left(\frac{S_{in}^2}{S_t^2} - 1 \right). \tag{5.1}$$

where P_{in}, P_t are inlet and throat pressures, ρ is density, v_{in}, v_t are inlet and throat velocities, and S_{in}, S_t are the channel cross-section areas.

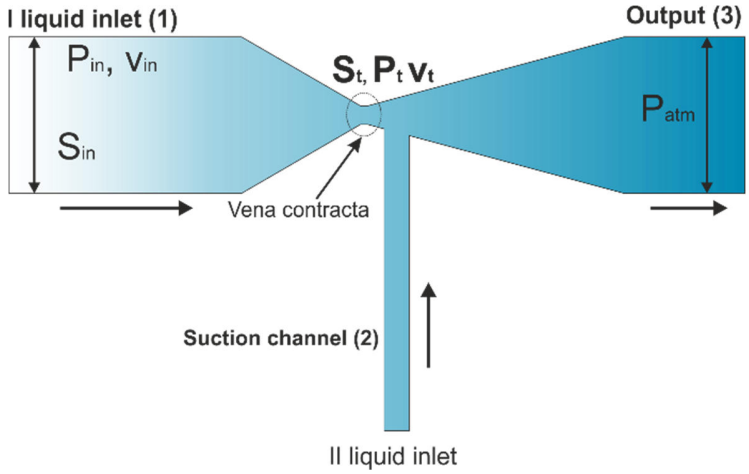

Figure 51 Schematic drawing of the Venturi-based micro-pump. The outlet is open to the atmosphere.

The accelerated liquid in the vena contracta region creates a pressure drop which should be compensated by the negative pressure, and a suction flow from inlet II appears. The design of the micro-pump device was adjusted to maximise the negative pressure. The Comsol Multiphysics software was used to optimise the micropump design and to find the threshold velocity to initiate the suction. The Navier-Stokes equation for the laminar flow was solved:

$$\rho\left(\frac{\partial u}{\partial t} + u \cdot \nabla u\right) = \left[-\nabla p + \mu \nabla^2 u\right] + F \qquad (5.2)$$

where ρ is the liquid density, $\boldsymbol{v}$ is the velocity vector, p is the pressure, μ is the dynamic viscosity and F is the gravity force. The main assumptions that were made during the modelling were: no-slip boundary condition and steady-state laminar flow condition. The simulation results are shown in Figure 52. As a fluid used for micropump characterization was water, Table 1 shows the main water parameters used in the simulation.

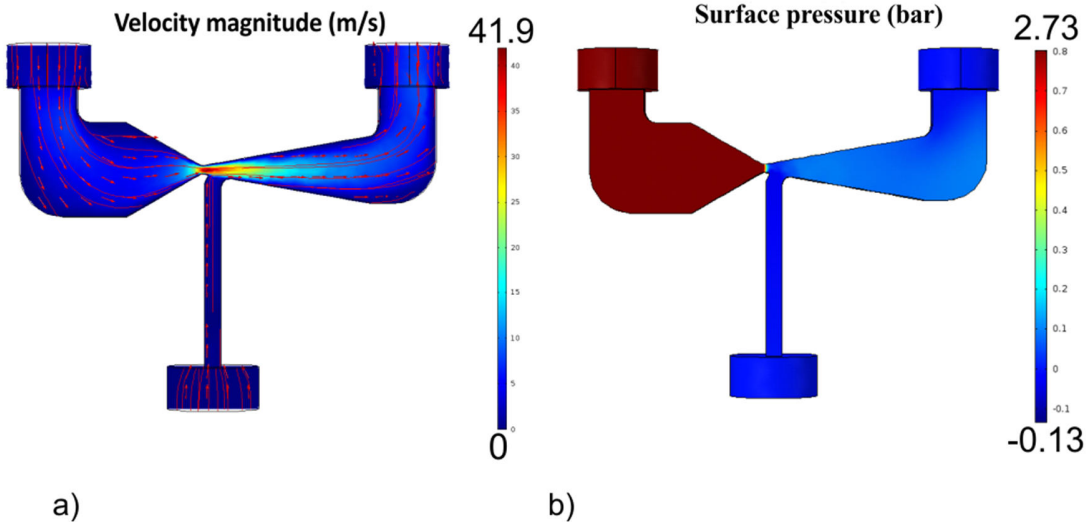

Figure 52 The velocity distribution (a) and pressure field (b) when the inlet water velocity is 1 m/s. The negative pressure in the vena contracta is -0.05 bar.

Table 1 The fluid parameters used in the simulation.

Parameter	*Value*	*Unit*
Density	1000	**kg/m^3**
Viscosity	0.001	**Pa·s**
Diffusion coefficient	2.99e-9	**m^2/s**
Inlet fluid velocity	0.1-2	**m/s**
Concentration	**1**	**mol/mm^3**

5.2.2 *Simulation of mixing*

The Fick's law can be used to describe the diffusive transport. At the macroscopic level, systems usually mix fluids using mechanical actuators or turbulent 3D flow. At the micro-scale level, however, neither of these approaches are practical or even possible. Inside the mixer, the following convection-diffusion equation describes the concentration of the dissolved substances in a fluid:

$$\frac{\partial c}{\partial t} + \nabla \cdot (-D \nabla c) = R - u \cdot \nabla c \qquad (5.3)$$

where c is the concentration, D is the diffusion coefficient, and R is the reaction rate. In this model, $D = 2.99 \cdot 10^{-9}$ m^2/s and $R = 0$, because the concentration is not affected by any reaction. The mixing results when the inlet concentration was 1 mol/mm^3 and the concentration in the suction channel was 0 mol/mm^3 and vice versa are shown in Figure 53.

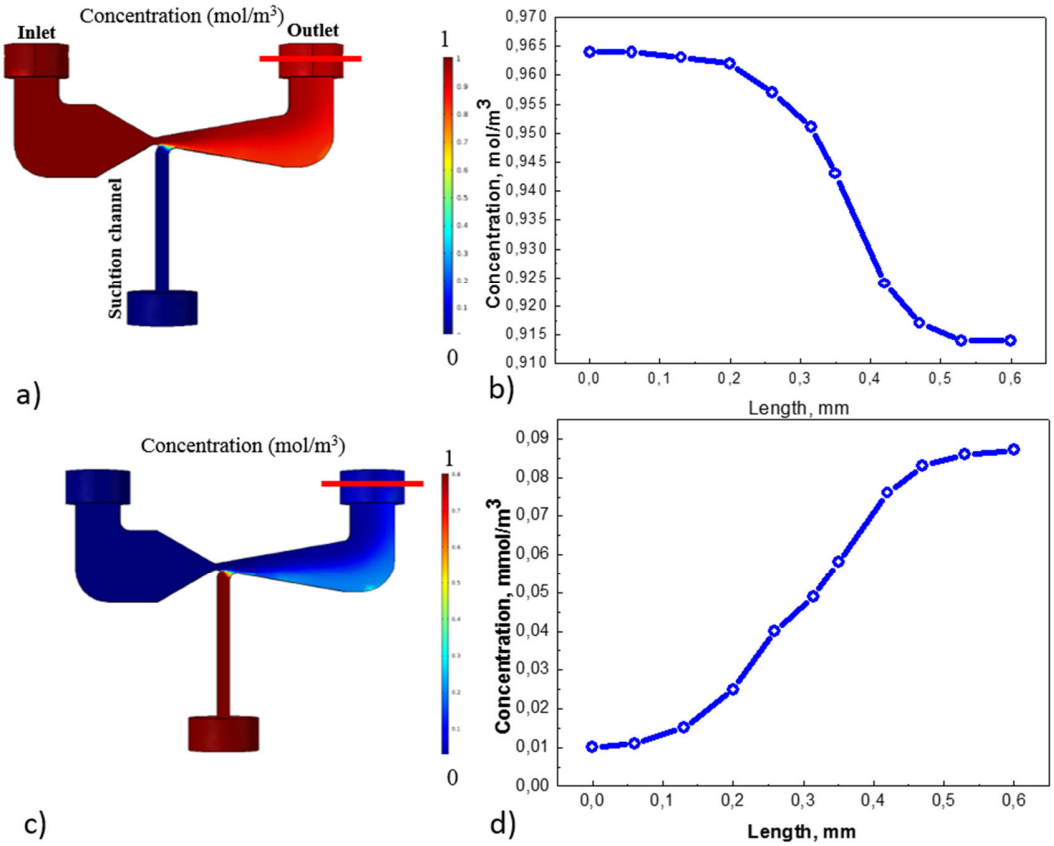

Figure 53 The ink concentration distribution in micro-pump device after 1 s: (a) Ink concentration at the inlet is 1 mol/m^3 and at suction channel ink concentration is 0 mol/m^3; (b) Ink concentration distribution at the cross section of the outlet microchannel (at indicated red line); (c) Ink concentration at the inlet is 0 mol/m^3 and at suction channel ink concentration is 1 mol/m^3; (d) Ink concentration distribution at the cross-section of the outlet microchannel (indicated red line).

According to the simulation results, it is evident that the concentration distribution at the output of the micropump is not uniform. The difference between minimal and maximal concentration is ~ 10 %. In the case, when 1 mol/mm^3 concentration of ink was at the inlet (Figure 53a), the concentration gradient at the outlet was positive and opposite gradient value when the concentration of 1 mol/mm^3 went from the suction channel (Figure 53c).

5.2.3 *Fabrication of the micropump device*

The micro-suction device was fabricated by the direct laser writing technique. with 500 kHz repetition rate and 400 nJ pulse energy. The beam was focused by the

50x (NA = 0.55) objective at a depth of ~ 550 µm below the sample surface. The sample was moved perpendicularly to the beam propagation direction at a speed of ~ 3 mm/s. The 3D micro-pump device was sliced to virtual vertical planes, and each plane was fabricated by the contour scanning method [165]. The linear polarization was set perpendicular to the X-axis direction. The modified sample was immersed in diluted 15 % HF acid for ~ 15 hours subsequent etching at 30 ºC temperature without ultrasonic batch. Fabricated micro-suction device possessed the micro-channels with a rectangular cross section. The inlet cross-section was ~ 670x150 µm^2; the vena contracta cross section was ~ 63x150 µm^2, and the outlet cross section was ~ 455x150 µm^2. The cross section of the suction channel was ~ 122x150 µm^2. During the experiments, a few designs of micropumps were fabricated (Figure 54) to optimize the device geometry and the size of the vena contracta. The micropump of the first design was fabricated without the simulation approach and exhibited no suction effect; the second and third design versions were optimised during the simulation.

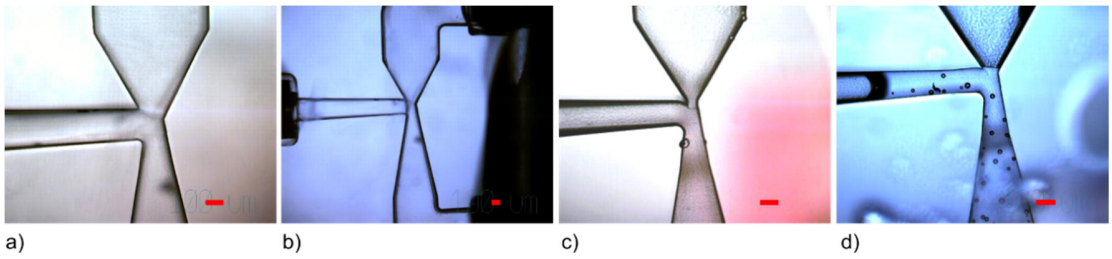

Figure 54 The micropump devices fabricated and etched in fused silica. (a) The second design approach with the ~ 130 µm wide vena contracta; (b) the ~ 100 µm wide vena contracta and the ~ 170 µm wide suction channel (c) the third design approach with the ~ 62 µm wide vena contracta and the 122 µm wide suction channel; (d) the ~ 87 µm wide vena contracta. The red bar indicates 100 µm.

The maximum suction effect was achieved when the vena contracta region was the narrowest. It is evident because the fluid speed was highest in the narrower channel. At the input and output part of the microchannel, the wider channels with a diameter of ~ 650 µm were fabricated as connectors from micro to macro. The sliced syringe needles were glued to the interconnectors with UV glue. Then the rubber hoses were

connected and glued to another needle side. The micro-pump device is shown in Figure 55a. The inlet of the prepared device was connected to the micro diaphragm liquid pump (KNF N10) with the controlled flow rate. The suction pressure was measured with the vacuum sensor (SMC ZSE 30). The measured and simulated dependence of the suction velocity on the input flow velocity is shown in Figure 55b.

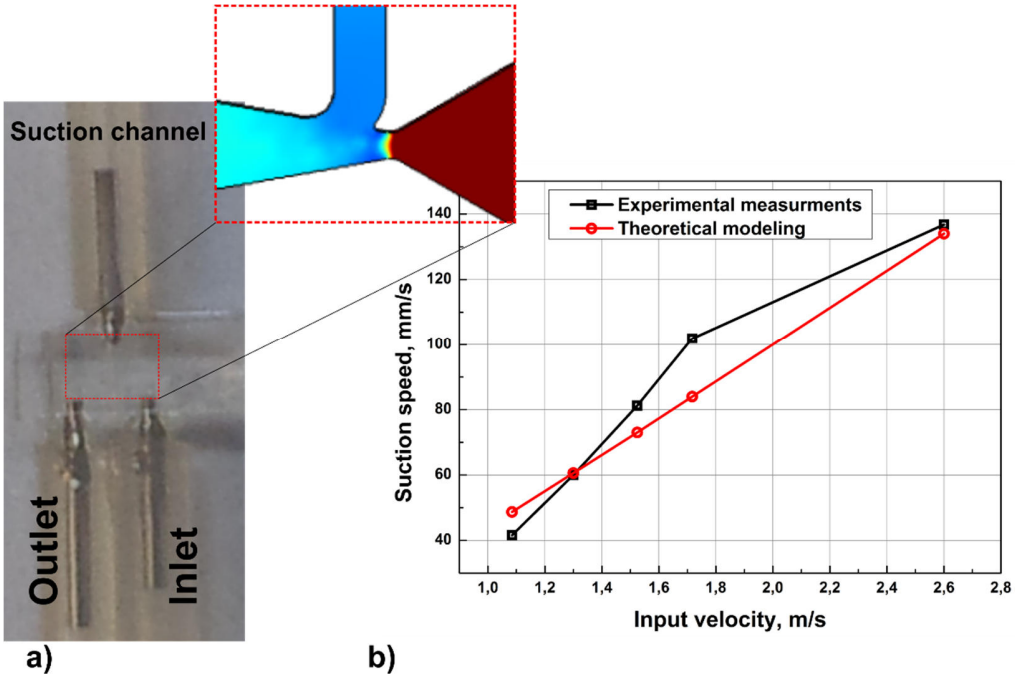

Figure 55 The fabricated micropump device (a) and the suction velocity dependence on the inlet fluid velocity (b).

The suction flow rate was measured by immersing the suction hose into the painted water cruet of a 2 ml volume. The suction time for 1 ml was measured, and according to this, the suction flow rate dependence on the inlet fluid velocity was estimated. The threshold inlet fluid velocity at which the fluid suction started in the suction channel was ~ 0.05 m/s for the micropump with the narrowest vena contracta (~62 µm). When the vena contracta size was increased, the threshold velocity increased as well. For the vena contracta of ~ 100 µm in size, it was ~ 0.4 m/s. The captured picture of the working micropump is presented in Figure 56.

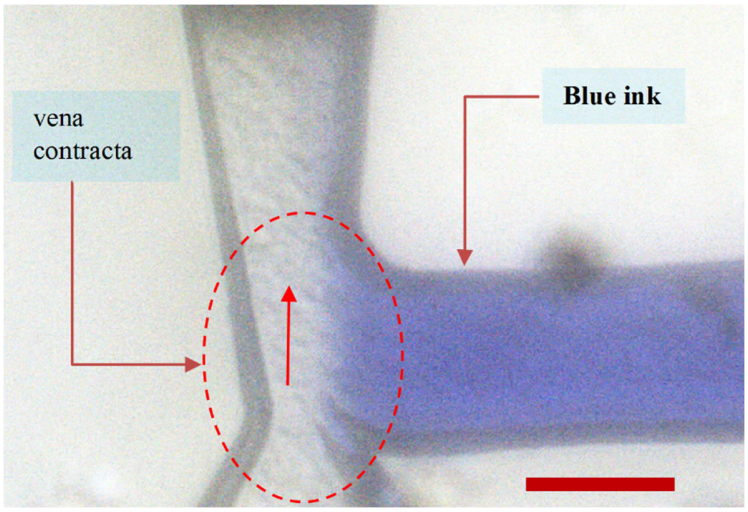

Figure 56 Image of the working micropump device in the vena contracta region captured with a CCD camera. The diluted blue ink was sucked in the suction channel and mixed with water. The speed of the blue ink is ~ 110 mm/s. The red bar indicates 100 μm.

In conclusion, the flow dynamics inside microchannels was investigated in order to achieve the suction effect in the Venturi type micropump. Depending on the used the input flow speed, the liquid injection or pumping can be achieved. The simulations showed that the narrowest vena contracta zone should be fabricated to get the best suction results. Experimentally, the ~ 60 μm width of the vena contracta zone was demonstrated with the minimal inlet fluid speed threshold of ~ 0.05 mm/s to initiate the pumping conditions. The pumping with ~ 110 mm/s velocity was achieved when the inlet fluid velocity was ~ 2 m/s. When the both inlets of the designed micro-pump were connected to liquids with a different concentration of dyes, the micropump acted as a micromixer.

5.3 Microfluidic device for ellipsometric biosensor application

In this section, the internal-to-external microfluidic device is presented. The micro-channels were prepared with the direct laser writing technique using different scanning methods [165]. To remove the modified material, a sample was immersed in diluted 10 % concentration HF acid.

Microchannels were designed to act as flow cells [166] in the imaging ellipsometric surface plasmon resonance (iSPR) setup to study the real-time kinetics of biological materials (proteins or DNA). Most of the current iSPR devices [167–169] measure the data from a single channel that makes the measurement process time consuming and expensive. Typically, one sensor chip is used for a single measurement only and for the next measurement the new sensor chip should be used. The goal of this study was to prepare the microfluidic device in fused silica that allows characterising the adsorption kinetics of biological materials by the iSPR method. A set of parallel independent microchannels were inscribed, and each of them was connected to the pump to circulate the protein solution during the measurement preserving a constant flow rate. This microchannel configuration involved parallelization of independent measurements of adsorption kinetics thus allowing to perform several independent experiments on the same sensor chip by shifting the microchannel position.

5.3.1 *Setup for Imaging surface plasmon resonance*

Imaging surface plasmon resonance (iSPR) experiments were performed in Kretschmann configuration [170] with imaging null-ellipsometer (Nanofilm_Ep3se, Accurion GmbH). Measurements were carried out with the 658 nm wavelength laser light at the 70.2 ° angle of incidence. Gold coated BK7 glass sensor chips (Biacore), and 60 BK7 glass prism were used. EP4 Model data analysis software was used for thickness modelling.

For all biosensor experiments and buffer preparation, the ultrapure water was used, taken directly from Synergy UV water purification system (Merck Millipore). Before the use, the sensor chips were cleaned with SC-1 solution, a mixture of ultrapure water, 30 % hydrogen peroxide (Carl Roth GmbH), and 25 % Ammonia solution (Carl Roth GmbH) in a ratio of 5:1:1, respectively, at 85 °C for 7 min., two times, followed by excessive rinsing in ultrapure water and drying with a nitrogen gas stream.

The self-assembled monolayer was formed by incubating the SC-1 cleaned sensor chip overnight in a solution of thiols in ethanol (Sigma-Aldrich), containing 8 μM concentration of biotin functional group containing thiol (HS-C_{11}-EG_3-biotin, ProChimia) and 32 μM concentration of protein adsorption resistant EG_3-OH group terminated thiol (HS-C_{11}-EG_3-OH, ProChimia). After incubation, the sensor chips were rinsed and sonicated in ethanol for 3 min. twice, sonicated in ultrapure water and dried with a nitrogen gas stream.

5.3.2 *Fabrication and investigation of the external-to-internal microchannels*

To get the internal-to-external microchannel, a part of the modified zone of fused silica should be near the sample surface, and the top part of the channel appears as surface damage. The design of such microfluidic channel is presented in Figure 57. The 3D model of the microchannel was imported to the fabrication program (SCA, Altechna R&D) and sliced into planes with the distance between them equal to 5 μm. Each plane was hatched by lines, and the scanning direction of lines was perpendicular to the laser beam polarization. The scanning speed and laser pulse energy were as follows: 4.5 mm/s and 400 nJ. For the first etching approach, the modified sample was submerged into diluted 10 % concentration HF acid for 12 hours. The improvement of the etching time was achieved by immersing a jar with the acid into heated to 40 °C water in an ultrasonic bath. In this case, depending on the etching conditions, the etching rate was increased from 5 to 10 times.

A large area of the modified zone in the external part of a microchannel is exposed to the etching solution (along the all external part of the microchannel). In this case, etching takes place in the perpendicular direction to the microchannel direction. However, in the internal part of the microchannel, only a cross-section of the microchannel is open for the acid, and the etching goes along the embedded modified zone. Therefore, the external part of the microchannel is formed much faster than the internal part. According to our investigations, the maximum achieved etching rate in 10 % HF for fused silica modified by 500 kHz and 400 nJ pulses was

~ 1000 µm/h while for unmodified fused silica ~ 15 µm/h (see below). This gives the etching selectivity of ~70 times. To fabricate good-quality microchannels, the etching selectivity should be taken into account. The modification depth for external microchannel was ~ 40 µm. The modification width of the microchannel was 50 µm for all microchannel lengths. Taking into account the 1000 µm/h etching rate of the laser modified zone, the estimated etching time for the external part of the microchannel should be only ~ 3 min. and the rest of time, the width of the external microchannel increased with the 15 µm/h rate (Figure 59f).

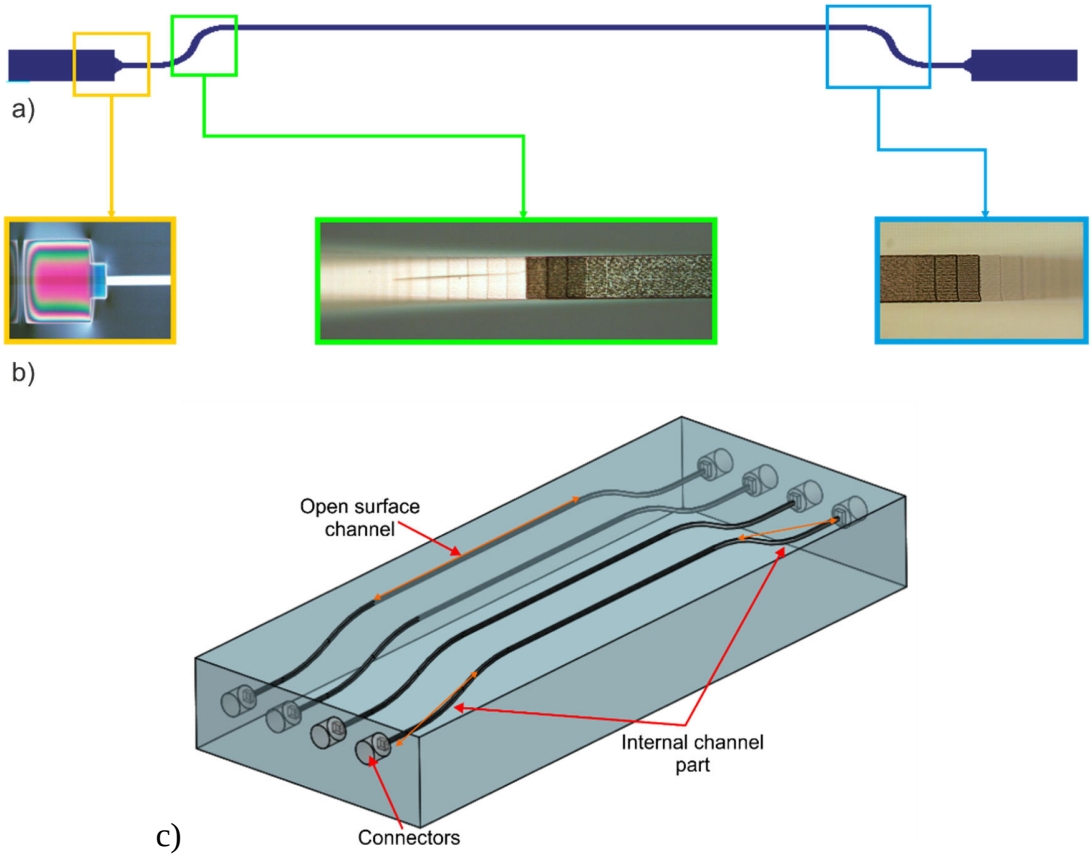

Figure 57 Design of the microfluidic external-internal microchannel (a); the optical microscope pictures from the top of the laser-induced modifications in fused silica (b); and design of the setup with internal-to-external microchannels (c).

The depth of the external part of microchannel after 1 hour of etching remained almost unchanged. The length of the embedded part of the microchannel varied from 2.5 to 3.5 mm, and the etching of this part took place from both sides (from

the transition between the external and embedded part and the connector side). That part of the channel should be fully etched after ~75 min. – 105 min. This estimation shows that design of the external-to-internal microchannels should be with minimised length of the embedded microchannel length to save the external part of the microchannel from degradation.

The design of microchannels plays a significant role for the etching time and quality of the external microchannel part. The internal part of the microchannel was used to prepare the interconnection with capillary that directs an analyte from an external pump to the microchannel. A few designs of microchannels were prepared. The first design was used only to check the functionality of the single channel measurements (Figure 57a). The second design was developed with close to each other placed microchannels to allow parallel measurements (Figure 58a). The latest design was developed with a close distance of adjacent microchannels and the minimised length of the embedded part of the microchannel (Figure 58b). As the internal part of the microchannel is embedded in fused silica, its vertical dimensions should be scaled by the refractive index of fused silica (n ~ 1.4615 at 515 nm) to get the correct shape of the microchannel due to the light refraction in transparent materials.

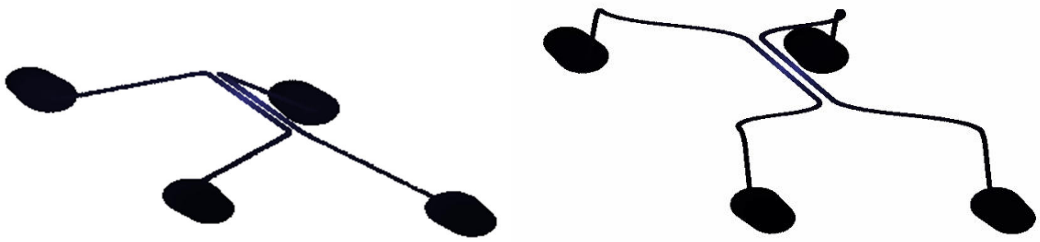

a) b)

Figure 58 Two optimised designs of the internal-to-external microchannel. The vertical dimensions are scaled by the refractive index of fused silica.

According to the described design, the samples were fabricated and etched in 10 % HF acid in the ultrasonic bath for 2 hours. To get the microchannels with

different surface roughness, each microchannel was fabricated with various fabrication parameters. The fabricated microchannels with different design approaches are shown in Figure 59. Influence of the processing parameters to the surface roughness is described in the next section.

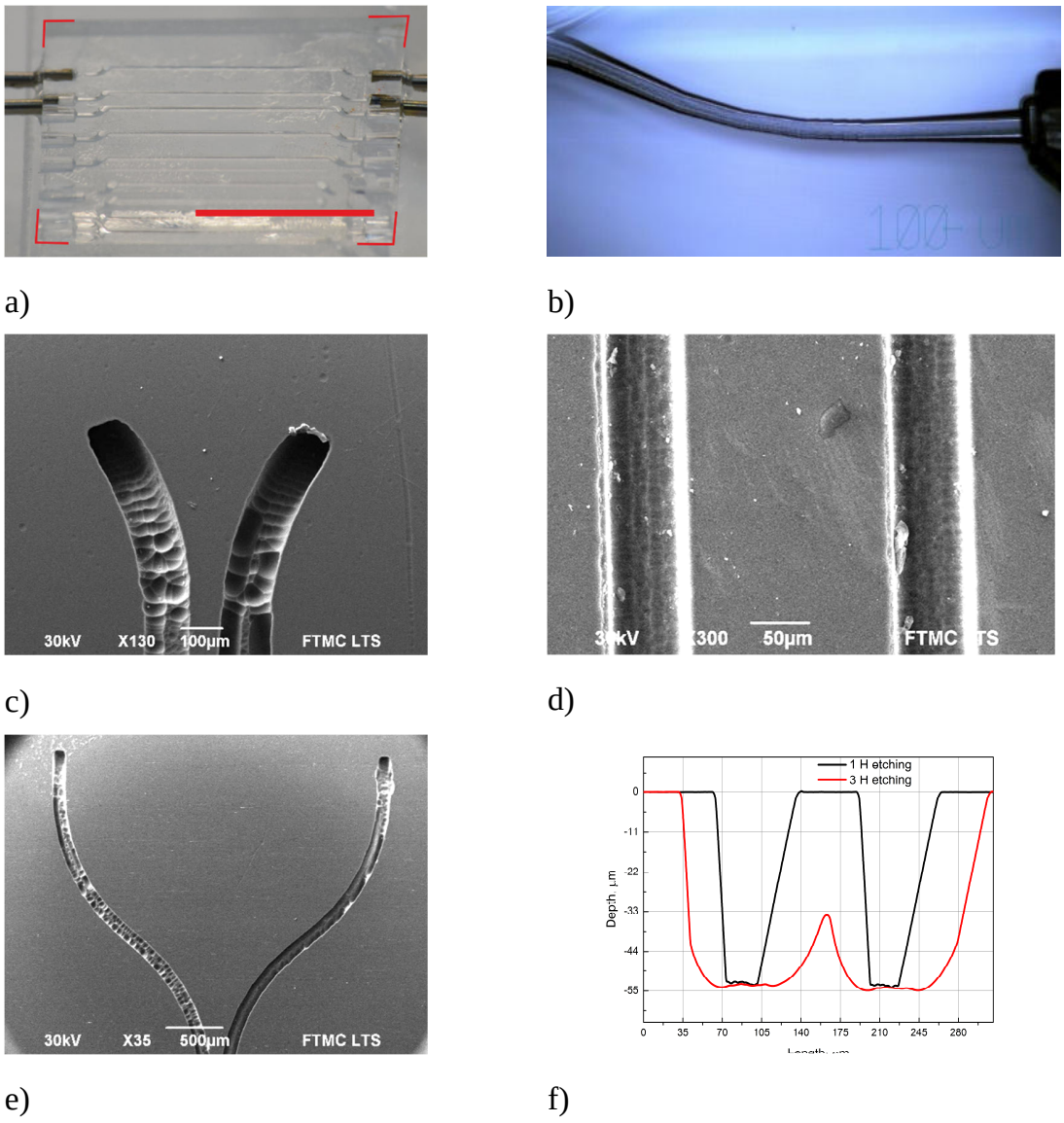

Figure 59 The pictures of fabricated microchannels with different design approaches: (a) full microchannel set with integrated connection tubes prepared for testing. The red scale bar indicates 10 mm; (b) Side view of the embedded microchannel part etched for 12 hours in 10 % HF acid; (c) SEM picture of the transition from the external to internal microchannel with the second design approach etched in HF acid 2 hours; (d) The top view of microchannels of the design approach from Figure 58a; (e) SEM picture of the transition from the external-to-internal microchannel of the design approach from Figure 58b etched in HF acid for 2 hours; (f) The depth profile of microchannels in Figure 59d, after different etching time.

The fabrication parameters of microchannels shown in Figure 59c are 300 nJ, 10 mm/s, dy = 3 μm and dz = 5 μm for the left channel in Figure 59c and 200 nJ, 5 mm/s, dy = 1.5 μm and dz = 5 μm for the right microchannel. In Figure 59e, the fabrication parameters are 300 nJ, 5 mm/s, dy – 3 μm and dz – 3 μm for the left channel and 300 nJ, 10 mm/s, dy = 3 μm and dz = 5 μm for the right microchannel.

From the depth profile of microchannels in Figure 58a, the etching rate of non-modified fused silica can be estimated, and it was ~ 15 μm/h. The volume of the etched microchannel increased, however, the depth remained almost unchanged because the measurements of the depth were done in respect to sample surface that was also etched with the same ~ 15 μm/h etching rate.

5.3.3 *Surface roughness estimation of the external channel part*

During the ellipsometric measurements, the solution of proteins flows through the external part of the microchannel, and the measurement results depended on the quality of the microchannel because of flow disturbance and light scattering from the channel walls. The surface roughness of the external microchannel was investigated. For that purpose, an array of external microchannels was fabricated varying the pulse energy (200 nJ-400 nJ) and scanning speed (2.5 mm/s – 20 mm/s). One channel was inscribed by a set of scans in the y-direction with the distance between scans – *dy* and in the z-direction with the distance between scans - *dz*. Five sets of the microchannel arrays with different *dy* and *dz* distances were fabricated. The last layer was focused on the sample surface to initiate the surface ablation. The processing parameters for each set are shown in Table 2.

Table 2 Processing parameters of the external channels.

Microchannel set no.	Laser pulse energy for one set, nJ	dy, um	dz, um	Translation speed for one set, mm/s
1	200 – 400	3	5	2.5-20
2		1.5	5	
3		5	5	
4		5	3	
5		5	7	

The fabricated external channels were immersed into diluted 10 % concentration HF acid in the ultrasonic bath and etched for 1 hour. After one hour, the sample was inspected by an optical microscope (Olympus), scanning electron microscope (JEOL JSM-6490LV) and stylus profiler (Bruker Dektak 150+) to measure the longitudinal surface roughness of the etched channels, and then placed for etching for one more hour. After 2 hours of etching, the sample was inspected by the same methods.

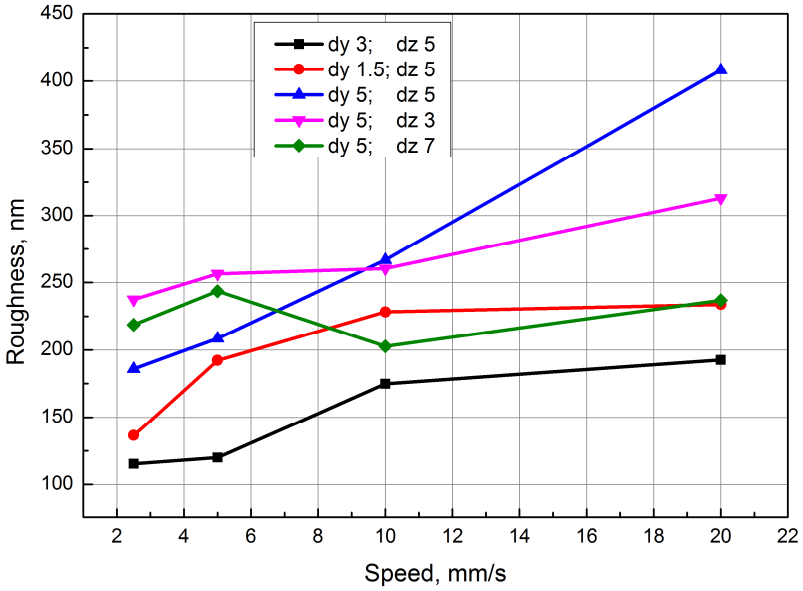

Figure 60 Dependence of longitudinal roughness of the external channel part on the scanning speed. The microchannel etching time in HF acid was 2 hours. The laser pulse energy and repetition rate were set as constant: 200 nJ and 500 kHz.

The surface roughness dependence on the scanning speed using the constant 200 nJ laser pulse energy is shown in Figure 60. The surface roughness decreased reducing the scanning speed. More pulses were delivered to a single point using the lower scanning speed at a constant pulse energy. Therefore, the overlap of adjacent modifications increased and larger exposure dose to a single point induced stronger modification of surrounding material. That led to the smaller grain size, and smaller surface roughness was achieved. The SEM pictures of the etched microchannel prepared using different processing energy are shown in Figure 61. The grain size increased by increasing the pulse energy that coincides with the results reported in the previous work [165].

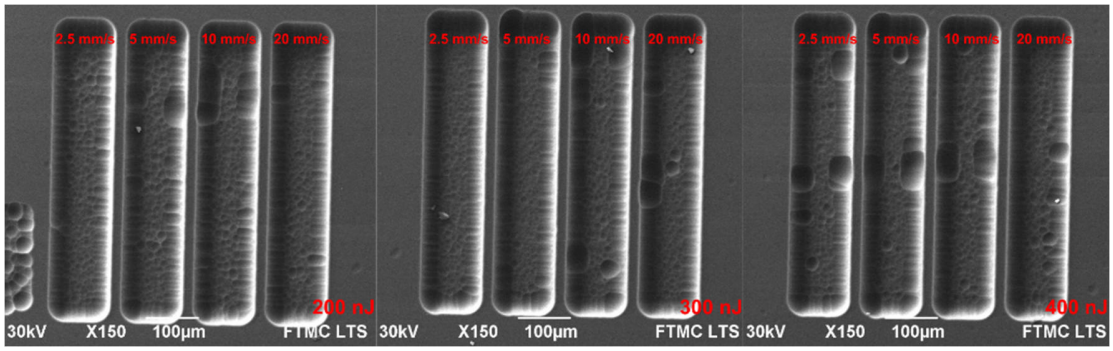

Figure 61 Images of external microchannels etched for 2 hours in 10 % HF acid.

5.3.4 *Investigation of the surface roughness of etched devices*

For many of optofluidic devices the channels roughness plays an important role, due to the light scattering and unwanted losses, therefore it was decided to investigate more detailed the channels roughness dependence on the different laser parameters and sample heating influence to the surface morphology. The experiment was prepared in the following way: the 4x4 fused silica surface modifications matrix was prepared where the scan speed was changed from 0.25 to 5 mm/s in the X-direction and the distance between adjacent modification lines was changed from 1 to 10 µm in the Y-direction. The 500 kHz repetition rate and 520 nm wavelength were applied. Four matrices were recorded, and the different

pulse energy from 100 nJ to 600 nJ was applied for each matrix. The samples etched for 32 min in 20 % HF acid are shown in Figure 62.

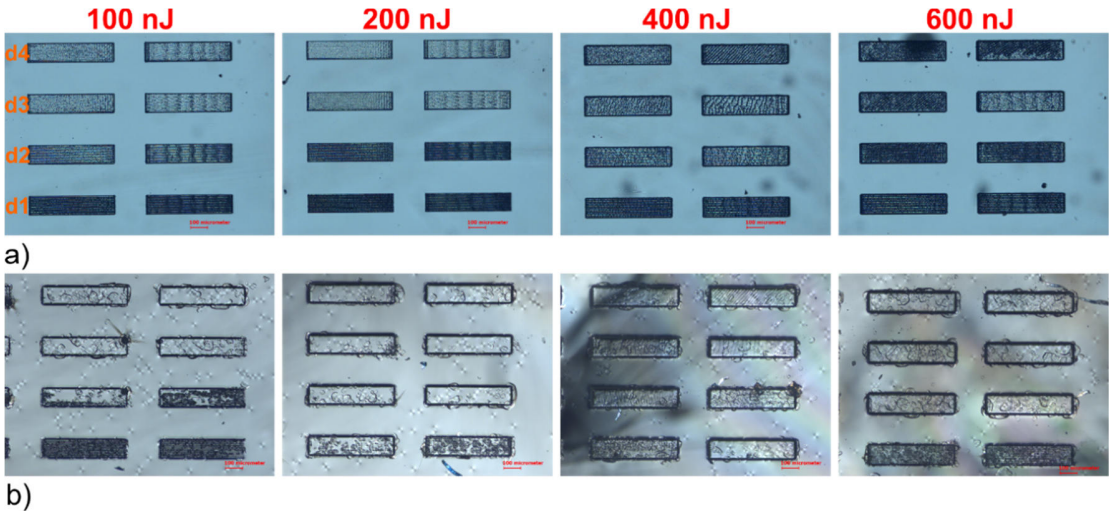

Figure 62 The surface channels etched in 20 % HF acid for 32 min (a) and after heating until 1210 °C with the 300 °C/h rate (b).

From the microscope pictures it can be noted that the annealing of the sample can smoothen the surface of the channels, however, small cracks appear during the heating. The small material parts were chipped and felt on the channel bottom and then melted. Such surface morphology is visible in the Figure 62b. This speculates that the heating rate was not optimal, and the process should be in further optimised to avoid the surface chipping.

The surface roughness of each channel was measured with the stylus profiler (Bruker Dektak 150+) in the X-direction along the scan direction and the Y-direction – perpendicular to the scan direction. The measured results are presented in Figure 63. The smallest achieved roughness (Ra ~ 75 nm) was for the 200 nJ pulse energy that was meanwhile the optimal energy for the nanograting formation. For pulse energies of 100 nJ and 200 nJ, the roughness was minimal for the 1 mm/s scan speed and increased in both directions for the higher speed. For pulse energies from 400 nJ to 600 nJ, the maximal surface roughness in the X-direction was for the 1 mm/s scan speed.

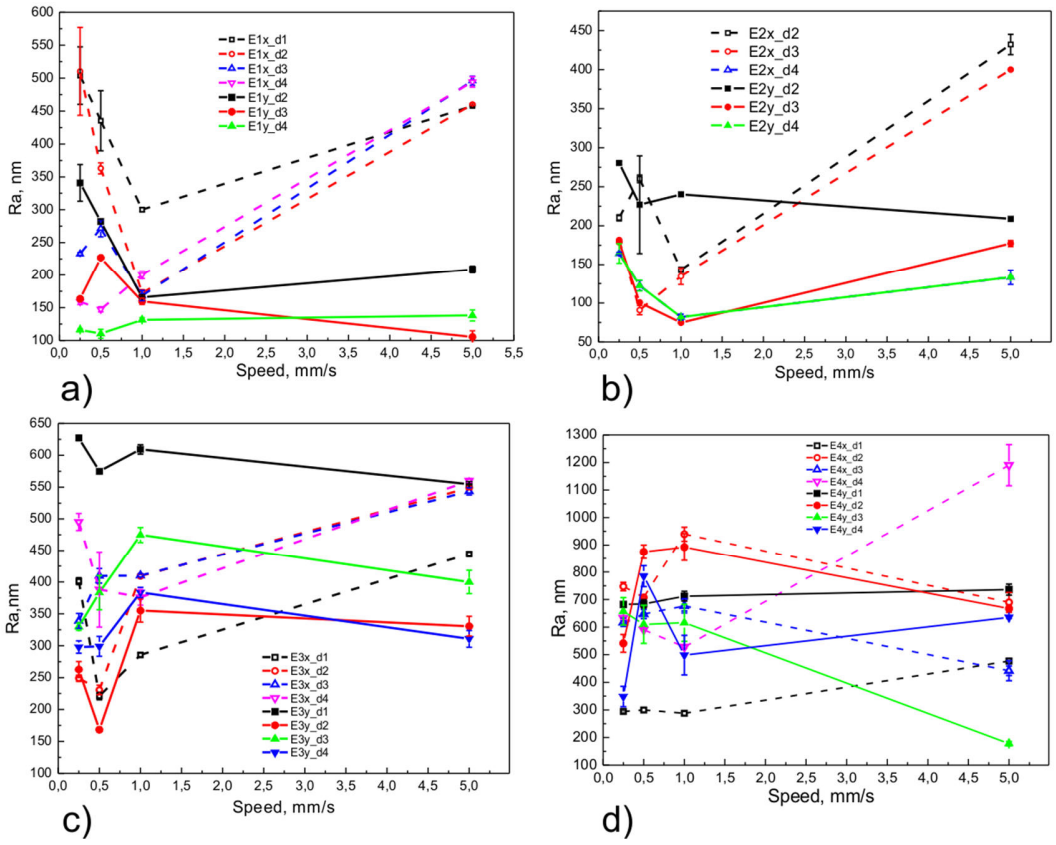

Figure 63 Dependence of the etched channels surface roughness on the scan speed for a) 100 nJ pulse energy; b) 200 nJ pulse energy; c) 400 nJ pulse energy; and d) 600 nJ pulse energy. The distance between adjacent lines was d1 – 10 µm, d2 - 5 µm; d3 - 2 µm; d4 = 1µm. Suffix X means roughness along the scan direction and Y – perpendicular to the scan direction.

The maximum surface roughness was achieved with 600 nJ pulse energy, and it was Ra ~ 950 nm. In optofluidics, the surface roughness of the microchannels should be smaller than the wavelength, and in most cases, for getting the valuable results, the roughness should be < λ/4 and even better. For inscribing with the 515 nm wavelength, this condition was satisfied for external channels fabricated with 200 nJ pulse energy and 1-2 µm distance between the modification lines. Unfortunately, in most cases, this pulse energy was not sufficient to achieve the maximum etching rate. Therefore it should be increased until 400 nJ, and then the minimal surface roughness was Ra~ 250 nm for 5 µm distance between the modified lines. This value was only 2 times smaller than the 515 nm wavelength and thus was not sufficient for optical applications consequently only the longer

wavelength can be used in the IR range. The surface morphology before heating and after the heating until the ~ 1200 °C temperature is shown Figure 64.

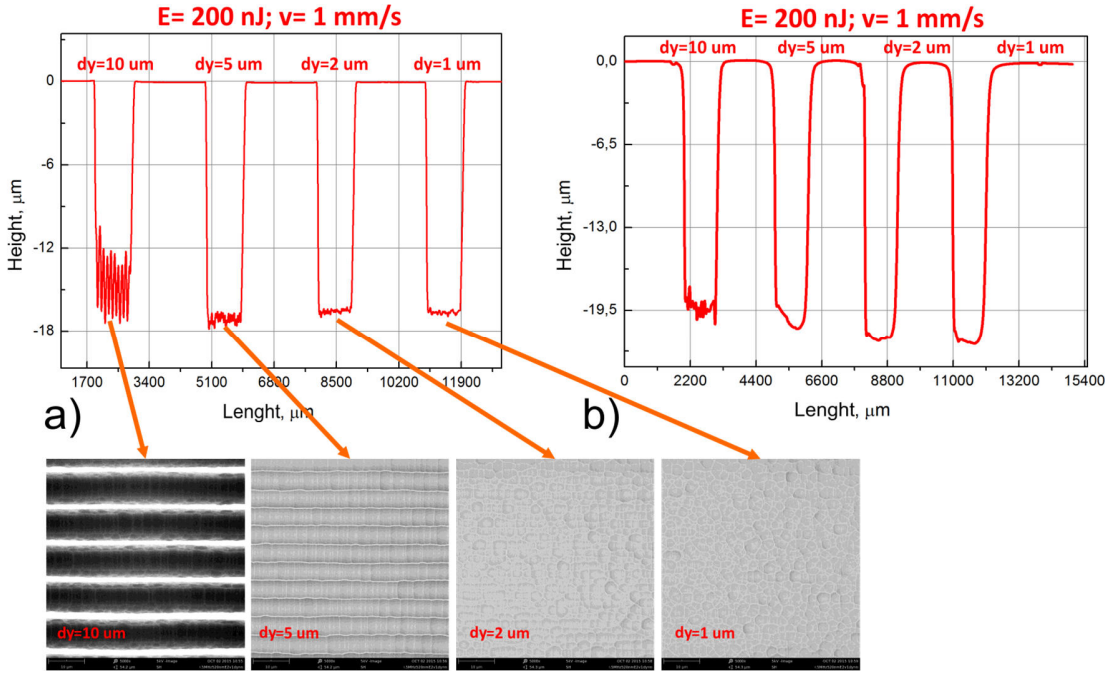

Figure 64 The surface profile and SEM pictures of the channel surface etched for 32 min in 20% HF acid (a) and surface profile of the same surface channels heated until 1210 °C temperature with the 300 °C/h heating rate (b). The scan speed was 1 mm/s and the pulse energy 200 nJ for the 520 nm wavelength at the 500 kHz repetition rate.

The surface roughness was minimised until the Ra~40 nm in this way, and the ratio of λ/12 can be achieved which is sufficient for the optical application.

5.3.5 *Assembling of the microfluidic device*

Microchannels were designed to act as flow cells [166] in the iSPR setup to study the real-time adsorption kinetics of biological materials (proteins). The microfluidic device was connected with the prepared sensor chip - glass substrate coated with a thin gold layer. The non-modified surface of the microfluidic device was also affected by HF acid. Therefore, the flatness was not sufficient to ensure hermetical sealing between the external part of the microchannel and the Au-coated sensor chip. To secure a reliable sealing, a thin PDMS interlayer with the thickness of

100 µm was added. The fluid to the sensor chip surface was delivered through slits in the PDMS interlayer with the size of a microchannel. The slits in PDMS were cut by the laser. After laser cutting, the PDMS interlayer was cleaned in ethanol and mounted on the top of the device with open microchannels. Then the glass surface was hermetically sealed with the PDMS layer. For the final step, a prism was placed on the sensor chip to obtain the Kretschmann configuration for the iSPR setup. The design of assembled iSPR setup is shown in Figure 65.

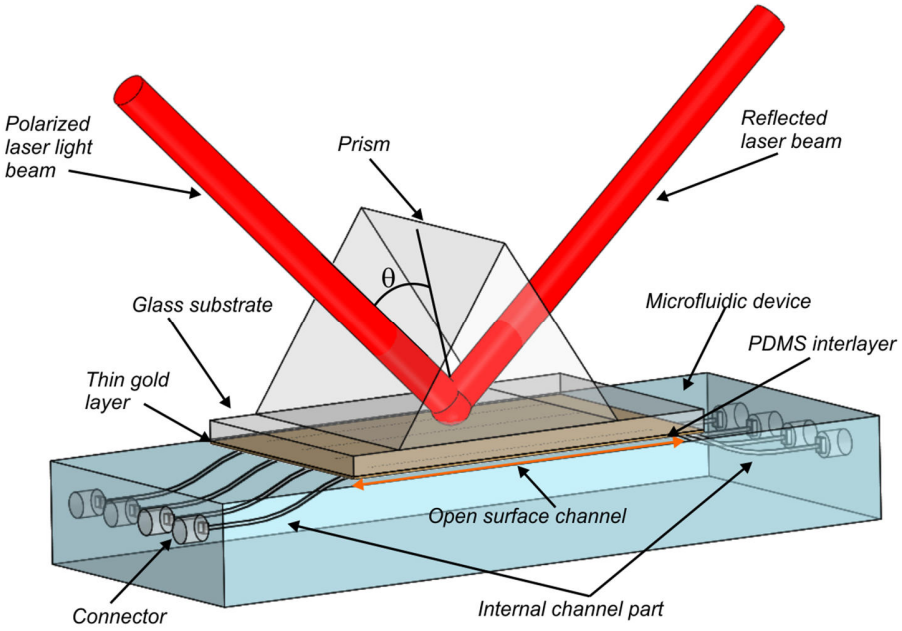

Figure 65 The design of iSPR setup with the integrated internal-to-external microfluidic device.

5.3.6 *Characterization of the microfluidic device*

To test the performance of the assembled microfluidic device, it was connected to the peristaltic pump with a constant flow rate which pumped the HEPES buffer (20 mM HEPES, 150 mM NaCl, pH 7.5) at 150 µl/min. flow rate from vial A. The fully-integrated and connected device was mounted into the ellipsometer for the specific protein adsorption kinetic measurement (Figure 66).

The specific and well-known biotin – streptavidin recognition reaction [166] was chosen to test the system performance. The sensor chips were modified with biotin functional group bearing a self-assembled monolayer.

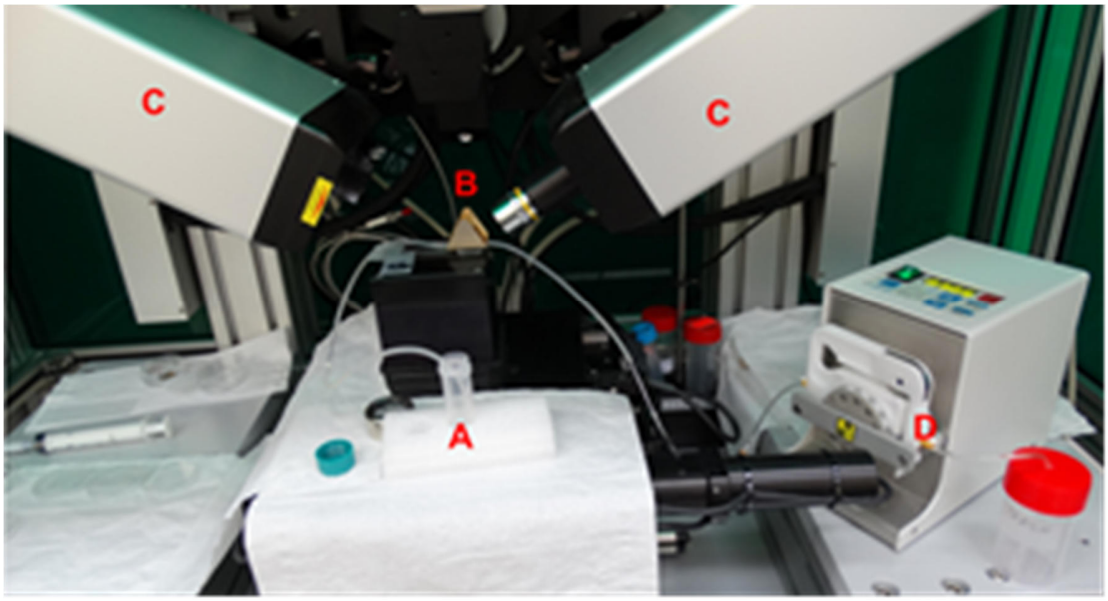

Figure 66 The fully integrated microfluidic device for ellipsometric measurements. A – vial with a buffer fluid and specific protein, B – the microfluidic device with the mounted prism, C – ellipsometer, D – fluid pump.

After rinsing with the buffer, the 1 mg/ml bovine serum albumin (BSA, Sigma-Aldrich) solution in HEPES was injected for 5 min. No protein adsorption was visible, what indicated that the sensor surface was sufficiently protein resistant (Figure 67). The second injection was the protein that should adsorb specifically on biotin groups – streptavidin. The 250 nM concentration streptavidin (Serva Electrophoresis GmbH) solution was injected in the buffer for 25 min. The specific adsorption was clearly visible. The thickness of the adsorbed streptavidin layer was 0.2-0.3 nm according to the ellipsometric model calculations. The break in the kinetics appeared because of the air bubble, trapped in the microchannel.

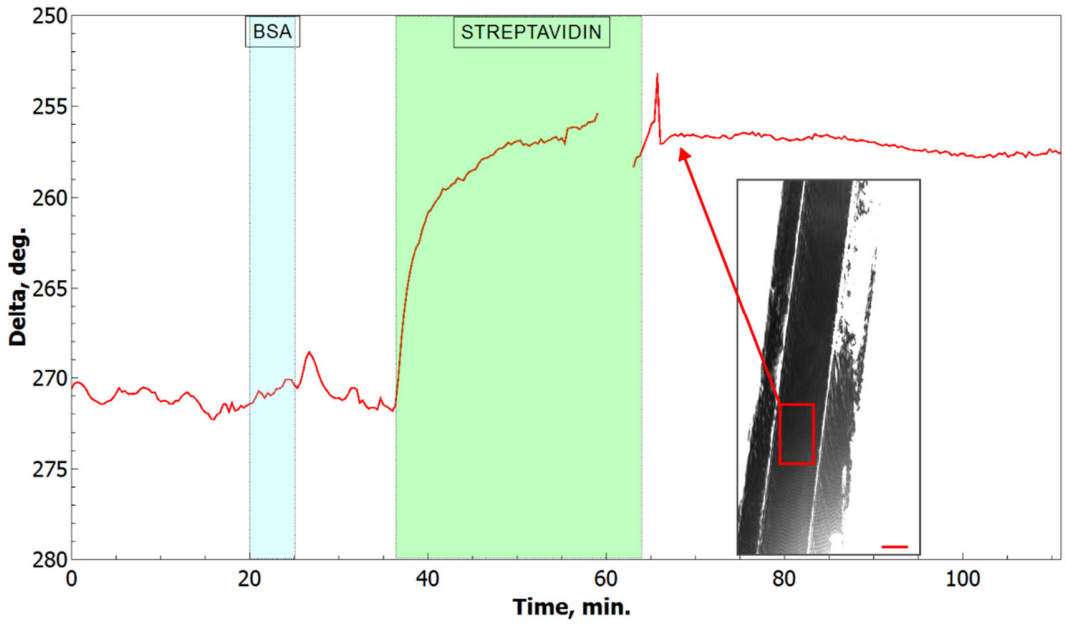

Figure 67 The specific protein adsorption kinetic measurement results achieved in the fabricated microfluidic device. Abbreviation on the graph: BSA – bovine serum albumin. Inset - the measurement zone in the microfluidic channel that is seen in the ellipsometric device. The red scale bar indicates 50 µm.

In conclusion, we have demonstrated the microfluidic device for ellipsometric applications with internal-to-external microchannels that served for measurement parallelization. We showed, that the protein adsorption kinetic can be properly measured by using our fabricated microfluidic device. The formed parallel microchannels allow the more efficient use of sensor chip and repeatability of experimental conditions. Due to decreased volumes of flow cells, much shorter solution mixing time was obtained, that made it possible to registration of the protein association kinetics at a constant its concentration.

5.4 Microfluidic lens design and fabrication

The microfluidic lenses fabricated inside the transparent materials are embedded devices without any adjustment requirements. They are able to make a direct focusing and imaging inside the lab-on-chip devices for characterization purposes in microfluidics. That lens as an example can be used for the selective plane illumination microscopy (SPIM) device fabrication [171]. The FLICE technique

was used to fabricate a complex shape of a micro lens to show the ability of collimation and focusing of the light coming from the laser-inscribed Y-waveguide.

5.4.1 *Design, fabrication and characterization of aspheric lens*

Usually, the microfluidic devices have limited dimensions. Therefore, the main task was to design and fabricate the aspherical lens with the focus of 1.5 mm. The flexibility of the focusing was designed by filling the hollow lens volume by a refractive index compensation fluid. The surface shape of the aspherical lens was estimated according to the Snell's law and the surface curvature radius formula:

$$r(\theta) = r_0 \frac{n_1 - n_2}{n_1 \cos\theta - n_2} \qquad (6.1)$$

where r_0 corresponds to the radius at 0° angle, n_1 – is the refractive index of the lens filled with the refractive index compensation fluid (n_1=1.73) and n_2 – is the refractive index of the surrounding material (fused silica, 1.45). The fabrication algorithm of the lens is presented in Figure 68a. Two interconnections from both sides of the lens were fabricated to connect the internal channels which direct the refractive index matching fluid into the lens structure.

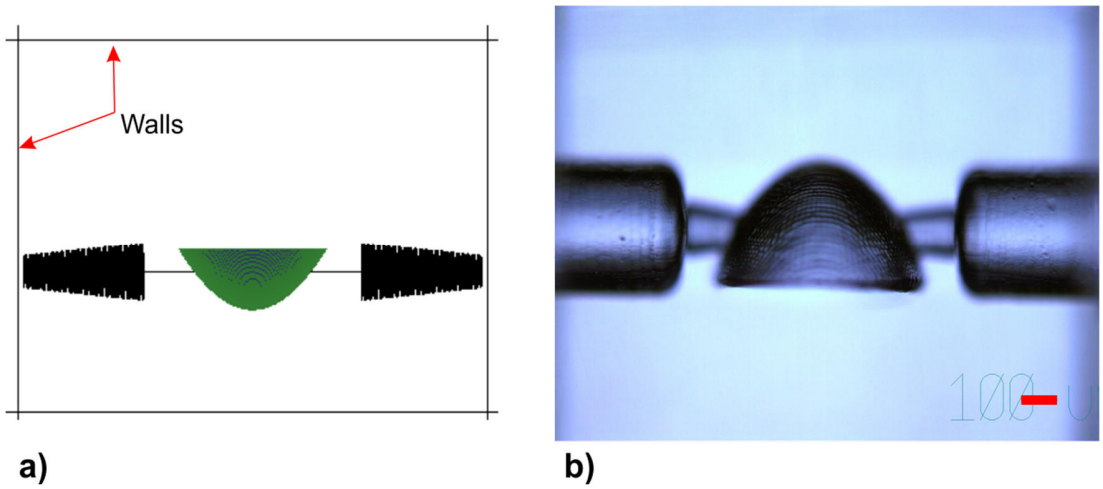

Figure 68 Microfluidic lens design with two sides interconnections a) and the lens structure etched in the 15 % HF for 4 hours. The red scale bar indicates 100 µm

The lens cavity was surrounded by the walls that created the shape of the whole structure. After the etching, two hoses were glued to the microfluidic structure with the UV glue and mounted on the characterization setup described in Section 2.7. The focusing characteristics of the microfluidic lens are presented in Figure 69.

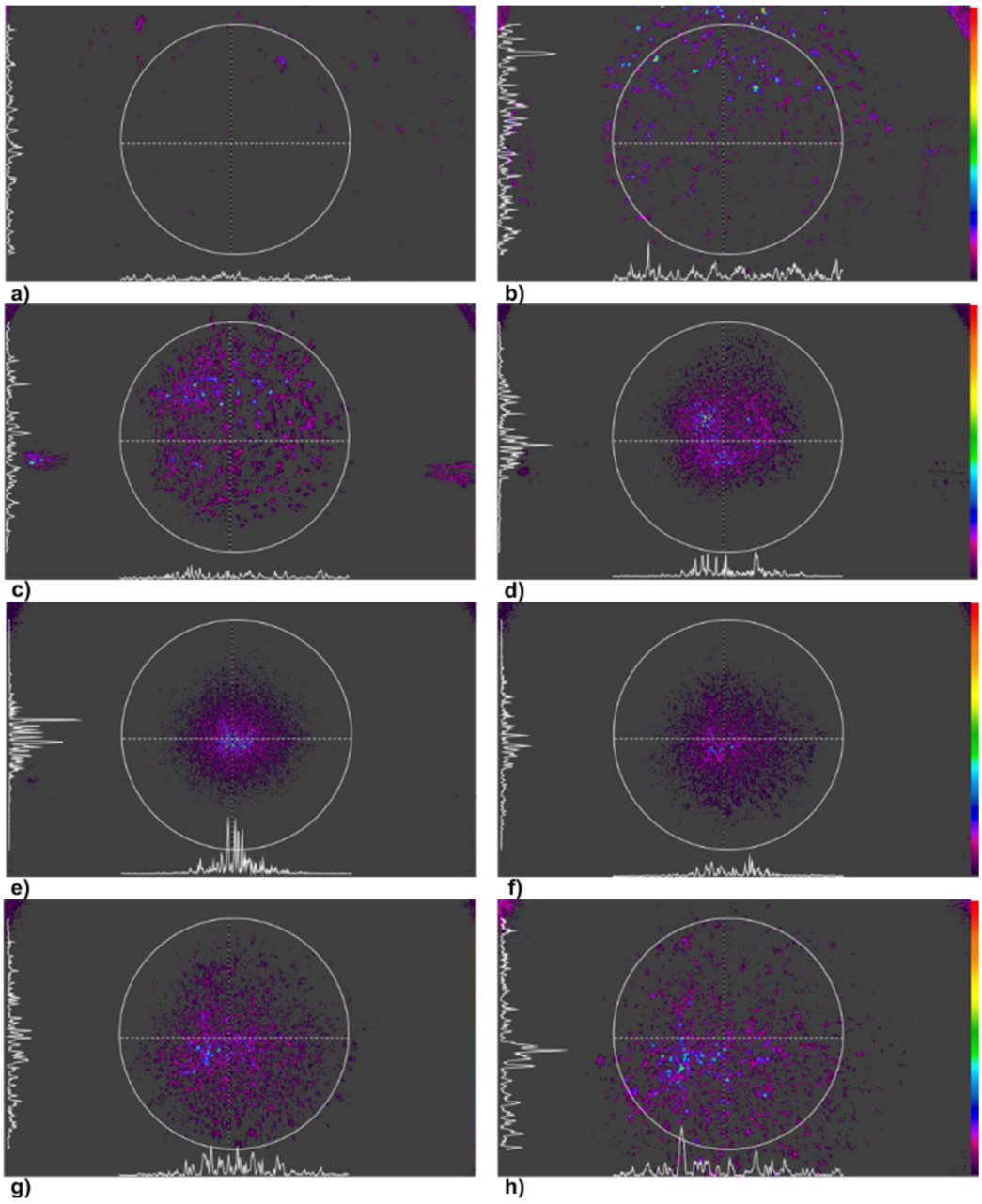

Figure 69 The focusing characteristics of the f=1.5 mm aspheric lens. The pictures shows the intensity distribution at the different distance from the focal point: a) -1.5 mm; b) -1.05 mm; c) -0.6 mm; d) -0.3 mm; e) focal point; f) 0.2 mm; g) 0.4 mm; h) 0.7 mm.

To visualise the focusing ability of the lens along the beam propagation direction, the microfluidic lens together with the reservoir was fabricated (Figure 70a). The reservoir was 2 mm in length and was filled with the fluorescence fluid with the maximum fluorescence intensity at the 532 nm wavelength. The 532 nm laser beam was directed to the aspheric lens, and the snapshot of the fluorescence intensity distribution was registered (Figure 70b).

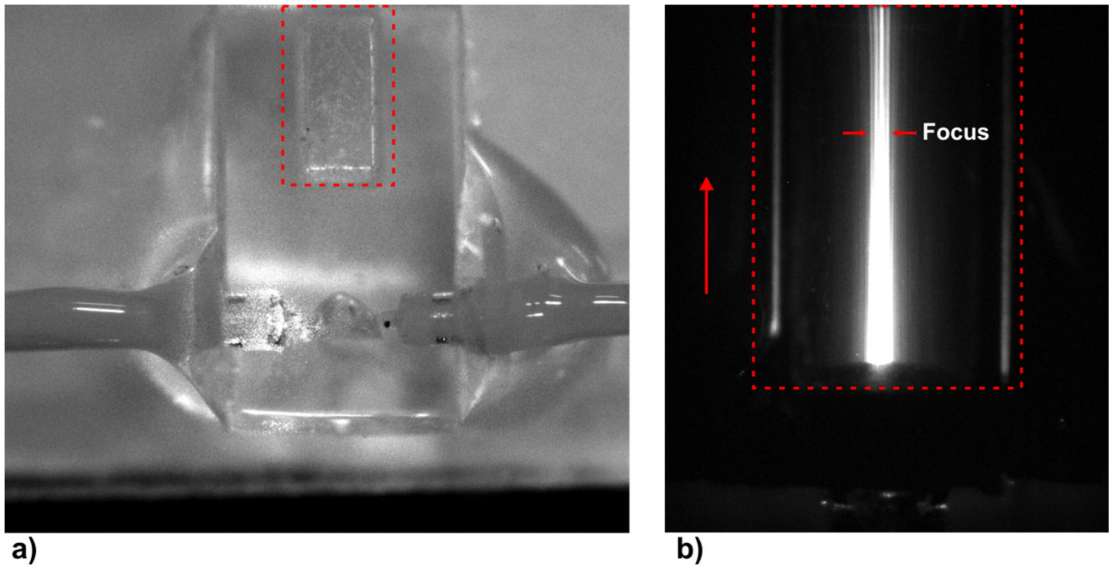

Figure 70 a) The microscope picture of the aspheric lens with the reservoir; b) The fluorescence of the focused beam. The red arrow shows the beam propagation direction.

The registered focus position was almost in the centre of the reservoir that corresponded to ~ 1.5 mm focal length. The aspheric lens demonstrated excellent focusing properties, and that was used for more complex structures formation (in the next section).

5.4.2 *Design and fabrication of a complex lens system in combination with a waveguide*

In this section, the new complex lens structure was designed and tested to build the micro device for beam collimating and focusing from the Y-waveguide which further can be used in microfluidic devices for the fluid velocity measurement based on the laser Doppler velocimetry.

First of all, the Y-waveguides were recorded 1 mm below the fused silica surface. It was found that the optimal pulse energy required for the waveguide writing was 100 nJ and the 0.5 mm/s processing speed at the 500 kHz repetition rate. The microscope objective with NA=0.55 and the 515 nm wavelength laser radiation were used. The best guiding characteristics were demonstrated for 12 stacked lines in one Y-waveguide branch with the distance of 1 µm between the stacked lines. The distance between Y branches was selected to be 260 µm. The total length of the waveguide was 5.5 mm to keep the optimal bending radius of the waveguide. The microscope picture and near field intensity distribution are demonstrated in Figure 71.

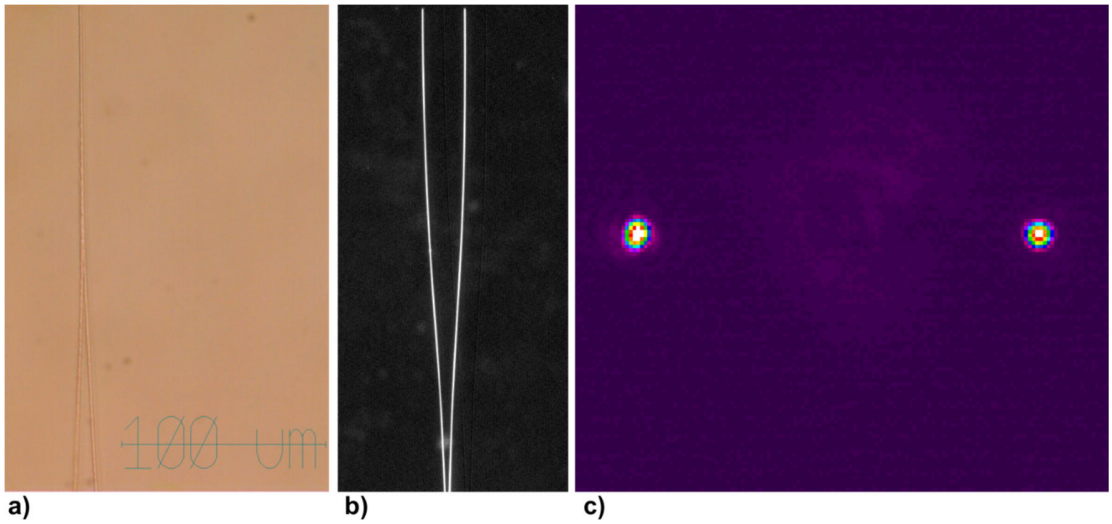

Figure 71 The Y-waveguide inscribed 1 mm below the fused silica surface with the 100 nJ pulse energy and 0.5 mm/s translation speed. a) Microscope picture of the inscribed waveguide; b) CCD image of the light guided through the waveguide; c) Near-field intensity distribution of the light at the Y-waveguide output.

After exiting from the waveguide, light propagates with a divergence defined by the refraction index contrast and distribution (NA of a waveguide). Therefore, the light should be collimated. For that purpose, the special double aspherical lens was designed (Figure 72a). The lens is fabricated at the focal length distance from the end of the waveguide. The lens initially collimates light coming out of the waveguide, and, consequently, two collimated and parallel adjusted beams

propagate. They are focused by the second surface of the lens (Figure 74b). In this way, the interference pattern is achieved, that further can be used for sensing applications. The laser beam was coupled into the waveguide using a single mode fibre which was glued in the specially etched connector (Figure 74e).

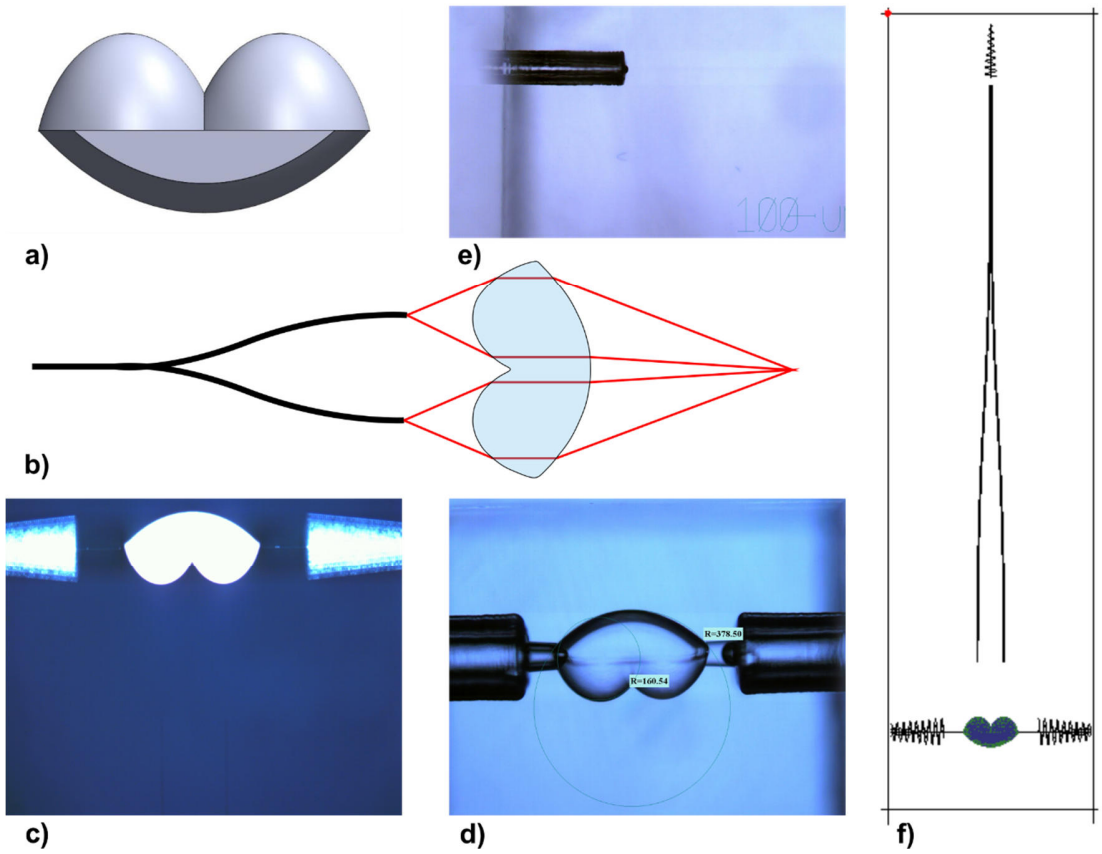

Figure 72 The 3D design and fabrication of the special designed aspherical lens. a) The design of double side aspherical lens for collimating and focusing; b) The operation principle of the double side aspherical lens; c) The crossed polarizers microscope picture of fabricated lens structure; d) The lens structure etched in 15% HF for 4 hours; e) The etched inlet for the fiber; f) The full view of the waveguide and collimating-focusing lens structure.

The external hoses (Idex, 350 µm external diameter) and fibre were connected to the fabricated structure, and then the whole structure was mounted in the characterization setup (described in Section 2.7). The microfluidic lens was filled with the refractive index compensation fluid (n=1.73, Figure 73a) and the red beam from the He-Ne laser was directed through the waveguide structure and the lens. The near field intensity profile was registered in two planes: directly at the lens back

surface (Figure 73b) and at the focal plane of the lens (Figure 73c) where two focused beams were combined to a single spot.

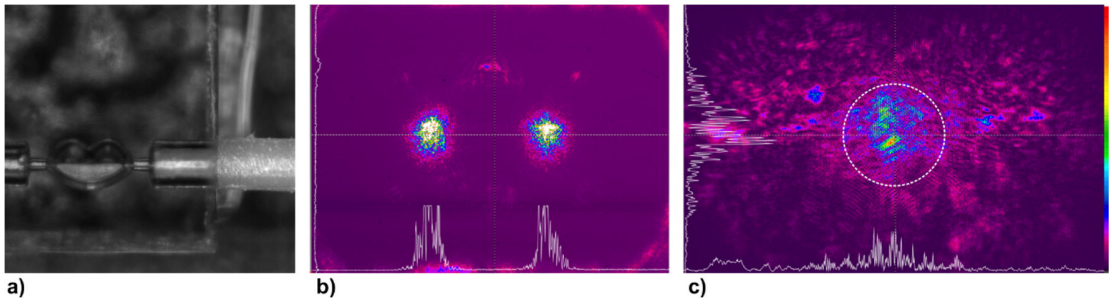

Figure 73 a) The camera picture of the double side aspheric lens filled with the refractive index matching fluid; b) the near field intensity distribution of the light beam passed the lens, directly on the second lens surface; c) the intensity profile pattern of the two focused and combined to a single spot beams (marked in the white circle).

To summarize, we have demonstrated the complex design aspherical microfluidic lens that is able to collimate and focus the light coming from the Y shaped waveguide. The concept design of the embedded device was demonstrated and the prelaminar focusing ability showed that we going on the right way. The focusing conditions further should be improved by optimising the lens design by applying the shape compensation calculations that are required due the different etchant penetration time periods into the already etched and non-etched areas. The further work is required to fulfil the device for the attractive applications such as fluid and particles speed in the fluid measurement in the real time. This can be achieved by including one additional channel where the fluid will flow. The focused radiation from the Y shaped waveguide will interfere and the Doppler shift will be measured, that actually will show the fluid speed.

5.5 Conclusions

- First of all, various scanning methods were tested to optimise the etching conditions, then a few microfluidic devices of complex 3D geometry were fabricated. Three different microfluidic devices were fabricated: Venturi-type

micropump, internal-to-external microfluidic device for the ellipsometric applications and double side aspherical lens.

- Two different scanning methods for the formation of three-dimensional microsystems were tested: the line scanning strategy and the contour scanning strategy. The etching selectivity with the proposed contour scanning shows promising results as enable easier acid penetration into the modified region.
- The formation of structures with different laser pulse energies, the pulse overlap, polarization states and distances between scanning lines was performed. The maximum etched volume speed for linear polarization was achieved with the 200 nJ pulse energy and for the circular polarization – with the 400 nJ pulse energy.
- The volume etching rate with the linear polarization was larger when the pulse energy was decreased to 200 nJ that may be concerned with nanograting singularity dependence on the laser pulse energy. In the circular polarization case, the etching speed does not depend on the scanning direction. It has been shown that the circular polarization in combination with the contour scanning strategy is preferable when the complex 3D structures are formed.
- The grain size of the etched structure can be minimised when the lower pulse energy for the formation of structures is used. In this case, the surface roughness could be minimised.
- The micropump device with mixing capability was demonstrated. The design of the device was optimised during the simulation. Several micropumps designs were simulated and fabricated. The femtosecond laser-induced chemical etching technique has shown a flexible possibility to fabricate such type of micro devices.
- The internal-to-external microchannels were fabricated and interconnected to a single device for the iSPR setup. The roughness of the external microchannel part was investigated and shown that the processing with lower pulse energy

(200 nJ) and with low speed (<10 mm/s at 500 kHz) should be performed to improve the quality of microchannel. However, to improve the processing time the ≥ 10 mm/s speed should be applied, and then the quality of the external channel decreases slightly.

- The protein adsorption kinetic was measured in the assembled microfluidic device. The formed parallel microchannels allow the measurement parallelization that enables more efficient use of sensor chip and repeatability of experimental conditions.
- The microfluidic aspherical lens filled with the refractive index matching fluid was demonstrated. The characterization showed that the focusing comparing with the simple spherical lens was improved. The aspheric design further was chosen for complex double side aspheric lens fabrication that showed the ability to collimate and then focus the light from the Y waveguide to a single spot on the focal plane that further can be used for the fluid measurement based on the laser Doppler velocimetry.

6 List of main results and conclusions

- The femtosecond lasers operating at the 515 nm and 1030 nm wavelength is able to form high-resolution modifications in fused silica with the high etching selectivity of ~140:1 for 1030 nm by the FLICE technique. The combination of the single lines modifications enables the formation of the rectangular shaped microchannels and complex 3D structures.
- The etching time rate enhancement more than 3 times was achieved by etching in ultrasonic batch.
- The optimal pulse duration for the maximal etching selectivity of fused silica (JGS1) exceeds ~ 700 fs independent on the pulse chirp parameters.
- The etching selectivity using the 1030 nm wavelength was ~ 20% higher than for the 515 nm wavelength.

- The etching selectivity for the microchannels recorded at the 200 µm depth using 1030 nm was ~ 32 % lower than for the channels recorded at 100 µm and 50 µm depths. For the NA = 0.25 objective, the nanogratings started to be formed at higher pulse energies, and their period was not as strongly arranged as in the case of the NA=0.55 objective. The nanograting period for the deeper focusing was higher due to the lower plasma density at that depth.
- The tilt between the nanograting orientation (wave vector **K**) and the polarization for various scan directions can be as high as $\Psi \sim 2^{o}$ at the constant pulse energy. Tilt angle was maximal when directions of the scan and the polarization had an angle of $\pi/4$ (@1030 nm).
- For the linearly polarised laser pulses, the strongest variations of the nanograting width and period were observed for the scanning directions parallel and perpendicular to the electric field direction while the maximum tilt of the nanograting orientation was observed when the scanning direction was at $\varphi=45°$.
- Theoretical anisotropic heat-diffusion model which takes into account coupling of the hot electrons in the plasma with the pulse electric field, enhancing the heat diffusion in the direction of the latter was proposed. This anisotropic heating of the substrate can be responsible for a modulated absorption of light along the different scan directions and explains the nanogratings tilt phenomena and period and width variations.
- For the 515 nm wavelength, the maximum tilt angle exceeding $\Psi=3°$ was measured for the 150 nJ pulse energy (~ 4.7 J/cm^2) at the $\pi/2$ and $3\pi/4$ scan angles using the ~ 260 fs-long pulses and polarization perpendicular to the X-axis ($\boldsymbol{E}_y$).
- The precise nanograting tilt investigation on the half-wave plate angle for a few different pulse energies for the 515 nm wavelength showed the dependence of the tilt on the pulse energy. The nanograting tilt difference

between two sets recorded with two different pulse energies was maximal for polarization perpendicular to the writing direction and vanished for polarization parallel to the writing direction.

- For the 515 nm wavelenghth, the combination of the pulse energy, pulse duration and pulse front tilt could induce the tilt angles as high as Ψ=17.5°. The larger nanograting tilt angles can be achieved for longer pulse durations.
- The microfluidic device with parallel internal to external microchannels is able to enhance the ellipsometric experiment. This microchannel configuration involves the parallelization of independent measurements of adsorption kinetics thus allowing to perform several independent experiments on the same sensor chip by shifting the microchannel position.
- Two different scanning methods for the formation of three-dimensional microsystems were tested: the line scanning strategy and the contour scanning strategy. The etching selectivity with the proposed contour scanning shows promising results as enable easier acid penetration into the modified region.
- The surface roughness of the microchannels was optimal when the pulse energy was 200 nJ, and the scanning speed was ~ 1 mm/s. The roughness value of Ra~ 75 nm was achieved. The sample annealing until 1210° C can smoothen the surface roughness ~ 2 times, and Ra as low as ~ 40 nm could be achieved.
- Fabricated difficult microfluidic lens enabled collimate the light from two separated waveguides and focus to the single spot.

Bibliography

1. T. H. Maiman. "Stimulated Optical Radiation in Ruby," *Nature* **187,** 493–494 (1960).
2. W. Yang. "Femtosecond laser writing in transparent materials," *Philosophy* (2008).
3. D. Du, X. Liu, G. Korn, J. Squier, and G. Mourou. "Laser-induced breakdown from 7 ns to 150 fs by impact ionization in Si02 with pulse widths," *Appl. Phys. Lett.* **64,** 3071–3073 (2001).
4. P. P. Pronko, S. K. Dutta, J. Squier, J. V. Rudd, D. Du, and G. Mourou. "Machining of sub-micron holes using a femtosecond laser at 800 nm," *Opt. Commun.* **114,** 106–110 (1995).
5. K. M. Davis, K. Miura, N. Sugimoto, and K. Hirao. "Writing waveguides in glass with a femtosecond laser," *Opt. Lett.* **21,** 1729 (1996).
6. E. N. Glezer, M. Milosavljevic, L. Huang, R. J. Finlay, T. H. Her, J. P. Callan, and E. Mazur. "Three-dimensional optical storage inside transparent materials.," *Opt. Lett.* **21,** 2023–2025 (1996).
7. D. Homoelle, S. Wielandy, a L. Gaeta, N. F. Borrelli, and C. Smith. "Infrared photosensitivity in silica glasses exposed to femtosecond laser pulses.," *Opt. Lett.* **24,** 1311–1313 (1999).
8. Y. Sikorski, A. A. Said, P. Bado, R. Maynard, C. Florea, and K. A. Winick. "Optical waveguide amplifier in Nd-doped glass written with near-IR femtosecond laser pulses Generalised Viterbi algorithm for trellis," *Electron. Lett.* **36,** 226 (2000).
9. A. M. Streltsov and N. F. Borrelli. "Fabrication and analysis of a directional coupler written in glass by nanojoule femtosecond laser pulses," *Opt. Lett.* **26,** 42–43 (2001).
10. G. Cerullo, R. Osellame, S. Taccheo, M. Marangoni, D. Polli, R. Ramponi, P. Laporta, and S. De Silvestri. "Femtosecond micromachining of symmetric waveguides at 1.5 microm by astigmatic beam focusing.," *Opt. Lett.* **27,** 1938–1940 (2002).
11. G. Zhu, J. van Howe, M. Durst, W. Zipfel, and C. Xu. "Simultaneous spatial and temporal focusing of femtosecond pulses," in *(CLEO). Conference on Lasers and Electro-Optics, 2005.* **13,** 1506–1508 Vol. 2 (IEEE, 2005).
12. F. He, H. Xu, Y. Cheng, J. Ni, H. Xiong, Z. Xu, K. Sugioka, and K. Midorikawa. "Fabrication of microfluidic channels with a circular cross section using spatiotemporally focused femtosecond laser pulses," *Opt. Express* **35,** 1106–1108 (2010).
13. J. D. Mills, P. G. Kazansky, E. Bricchi, and J. J. Baumberg. "Embedded anisotropic microreflectors by femtosecond-laser nanomachining," *Appl. Phys. Lett.* **81,** 196–198 (2002).
14. Y. Shimotsuma, P. G. Kazansky, J. Qiu, and K. Hirao. "Self-organized nanogratings in glass irradiated by ultrashort light pulses," *Phys. Rev. Lett.* **91,** 247405 (4 pages)

(2003).

15. V. R. Bhardwaj, E. Simova, P. P. Rajeev, C. Hnatovsky, R. S. Taylor, D. M. Rayner, and P. B. Corkum. "Optically produced arrays of planar nanostructures inside fused silica.," *Phys. Rev. Lett.* **96,** 57404 (2006).

16. Y. Bellouard, A. Champion, B. Lenssen, M. Matteucci, A. Schaap, M. Beresna, C. Corbari, M. Gecevičius, P. Kazansky, O. Chappuis, M. Kral, R. Clavel, F. Barrot, J. M. Breguet, Y. Mabillard, S. Bottinelli, M. Hopper, C. Hoenninger, E. Mottay, and J. Lopez. "The femtoprint project," *J. Laser Micro Nanoeng.* **7,** 1–10 (2012).

17. A. Marcinkevičius and S. Juodkazis. "Femtosecond laser-assisted three-dimensional microfabrication in silica," *Opt. Lett.* **26,** 277–279 (2001).

18. K. Sugioka, Y. Cheng, and K. Midorikawa. "Three-dimensional microfluidic structure embedded in photostructurable glass by femtosecond laser for lab-on-chip applications," *Appl. Phys. A* **79,** 815–817 (2004).

19. D. Psaltis, S. R. Quake, and C. Yang. "Developing optofluidic technology through the fusion of microfluidics and optics.," *Nature* **442,** 381–6 (2006).

20. C. Monat, P. Domachuk, and B. J. Eggleton. "Integrated optofluidics: A new river of light," *Nat. Photonics* **1,** 106–114 (2007).

21. J. R. Goldman and J. A. Prybyla. "Ultrafast dynamics of laser-excited electron distributions in silicon.," *Phys. Rev. Lett.* **72,** 1364–1367 (1994).

22. Y. Siegal, E. N. Glezer, L. Huang, and E. Mazur. "Laser - induced phase transitions in semiconductors," *Annu. Rev. Mater. Sci* **25,** 223–247 (1995).

23. D. von der Linde, K. Sokolowski-Tinten, and J. Bialkowski. "Laser–solid interaction in the femtosecond time regime," *Appl. Surf. Sci.* **109–110,** 1–10 (1997).

24. C. B. Schaffer, A. Brodeur, and E. Mazur. "Laser-induced breakdown and damage in bulk transparent materials induced by tightly focused femtosecond laser pulses," *Meas. Sci. Technol.* **12,** 1784–1794 (2001).

25. R. R. Gattass and E. Mazur. "Femtosecond laser micromachining in transparent materials," *Nat. Photonics* **2,** 219–225 (2008).

26. L. V. Keldysh. "Ionization in the field of a strong electromagnetic wave," *Sov. Phys. jetp* **20,** 1307–1314 (1965).

27. B. C. Stuart, M. D. Feit, S. Herman, A. M. Rubenchik, B. W. Shore, and M. D. Perry. "Nanosecond-to-femtosecond laser-induced breakdown in dielectrics," *Phys. Rev. B* **53,** 1749–1761 (1996).

28. A. Kaiser, B. Rethfeld, M. Vicanek, and G. Simon. "Microscopic processes in dielectrics under irradiation by subpicosecond laser pulses," *Phys. Rev. B* **61,** 11437–11450 (2000).

29. M. D. Perry, B. C. Stuart, P. S. Banks, M. D. Feit, V. Yanovsky, and a. M. Rubenchik. "Ultrashort-pulse laser machining of dielectric materials," *J. Appl. Phys.* **85,** 6803 (1999).

30. A. V Smith and B. T. Do. "Bulk and surface laser damage of silica by picosecond and nanosecond pulses at 1064 nm.," *Appl. Opt.* **47,** 4812–4832 (2008).

31. O. Efimov, S. Juodkazis, and H. Misawa. "Intrinsic single- and multiple-pulse laser-induced damage in silicate glasses in the femtosecond-to-nanosecond region," *Phys. Rev. A* **69,** 42903 (2004).

32. B. C. Stuart, M. D. Feit, A. M. Rubenchik, B. W. Shore, and M. D. Perry. "Laser-Induced Damage in Dielectrics with Nanosecond to Subpicosecond Pulses," *Phys. Rev. Lett.* **74,** 2248–2252 (1995).

33. K. Miura, J. Qiu, H. Inouye, T. Mitsuyu, and K. Hirao. "Photowritten optical waveguides in various glasses with ultrashort pulse laser," *Appl. Phys. Lett.* **71,** 3329–3331 (1997).

34. M. Birnbaum. "Semiconductor surface damage produced by Ruby lasers," *J. Appl. Phys.* **36,** 3688–3689 (1965).

35. В. В. Баженов, А. М. Бонч-Бруевич, Р. В. Канапенас, М. Н. Либенсон, В. С. Макин, Р. Й. Петрушкявичюс, and Ю. Й. Рекснис. "Роль ПЭВ в воздейцтвии на металлы сканируемого пучка непрерывного лазерного излучения," *Sov. Tech. Phys. Lett.* **12,** 151–156 (1986).

36. Z. Guosheng, P. M. Fauchet, and A. E. Siegman. "Growth of spontaneous periodic surface structures on solids during laser illumination," *Phys. Rev. B* **26,** 5366–5381 (1982).

37. D. C. Emmony, R. P. Howson, and L. J. Willis. "Laser mirror damage in germanium at 10.6 μm," *Appl. Phys. Lett.* **23,** 598–600 (1973).

38. J. A. Van Vechten. "Experimental tests for boson condensation and superconductivity in semiconductors during pulsed beam annealing," *Solid State Commun.* **39,** 1285–1291 (1981).

39. F. Keilmann and Y. H. Bai. "Periodic surface structures frozen into CO2 laser-melted quartz," *Appl. Phys. A Solids Surfaces* **29,** 9–18 (1982).

40. J. E. Sipe, J. F. Young, J. S. Preston, and H. M. Van Driel. "Laser-induced periodic surface structure. I. Theory," *Phys. Rev. B* **27,** 1141–1154 (1983).

41. A. M. Bonch-Bruevich, M. N. Libenson, V. S. Makin, V. V. Trubaev, and S. I. Vavilov. "Surface electromagnetic waves in optics," *Opt. Eng.* **31,** 718–730 (1992).

42. A. E. Siegman and P. M. Fauchet. "Stimulated Wood's Anomalies on Laser-Illuminated Surfaces," *IEEE J. Quantum Electron.* **22,** 1384–1403 (1986).

43. E. Bricchi, B. G. Klappauf, and P. G. Kazansky. "Form birefringence and negative index change created by femtosecond direct writing in transparent materials," *Opt. Lett.* **29,** 119 (2004).

44. L. Sudrie, M. Franco, B. Prade, and A. Mysyrowicz. "Writing of permanent birefringent microlayers in bulk fused silica with femtosecond laser pulses," *Opt. Commun.* **171,** 279–284 (1999).

45. P. G. Kazansky, H. Inouye, T. Mitsuyu, K. Miura, J. Qiu, K. Hirao, and F. Starrost.

"Anomalous Anisotropic Light Scattering in Ge-Doped Silica Glass," *Phys. Rev. Lett.* **82,** 2199 (1999).

46. Y. Shimotsuma, K. Hirao, J. Qiu, and K. Miura. "Nanofabrication in transparent materials with a femtosecond pulse laser," *J. Non. Cryst. Solids* **352,** 646–656 (2006).

47. Y. Shimotsuma, K. Hirao, J. Qiu, and P. G. Kazansky. "Nano-modification inside transparent materials by femtosecond laser single beam," *Mod. Phys. Lett. B* **19,** 225–238 (2005).

48. S. Richter, C. Miese, S. Döring, F. Zimmermann, M. J. Withford, A. Tünnermann, and S. Nolte. "Laser induced nanogratings beyond fused silica - periodic nanostructures in borosilicate glasses and ULE^{TM}," *Opt. Mater. Express* **3,** 1161 (2013).

49. Y. Liao, Y. Shen, L. Qiao, D. Chen, Y. Cheng, K. Sugioka, and K. Midorikawa. "Femtosecond laser nanostructuring in porous glass with sub-50 nm feature sizes.," *Opt. Lett.* **38,** 187–9 (2013).

50. J. Gottmann, D. Wortmann, and M. Hörstmann-Jungemann. "Fabrication of sub-wavelength surface ripples and in-volume nanostructures by fs-laser induced selective etching," *Appl. Surf. Sci.* **255,** 5641–5646 (2009).

51. R. Buividas, M. Mikutis, and S. Juodkazis. "Surface and bulk structuring of materials by ripples with long and short laser pulses: Recent advances," *Prog. Quantum Electron.* **38,** 119–156 (2014).

52. W. J. Yang, E. Bricchi, P. G. Kazansky, J. Bovatsek, and A. Y. Arai. "Self-assembled periodic sub-wavelength structures by femtosecond laser direct writing," *Opt. Express* **14,** 10117–10124 (2006).

53. M. Beresna, M. Gecevičius, P. G. Kazansky, T. Taylor, and A. V. Kavokin. "Exciton mediated self-organization in glass driven by ultrashort light pulses," *Appl. Phys. Lett.* **101,** (2012).

54. E. N. Glezer and E. Mazur. "Ultrafast-laser driven micro-explosions in transparent materials," *Appl. Phys. Lett.* **71,** 882 (1997).

55. R. Taylor, C. Hnatovsky, and E. Simova. "Applications of femtosecond laser induced self-organized planar nanocracks inside fused silica glass," *Laser Photonics Rev.* **2,** 26–46 (2008).

56. P. P. Rajeev, M. Gertsvolf, E. Simova, C. Hnatovsky, R. S. Taylor, V. R. Bhardwaj, D. M. Rayner, and P. B. Corkum. "Memory in Nonlinear Ionization of Transparent Solids," *Phys. Rev. Lett.* **97,** 253001 (2006).

57. R. Buividas, L. Rosa, R. Sliupas, T. Kudrius, G. Slekys, V. Datsyuk, and S. Juodkazis. "Mechanism of fine ripple formation on surfaces of (semi)transparent materials via a half-wavelength cavity feedback.," *Nanotechnology* **22,** 55304 (2011).

58. F. Messina, E. Vella, M. Cannas, and R. Boscaino. "Evidence of delocalized excitons in amorphous solids," *Phys. Rev. Lett.* **105,** 1–4 (2010).

59. E. Vella, F. Messina, M. Cannas, and R. Boscaino. "Unraveling exciton dynamics in amorphous silicon dioxide: Interpretation of the optical features from 8 to 11 eV," *Phys. Rev. B - Condens. Matter Mater. Phys.* **83,** 4–11 (2011).

60. J. Canning, M. Lancry, K. Cook, a. Weickman, F. Brisset, and B. Poumellec. "Anatomy of a femtosecond laser processed silica waveguide [Invited]," *Opt. Mater. Express* **1,** 998 (2011).

61. P. Martin, S. Guizard, P. Daguzan, and G. Petite. "Subpicosecond study of carrier trapping dynamics in wide-band-gap crystals," *Physical Review B - Condensed Matter and Materials Physics* **55,** 5799–5810 (1997).

62. L. Skuja, M. Hirano, H. Hosono, and K. Kajihara. "Defects in oxide glasses," *Phys. Status Solidi C Conf.* **2,** 15–24 (2005).

63. A. Pasquarello and R. Car. "Identification of Raman Defect Lines as Signatures of Ring Structures in Vitreous Silica," *Phys. Rev. Lett.* **80,** 5145–5147 (1998).

64. A. E. Geissberger and F. L. Galeener. "Raman studies of vitreous SiO2 versus fictive temperature," *Phys. Rev. B* **28,** 3266–3271 (1983).

65. J. C. Mikkelsen and F. L. Galeener. "Thermal equilibration of raman active defects in vitreous silica," *J. Non. Cryst. Solids* **37,** 71–84 (1980).

66. F. L. Galeener. "Raman and ESR studies of the thermal history of amorphous SiO2," *J. Non. Cryst. Solids* **71,** 373–386 (1985).

67. F. L. Galeener. "Planar rings in vitreous silica," *J. Non. Cryst. Solids* **49,** 53–62 (1982).

68. H. Nishikawa, E. Watanabe, D. Ito, and Y. Ohki. "Decay kinetics of the 4.4-eV photoluminescence associated with the two states of oxygen-deficient-type defect in amorphous SiO2," *Phys. Rev. Lett.* **72,** 2101–2104 (1994).

69. K. Kajihara, L. Skuja, M. Hirano, and H. Hosono. "Formation and decay of nonbridging oxygen hole centers in SiO2 glasses induced by F2 laser irradiation: In situ observation using a pump and probe technique," *Appl. Phys. Lett.* **79,** 1757–1759 (2001).

70. L. Skuja. "*Defects in SiO2 and Related Dielectrics: Science and Technology*," (Kluwer, 2000).

71. S. Juodkazis, M. Watanabe, M. Miwa, S. Matsuo, H. Misawa, and J. Nishii. "Femtosecond laser-assisted three-dimensional microfabrication in silica," *Opt. Lett.* **26,** 277–279 (2001).

72. Y. Bellouard, A. Said, M. Dugan, and P. Bado. "Fabrication of high-aspect ratio, micro-fluidic channels and tunnels using femtosecond laser pulses and chemical etching," *Opt. Express* **12,** 2120 (2004).

73. C. Hnatovsky, R. S. Taylor, E. Simova, P. P. Rajeev, D. M. Rayner, V. R. Bhardwaj, and P. B. Corkum. "Fabrication of microchannels in glass using focused femtosecond laser radiation and selective chemical etching," *Appl. Phys. A-Materials Sci. \& Process.* **84,** 47–61 (2006).

74. S. Juodkazis, K. Yamasaki, V. Mizeikis, S. Matsuo, and H. Misawa. "Formation of embedded patterns in glasses using femtosecond irradiation," *Appl. Phys. A* **79,** 1549–1553 (2004).

75. S. Kiyama, S. Matsuo, S. Hashimoto, and Y. Morihira. "Examination of etching agent and etching mechanism on femotosecond laser microfabrication of channels inside vitreous silica substrates," *J. Phys. Chem. C* **113,** 11560–11566 (2009).

76. C. Hnatovsky, R. S. Taylor, E. Simova, V. R. Bhardwaj, D. M. Rayner, and P. B. Corkum. "High-resolution study of photoinduced modification in fused silica produced by a tightly focused femtosecond laser beam in the presence of aberrations," *J. Appl. Phys.* **98,** (2005).

77. V. Maselli, R. Osellame, R. Martinez Vazquez, P. Laporta, and G. Cerullo. "Integration of optical waveguides and microfluidic channels fabricated by femtosecond laser irradiation," *Conf. Lasers Electro-Optics, 2007, CLEO 2007* **231118,** 12–15 (2007).

78. K. C. Vishnubhatla, N. Bellini, R. Ramponi, G. Cerullo, and R. Osellame. "Shape control of microchannels fabricated in fused silica by femtosecond laser irradiation and chemical etching," *Opt. Express* **17,** 8685–8695 (2009).

79. R. Osellame, H. J. W. M. Hoekstra, G. Cerullo, and M. Pollnau. "Femtosecond laser microstructuring: An enabling tool for optofluidic lab-on-chips," *Laser Photonics Rev.* **5,** 442–463 (2011).

80. R. A. B. Devine, R. Dupree, I. Farnan, and J. J. Capponi. "Pressure-induced bond-angle variation in amorphous SiO2," *Phys. Rev. B* **35,** 2560–2562 (1987).

81. C. Hnatovsky, R. S. Taylor, E. Simova, V. R. Bhardwaj, D. M. Rayner, and P. B. Corkum. "Polarization-selective etching in femtosecond laser-assisted microfluidic channel fabrication in fused silica," *Opt. Lett.* **30,** 1867–1869 (2005).

82. K. Sugioka, Y. Cheng, and K. Midorikawa. "All-in-One'' Chip Fabrication by 3D Femtosecond Laser Microprocessing for Biophotonics," *J. Phys. Conf. Ser.* **59,** 533 (2007).

83. K. Sugioka, Y. Hanada, and K. Midorikawa. "Three-dimensional femtosecond laser micromachining of photosensitive glass for biomicrochips," *Laser Photonics Rev.* **4,** 386–400 (2010).

84. K. Sugioka and Y. Cheng. "Femtosecond laser processing for optofluidic fabrication," *Lab Chip* **12,** 3576–3589 (2012).

85. G. M. Whitesides. "The origins and the future of microfluidics.," *Nature* **442,** 368–73 (2006).

86. R. Aris. "On the dispersion of a solute in a fluid flowing through a tube," *Proc. R. Soc. A Math. Phys. Eng. Sci.* **235,** 67–77 (1956).

87. J. P. Brody, P. Yager, R. E. Goldstein, and R. H. Austin. "Biotechnology at low Reynolds numbers.," *Biophys J* **71,** 3430–3441 (1996).

88. H. Cao, J. O. Tegenfeldt, R. H. Austin, and S. Y. Chou. "Gradient nanostructures

for interfacing microfluidics and nanofluidics," *Appl. Phys. Lett.* **81,** 3058–3060 (2002).

89. J. C. McDonald, D. C. Duffy, J. R. Anderson, D. T. Chiu, H. Wu, O. J. Schueller, and G. M. Whitesides. "Fabrication of microfluidic systems in poly(dimethylsiloxane)," *Electrophoresis* **21,** 27–40 (2000).

90. H. Becker and U. Heim. "Hot embossing as a method for the fabrication of polymer high aspect ratio structures," *Sensors Actuators, A Phys.* **83,** 130–135 (2000).

91. S. Qi, X. Liu, R. H. Nilson, et al. "Microfluidic devices fabricated in poly(methyl methacrylate) using hot-embossing with integrated sampling capillary and fiber optics for fluorescence detection," *Lab Chip* **2,** 88–95 (2002).

92. R. D. Chien. "Micromolding of biochip devices designed with microchannels," *Sensors Actuators, A Phys.* **128,** 238–247 (2006).

93. U. M. Attia, S. Marson, and J. R. Alcock. "Micro-injection moulding of polymer microfluidic devices," *Microfluid. Nanofluidics* **7,** 1–28 (2009).

94. M. Masuda, K. Sugioka, Y. Cheng, N. Aoki, M. Kawachi, K. Shihoyama, K. Toyoda, H. Helvajian, and K. Midorikawa. "3-D microstructuring inside photosensitive glass by femtosecond laser excitation," *Appl. Phys. A Mater. Sci. Process.* **76,** 857–860 (2003).

95. J. Rossier, F. Reymond, and P. E. Michel. "Polymer microfluidic chips for electrochemical and biochemical analyses," *Electrophoresis* **23,** 858–867 (2002).

96. Y. Li, K. Itoh, W. Watanabe, K. Yamada, D. Kuroda, J. Nishii, and Y. Jiang. "Three-dimensional hole drilling of silica glass from the rear surface with femtosecond laser pulses," *Opt. Lett.* **26,** 1912 (2001).

97. Lee, Park, and Whitesides. "Solvent compatibility of poly (dimethylsiloxane)-based microfluidic devices," *Anal. Chem. Dc-* **75,** 6544–6554 (2003).

98. J. C. McDonald and G. M. Whitesides. "Poly (dimethylsiloxane) as a Material for Fabricating Microfluidic Devices," *Acc. Chem. Res.* **35,** 491–499 (2002).

99. Y. Fainman, L. P. Lee, D. Psaltis, and C. Yang. "*Optofluidics: Fundamentals, devices, and application*," (McGraw-Hill Professional, 2010).

100. K. Sugioka and Y. Cheng. "Ultrafast lasers—reliable tools for advanced materials processing," *Light Sci. Appl.* **3,** e149 (2014).

101. G. Della Valle, R. Osellame, and P. Laporta. "Micromachining of photonic devices by femtosecond laser pulses," *J. Opt. A Pure Appl. Opt.* **11,** 13001 (2009).

102. Y. Bellouard, A. A. Said, and P. Bado. "Integrating optics and micro-mechanics in a single substrate: a step toward monolithic integration in fused silica.," *Opt. Express* **13,** 6635–6644 (2005).

103. M. C. Potter and D. C. Wiggert. "*Mechanics of fluids*," (CA: Brooks/ Cole, 2002).

104. W. E. Svendsen. "*Lab-on-a-Chip Devices and Micro-Total Analysis Systems*," (Springer International Publishing, 2015). doi:10.1007/978-3-319-08687-3

105. J. P. Holman. "*Principles of convection. In: Heat transfer*," (McGraw-Hill, 1997).

106. M. Lard. "*Lab 3 : COMSOL*," (2014).

107. "Free shear flow illustrating laminar, transition and turbulent phases," Available at: https://encrypted-tbn0.gstatic.com/images?q=tbn:ANd9GcSXu7RprYvehrG8Okb_KP4-I6TnODlVNN7pcB7JFnlWFqDW6gDmUw.

108. T. M. Squires and S. R. Quake. "Microfluidics Fluid physics at the nanoliter.pdf," *Rev. Mod. Phys.* **77,** 978–1026 (2005).

109. S. M. Eaton, H. Zhang, P. R. Herman, F. Yoshino, L. Shah, J. Bovatsek, and A. Y. Arai. "Heat accumulation effects in femtosecond laser-written waveguides with variable repetition rate," *Opt. Express* **13,** 4708 (2005).

110. R. Trebino, P. Bowlan, P. Gabolde, and X. Gu. "Measuring Everything You've Ever Wanted to Know About an Ultrashort Light Pulse," *Mitr.P.Lodz.Pl* 1–41

111. R. Trebino. "*Frequency-Resolved Optical Gating: The Measurement of Ultrashort Laser Pulses*," *Frequency-Resolved Optical Gating: The Measurement of Ultrashort Laser Pulses* (2002). doi:10.1007/978-1-4615-1181-6

112. R. Wyatt and E. E. Marinero. "Versatile single-shot background-free pulse duration measurement technique, for pulses of subnanosecond to picosecond duration," *Appl. Phys.* **25,** 297–301 (1981).

113. A. Brun, P. Georges, G. Le Saux, and F. Salin. "Single-shot characterization of ultrashort light pulses," *J. Phys. D. Appl. Phys.* **24,** 1225–1233 (1991).

114. S. Szatmári, F. P. Schäfer, and J. Jethwa. "A single-shot autocorrelator for the ultraviolet with a variable time window," *Rev. Sci. Instrum.* **61,** 998–1003 (1990).

115. Juodkazis S., Y. Tabuchi, T. Ebisui, S. Matsuo, and H. Misawa. "Anisotropic etching of dielectrics exposed by high intensity femtosecond pulses," *Adv. Laser Technol. 2004* **5850,** 59–66 (2005).

116. M. Hörstmann-Jungemann, J. Gottmann, and M. Keggenhoff. "3D-microstructuring of sapphire using fs-laser irradiation and selective etching," *J. Laser Micro Nanoeng.* **5,** 145–149 (2010).

117. S. Lo Turco, R. Osellame, R. Ramponi, and K. C. Vishnubhatla. "Hybrid chemical etching of femtosecond irradiated 3D structures in fused silica glass," *MATEC Web Conf.* **8,** 5009 (2013).

118. V. Stankevič and G. Račiukaitis. "Formation of rectangular channels in fused silica by laser-induced chemical etching," *Lith. J. Phys.* **54,** 136–141 (2014).

119. V. Stankevič, G. Račiukaitis, F. Bragheri, X. Wang, E. G. Gamaly, R. Osellame, and S. Juodkazis. "Laser printed nano-gratings : orientation and period peculiarities," *Sci. Rep.* **7,** 1–9 (2016).

120. S. Ho, P. R. Herman, and J. S. Aitchison. "Single- and multi-scan femtosecond laser writing for selective chemical etching of cross section patternable glass micro-channels," *Appl. Phys. A* **106,** 5–13 (2012).

121. C. Hnatovsky, R. S. Taylor, P. P. Rajeev, E. Simova, V. R. Bhardwaj, D. M. Rayner, and P. B. Corkum. "Pulse duration dependence of femtosecond-laser-fabricated nanogratings in fused silica," *Appl. Phys. Lett.* **87,** 98–101 (2005).

122. M. Hermans, J. Gottmann, and F. Riedel. "Selective, laser-induced etching of fused silica at high scan-speeds using KOH," *J. Laser Micro Nanoeng.* **9,** 126–131 (2014).

123. G. Min. "*Advanced optical imaging theory*," (Springer, 1999).

124. H. B. Sun and S. Kawata. "Two-photon photopolymerization and 3D lithographic microfabrication," *Adv. Polym. Sci.* **170,** 169–273 (2004).

125. H. B. Sun, M. Maeda, K. Takada, J. W. M. Chon, M. Gu, and S. Kawata. "Experimental investigation of single voxels for laser nanofabrication via two-photon photopolymerization," *Appl. Phys. Lett.* **83,** 819–821 (2003).

126. T. a Klar, R. Wollhofen, and J. Jacak. "Sub-Abbe resolution: from STED microscopy to STED lithography," *Phys. Scr.* **T162,** 14049 (2014).

127. Y. C. Cheng, H. Zeng, J. Trull, C. Cojocaru, M. Malinauskas, T. Jukna, D. S. Wiersma, and K. Staliunas. "Beam focalization in reflection from flat dielectric subwavelength gratings.," *Opt. Lett.* **39,** 6086–9 (2014).

128. S. Rekštytė, T. Jonavičius, D. Gailevičius, M. Malinauskas, V. Mizeikis, E. G. Gamaly, and S. Juodkazis. "Nanoscale Precision of 3D Polymerization via Polarization Control," *Adv. Opt. Mater.* **4,** 1209–1214 (2016).

129. B. Bin Xu, L. Wang, Z. C. Ma, R. Zhang, Q. D. Chen, C. Lv, B. Han, X. Z. Xiao, X. L. Zhang, Y. L. Zhang, K. Ueno, H. Misawa, and H. B. Sun. "Surface-plasmon-mediated programmable optical nanofabrication of an oriented silver nanoplate," *ACS Nano* **8,** 6682–6692 (2014).

130. B. Öktem, I. Pavlov, S. Ilday, H. Kalaycıoğlu, A. Rybak, S. Yavaş, M. Erdoğan, and F. Ö. Ilday. "Nonlinear laser lithography for indefinitely large-area nanostructuring with femtosecond pulses," *Nat. Photonics* **7,** 897–901 (2013).

131. J. M. Guay, A. Villafranca, F. Baset, K. Popov, L. Ramunno, and V. R. Bhardwaj. "Polarization-dependent femtosecond laser ablation of poly-methyl methacrylate," *New J. Phys.* **14,** (2012).

132. D. M. Simanovskii, H. A. Schwettman, H. Lee, and A. J. Welch. "Midinfrared optical breakdown in transparent dielectrics.," *Phys. Rev. Lett.* **91,** 107601 (2003).

133. A. Rudenko, J. P. Colombier, and T. E. Itina. "From random inhomogeneities to periodic nanostructures induced in bulk silica by ultrashort laser," *Phys. Rev. B - Condens. Matter Mater. Phys.* **93,** 1–13 (2016).

134. D. Puerto, M. Garcia-Lechuga, J. Hernandez-Rueda, A. Garcia-Leis, S. Sanchez-Cortes, J. Solis, and J. Siegel. "Femtosecond laser-controlled self-assembly of amorphous-crystalline nanogratings in silicon," *Nanotechnology* **27,** 265602 (2016).

135. J. Gottmann, D. Wortmann, and R. Wagner. "Manufacturing of periodical nanostructures by fs-laser direct writing," *Proc. SPIE* **7022,** 702202-702202–10

(2007).

136. M. Beresna, M. Gecevičius, P. G. Kazansky, and T. Gertus. "Radially polarized optical vortex converter created by femtosecond laser nanostructuring of glass," *Appl. Phys. Lett.* **98,** 2–4 (2011).

137. L. Marrucci, E. Karimi, S. Slussarenko, B. Piccirillo, E. Santamato, E. Nagali, and F. Sciarrino. "Spin-to-orbital conversion of the angular momentum of light and its classical and quantum applications," *J. Opt.* **13,** 64001 (2011).

138. J. Zhang, M. Gecevičius, M. Beresna, and P. G. Kazansky. "Seemingly unlimited lifetime data storage in nanostructured glass," *Phys. Rev. Lett.* **112,** 1–5 (2014).

139. C. J. de Jong, A. Lajevardipour, M. Gecevičius, M. Beresna, G. Gervinskas, P. G. Kazansky, Y. Bellouard, A. H. A. Clayton, and S. Juodkazis. "Deep-UV fluorescence lifetime imaging microscopy," *Photonics Res.* **3,** 283 (2015).

140. C. Hnatovsky, V. Shvedov, W. Krolikowski, and A. Rode. "Revealing local field structure of focused ultrashort pulses," *Phys. Rev. Lett.* **106,** 1–4 (2011).

141. S. Juodkazis, V. Mizeikis, S. Matsuo, K. Ueno, and H. Misawa. "Three-dimensional micro- And nano-structuring of materials by tightly focused laser radiation," *Bull. Chem. Soc. Jpn.* **81,** 411–448 (2008).

142. J. F. Young, J. S. Preston, H. M. Van Driel, and J. E. Sipe. "Laser-induced periodic surface structure. II. Experiments on Ge, Si, Al, and brass," *Phys. Rev. B* **27,** 1155–1172 (1983).

143. S. Sakabe, M. Hashida, S. Tokita, S. Namba, and K. Okamuro. "Mechanism for self-formation of periodic grating structures on a metal surface by a femtosecond laser pulse," *Phys. Rev. B - Condens. Matter Mater. Phys.* **79,** 1–4 (2009).

144. K. Miyazaki and G. Miyaji. "Nanograting formation through surface plasmon fields induced by femtosecond laser pulses," *J. Appl. Phys.* **114,** (2013).

145. S. K. Das, H. Messaoudi, A. Debroy, E. McGlynn, and R. Grunwald. "Multiphoton excitation of surface plasmon-polaritons and scaling of nanoripple formation in large bandgap materials," *Opt. Mater. Express* **3,** 1705 (2013).

146. Y. Liao, J. Ni, L. Qiao, M. Huang, Y. Bellouard, K. Sugioka, and Y. Cheng. "High-fidelity visualization of formation of volume nanogratings in porous glass by femtosecond laser irradiation," *Optica* **2,** 329 (2015).

147. E. G. Gamaly and A. V. Rode. "Coupling of polarisation of high frequency electric field and electronic heat conduction in laser created plasma," *Opt. Laser Technol.* **82,** 69–71 (2016).

148. E. M. Lifshitz and L. P. Pitaevski. "*Physical Kinetics*," (Pergamon, 1981).

149. D. Puerto, W. Gawelda, J. Siegel, J. Bonse, G. Bachelier, and J. Solis. "Transient reflectivity and transmission changes during plasma formation and ablation in fused silica induced by femtosecond laser pulses," *Appl. Phys. A Mater. Sci. Process.* **92,** 803–808 (2008).

150. M. Sakakura, M. Terazima, Y. Shimotsuma, K. Miura, and K. Hirao. "Thermal and

shock induced modification inside a silica glass by focused femtosecond laser pulse," *J. Appl. Phys.* **109,** 0–8 (2011).

151. M. Sakakura, M. Terazima, Y. Shimotsuma, K. Miura, and K. Hirao. "Observation of pressure wave generated by focusing a femtosecond laser pulse inside a glass," *Opt. Express* **15,** 5674–5686 (2007).

152. A. Champion, M. Beresna, P. Kazansky, and Y. Bellouard. "Stress distribution around femtosecond laser affected zones: effect of nanogratings orientation.," *Opt. Express* **21,** 24942–51 (2013).

153. S. Juodkazis, Y. Nishi, H. Misawa, V. Mizeikis, O. Schecker, R. Waitz, P. Leiderer, and E. Scheer. "Optical transmission and laser structuring of silicon membranes," *Opt. Express* **17,** 15308–15317 (2009).

154. M. Malinauskas, A. Žukauskas, G. Bičkauskaitė, R. Gadonas, and S. Juodkazis. "Mechanisms of three-dimensional structuring of photo-polymers by tightly focussed femtosecond laser pulses," *Opt. Express* **18,** 10209 (2010).

155. Y. Hayasaki, K. Iwata, S. Hasegawa, A. Takita, and S. Juodkazis. "Time-resolved axial-view of the dielectric breakdown under tight focusing in glass," *Opt. Mater. Express* **1,** 1399 (2011).

156. P. G. Kazansky, W. Yang, E. Bricchi, J. Bovatsek, and A. Arai. "“Quill” writing with ultrashort light pulses in transparent optical materials," *Conf. Lasers Electro-Optics, 2007, CLEO 2007* **151120,** 2005–2008 (2007).

157. F. He, J. Lin, and Y. Cheng. "Fabrication of hollow optical waveguides in fused silica by three-dimensional femtosecond laser micromachining," *Appl. Phys. B Lasers Opt.* **105,** 379–384 (2011).

158. E. K. Sackmann, A. L. Fulton, and D. J. Beebe. "The present and future role of microfluidics in biomedical research.," *Nature* **507,** 181–9 (2014).

159. S. Pennathur. "Flow control in microfluidics: are the workhorse flows adequate?," *Lab Chip* **8,** 383 (2008).

160. R. Zengerle, J. Ulrich, S. Kluge, M. Richter, and A. Richter. "A bidirectional silicon micropump," *Sensors Actuators A Phys.* **50,** 81–86 (1995).

161. W. L. Benard, H. Kahn, A. H. Heuer, and M. a. Huff. "A titanium-nickel shape-memory alloy actuated micropump," in *Proceedings of International Solid State Sensors and Actuators Conference (Transducers ’97)* **1,** 361–364 (IEEE, 1997).

162. C. H. Ahn and M. G. Allen. "Fluid micropumps based on rotary magnetic actuators," in *Proceedings IEEE Micro Electro Mechanical Systems. 1995* 408 (IEEE, 1995). doi:10.1109/MEMSYS.1995.472590

163. A. Manz, C. S. Effenhauser, N. Burggraf, D. J. Harrison, K. Seiler, and K. Fluri. "Electroosmotic pumping and electrophoretic separations for miniaturized chemical analysis systems," *J. Micromechanics Microengineering* **4,** 257–265 (1994).

164. K. Koo, M. Jeong, S. Park, H. Choi, and G. Kim. "Novel valveless micro suction pump using a solid chemical propellant," *World Congr. Med. Phys. Biomed. Eng.*

2006 **14,** 310–313 (2007).

165. V. Stankevič and G. Račiukaitis. "Free-shape 3D structure formation in bulk fused silica by irradiation with femtosecond laser pulses," *JLMN-Journal of Laser Micro/Nanoengineering* **9,** 271–275 (2014).

166. S. Rekveld. "Ellipsometric studies of protein adsorption onto hard surfaces in a flow cell," (1997).

167. J. Homola, S. S. Yee, and G. Gauglitz. "Surface plasmon resonance sensors: review," *Sensors Actuators B Chem.* **54,** 3–15 (1999).

168. X. Guo. "Surface plasmon resonance based biosensor technique: A review," *J. Biophotonics* **5,** 483–501 (2012).

169. T. H. Seefeld, A. R. Halpern, and R. M. Corn. "On-Chip Synthesis of Protein Microarrays from DNA Microarrays via Coupled In Vitro Transcription and Translation for Surface Plasmon Resonance Imaging Biosensor Applications," *J. Am. Chem. Soc.* **134,** 12358–12361 (2012).

170. H. Raether. "*Surface Plasmons on Smooth and Rough Surfaces and on Gratings*," *Springer Tracts in Modern Physics* **111,** (Springer Berlin Heidelberg, 1988).

171. P. Paiè, F. Bragheri, T. Claude, and R. Osellame. "Adaptable acylindrical microlenses fabricated by femtosecond laser micromachining," *Spie Lase* **9355,** 935516 (2015).